Cover Page

Universiteit Leiden

The handle http://hdl.handle.net/1887/53199 holds various files of this Leiden University dissertation.

Author: Zuiden, B.C. van
Title: Topology and geometry in chiral liquids
Issue Date: 2017-09-27

Topology and Geometry in Chiral Liquids

PROEFSCHRIFT

ter verkrijging van
de graad van Doctor aan de Universiteit Leiden,
op gezag van Rector Magnificus prof. mr. C. J. J. M. Stolker,
volgens besluit van het College van Promoties
te verdedigen op woensdag 27 september 2017
klokke 13.45 uur

door

Benjamin Chai van Zuiden
Geboren te Jeruzalem, Israël in 1987

Promotor:

prof. dr. V. Vitelli

Promotiecommissie:

prof. dr. D. Bartolo (École Normale Supérieure de Lyon, FR)
dr. W. T. M. Irvine (the University of Chicago, USA)
prof. dr. E. R. Eliel
prof. dr. H. Schiessel
dr. L. Giomi

The research done for this thesis was mostly conducted at the Lorentz Institute for theoretical physics, Leiden University, the Netherlands.

The use of general descriptive names, registered names, trademarks, etc. in this thesis does not imply, even in the absence of a specific statement, that such names are exempt from the relevant protective laws and regulations and therefore free for general use.

This thesis will be made available in electronic form at the Leiden University repository located at: `https://openaccess.leidenuniv.nl`.

Casimir PhD Series, Leiden–Delft, 2017–25.
ISBN 978-90-8593-309-0

Contents

Introduction **1**

1 Chiral texture in toroidal liquid crystals **11**

2 Topological chiral sound in active liquids **33**

3 Chiral active liquids with self-rotation **53**

4 Molecular dynamics on a curved substrate **77**

Appendices **105**

References **137**

Samenvatting **149**

List of publications **153**

Curriculum vitæ **155**

Introduction

Materials and metamaterials consist of fundamental units called particles. The material properties of these *microscopic* components often determine the *macroscopic* properties of the resulting material. In many cases, however, it turns out that the underlying *geometrical* and *topological* properties of the many-body system or confining space also have a tremendous impact on the macroscopic properties of matter. From a solid understanding of how materials and metamaterials achieve their properties one can start designing materials and metamaterials with useful and novel functionalities [18, 19, 34, 37].

Chiral symmetry

The concept of spontaneous symmetry breaking is one of the cornerstones of modern physics. Spontaneous symmetry breaking occurs when the laws of physics are invariant under a certain symmetry. One of these symmetries is *chirality* — or handedness. Spontaneous symmetry breaking due to chirality is often referred to as chiral symmetry breaking. The concept of chirality is perhaps easily understood when observing our hands. Our right hand cannot possibly be superimposed on our left hand, unless the palms are facing the opposite directions. Our hands are each other's mirror image. Chiral objects are all around us: examples are screws, fusilli pasta, guitars, bikes, cars, etc. The test for chirality is simple: as long as we cannot recreate the mirror image of the object by translating and/or rotating the object in its entirety, the object is chiral; otherwise it is not. For example, a coffee mug is not chiral as its mirror image can be found by rotating the mug by half a turn. A simple system showing chiral symmetry breaking is depicted in fig. 1 where we find that both chiral states are energy symmetric yet can not be transformed into one another.

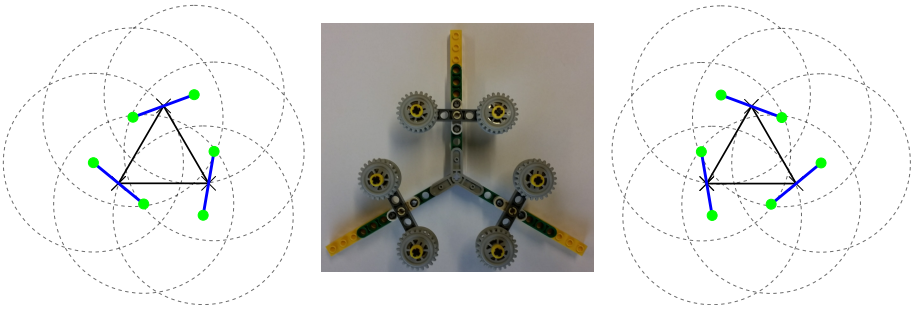

Figure 1: A simple setup showing chiral symmetry breaking. **Center**: an unstable-state achiral state made with LEGO gray bars can rotate freely. Gears are equally magnetized such that they repel one another. **Left–right**: two stable chiral states found using a numerical minimization. Both states have an equal energy lower than the unstable state. Both chiral states can be found in the LEGO setup as well.

The chirality of our hands is a spatial asymmetry. Chirality, however, can also exist as a *temporal* asymmetry. Imagine an analog clock. The second hand moves in a clockwise direction. A clock therefore possesses left-handed temporal chirality.♠ When we mirror the arrow of time, meaning that time now goes backwards, the second hand of the clock moves backwards too. In such an event, the orbit of the second hand becomes anti-clockwise. There is, however, a class of systems imaginable where the chirality does not change upon time reversal. Suppose the clock is driven by a digital signal, and the second hand represents a time interval as measured by a crystal oscillator. Then, regardless of the arrow of time, the clock's chirality is defined by the internal mechanics of the device. An experimental system with temporal chiral particles is depicted in fig. 2.

Naively, the macroscopic chirality of systems follows from the microscopic chirality of the particles of which they consist. Remarkably, however, this is not necessarily the case. Achiral particles confined in an *achiral* geometry may still spontaneously manifest a *chiral* macroscopic state. This means that due to the achiral nature of the microscopic particles, the particular choice of chirality — left-handed or right-handed — is energetically indifferent and

♠Some may argue that canonical clock is left-handed. This is purely semantical and mostly concerned with how we label things, hence irrelevant for this discussion. Physics would not change if we consistently relabeled left as right and right as left. We have implicitly assumed here that the unit vector $\hat{z}$ points from the book towards your eyes as this is the canonical *right* way — and incidentally also the right-handed way.

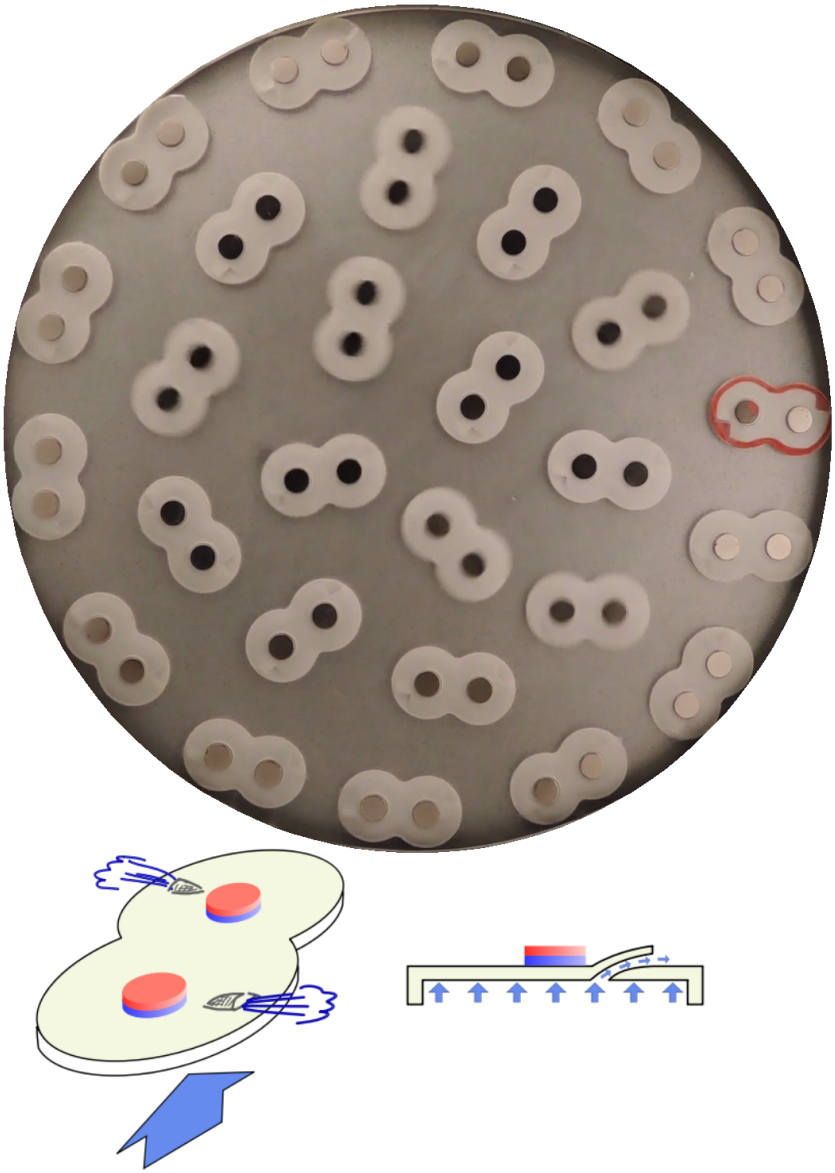

Figure 2: A setup showing temporal chiral symmetry. **Top**: a custom-built air hockey table with 3D-printed chiral pucks floating and rotating due to airflow. Pucks may appear blurred as some are rotating fast. **Bottom**: illustration of the airflow through the puck causing both lift and spin, the latter breaking temporal chiral symmetry.

hence a chiral state is spontaneously chosen. In this thesis, we will examine two examples of this effect: one spatial, chapter 1, and one temporal, chapter 2. Additionally, we will give an example of how the temporal chirality of particles determines the temporal chirality of the system in chapter 3.

Active matter

Particles are often thought of as static units. In recent attempts to understand the collective behavior of biological and robotic systems, however, physicists have researched particles which are internally or externally driven. Systems containing such particles manifest much more complex physics [52, 110, 148, 149]. These self driven systems are often called *active* systems, as energy is actively pumped into to the system at the microscale. Hence, the system consumes energy. Unlike *passive* systems, which tend to reside in *equilibrium*, active systems often reside in *steady states*, where the energy pumped into the system is on average equal to the energy dissipated from the system. In addition, as the fundamental units that form matter become increasingly more complex, so may their interactions. For instance, while a simple charged particle merely exchanges positional information with other particles — and possibly information about its velocity as well — a more complex particle may also exchange non-trivial information like a list of its neighbors, the availability of nutrition or other resources in its surroundings, etc. On the receiving end, more complex particles with a little processing power may use all this information to decide on their course of action — which likely also requires energy. These active systems offer exciting possibilities for more complex material and metamaterial design.

The canonical toy model for active matter is called the Vicsek model [133, 142, 149]. This model can be used to describe a school of fish, a flock of birds, a large group of bacterial swimmers, a swarm of robots etc. There are two assumptions the Vicsek model makes. First, particles are self-driven, yielding some stationary speed. Second, particles try to align the direction of that speed with the velocity of their neighbors. Additionally, the Vicsek model allows for noise in the alignment procedure, mimicking temperature, communication errors or similar perturbations. It relies on an overdamped version of Newton's equations of motion♠ where inertia does not play a role. The result is that, if the noise term is sufficiently low, the particles align and flock, swarming around through their confinement space, never in equilibrium but possibly in a

♠Newton's equations of motion are briefly introduced in appendix A.

steady state. In two dimensions, mean field theory finds that the model defies the Mermin–Wagner theorem, stating that long-range order cannot exist in two-dimensional equilibrium systems at finite temperature. It is therefore possible for the alignment of the self-driven particles to spontaneously emerge throughout the system.

As active matter is driven externally or internally, it naturally breaks time reversal symmetry.♠ Time reversal symmetry is the property that enables the mapping of t to $t \to -t$. As time reversal symmetry breaking is a key ingredient for a class of topological insulators, active matter might be a perfect candidate to achieve a classical topological insulator [16, 31, 82], as we will see in chapter 2.

Topology and geometry

The macroscopic properties of materials are tremendously impacted by the geometrical and topological properties of the confinement space [5, 38, 115, 132]. For passive matter this means that the ground state structure often fails to propagate throughout the system, often introducing defects or changing the structure altogether. An example of the latter will be shown in chapter 1. For active matter it means the flow of the particles is dominated by the topology and geometry of its confining space. If the confinement is for instance tubular, particles will likely flow along the long axis of the tube. Similarly, if the confinement is circular or annular, particles will tend to flow along the circle. The chirality of the flow in a circular confinement is chosen spontaneously; the same goes for an annular confinement, as we will see in chapter 2.

The concept of topology has changed both modern mathematics and physics. Topology is roughly a way to characterize a mathematical space in such a way that the characterization is invariant under continuous transformations. Suppose we have an inflated bicycle inner tube. The number of handles or holes in such a system is conserved regardless of linear transformations, geometrical irregularities and/or different embeddings. In fact, the number of handles serves as a *topological index*, an integer number that allows us to topologically characterize objects. As our bicycle tire has exactly one handle, we classify its index as one. Comparing this to, for instance, a ball which has exactly zero handles, we conclude that there is no possible way to continuously transform an inner tube into a ball — or vice versa. It is, however, possible to

♠Strictly speaking, a system with just a damping term already breaks time reversal symmetry although such a system might also demonstrate somewhat dull physics.

continuously transform an inner tube into a coffee mug — and vice versa — as the number of handles in both objects is equal. The number of handles is one of the many imaginable topological indices. A more sophisticated topological index for spatial objects is the Euler characteristic. In momentum space one may use the Chern number to conclude if certain band gaps are topologically protected, as these band gaps cannot be closed by smoothly deforming the system.

Computational physics

Performing analytical calculations on passive systems in equilibrium often requires complicated mathematics. As activity and complexity are introduced to these systems, calculations become increasingly harder. Fortunately, the discipline of computational physics may often help. Numerical methods have shown both to be an excellent way to validate analytical theories, as well as revealing new hidden physics from known analytical theories — the latter often unreachable from the analytical point of view. Combined with analytical methods and possibly experiments, the computer allows us to make great leaps forward in science as a whole.

One of the powerful numerical methods we will employ in this thesis is called molecular dynamics. Molecular dynamics is, very briefly, a method to solve the classical N-body problem numerically — in general, N bodies with arbitrary defined interactions. At its core, molecular dynamics employs one of the most validated equations in physics: Newton's equations of motion, eq. (A.2). A brief explanation of how molecular dynamics works is given in appendix O.

For this thesis a custom molecular dynamics computer library called `libmd` was written; see appendix P for more details. The library differs from other libraries as it is specifically designed to solve problems in passive and active matter with geometrical and topological constraints. More explicitly, it contains an implementation of a novel symplectic integrator that solves Newton's equation in the presence of curvature numerically, as described in chapter 4. Additionally, it employs computational techniques like automatic differentiation, appendix section G.3, to make simulations more accurate, simpler and more reliable.

Outline of this thesis

In this thesis we will study the interplay of topology and geometry with chirality for several passive and active systems, employing both analytical and numerical methods. Specifically, this thesis discusses the systems briefly mentioned here.

In chapter 1 we explain how nematic liquid crystals confined in toroidal geometries undergo structural phase transitions depending on the slenderness of the confining toroid. We will see that, although the nature of the nematic liquid crystal is achiral, the toroidal geometry will force the system to choose a chiral state. As both states yield the same Frank free energy the choice of chirality is spontaneous. This structural phase transition falls in the same universality class as the famous Ising model, a model for ferromagnetism: both are perfect examples of spontaneous symmetry breaking. For a schematic see fig. 3.

In chapter 2 we consider a system of active polar swimmers that align with their neighbors. When confined in the right geometry, the system will self-assemble into a state with topologically protected chiral acoustic modes. The chirality in this system manifests itself as a temporal one, rather than a spatial chirality. For a schematic see fig. 4.

Chapter 3 shows how systems of Yukawa charged active spinning dimers self-assemble into a crystal phase with spatiotemporal order, a liquid phase or a glass phase depending on the density. The chirality in this system is determined by the handedness of spin of the dimers. Depending on the phase and the confinement geometry of these systems of actively spinning dimers, the system will allow for rigid body rotations or edge currents. The chirality of rotations and edge currents are set by the chirality of the spinning dimers. For a schematic see fig. 5.

Finally, in chapter 4 we introduce a novel method of doing molecular dynamics on curved surfaces by developing a symplectic integrator. Although this new method can be applied to many topics, see for instance fig. 6, we present preliminary results on two-dimensional crystal melting in the presence of curvature. As melting in two dimensions is mediated by topological defects which are spatially positioned by the curvature, we find that the crystal may melt inhomogeneously.

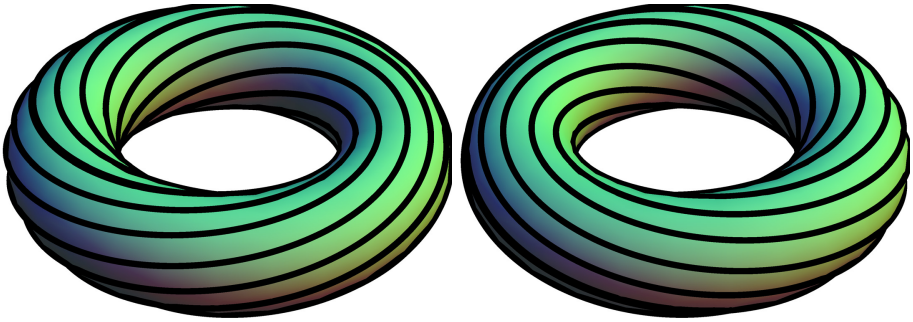

Figure 3: Schematic of left-handed (**left**) and right-handed (**right**) toroidal nematic liquid crystals.

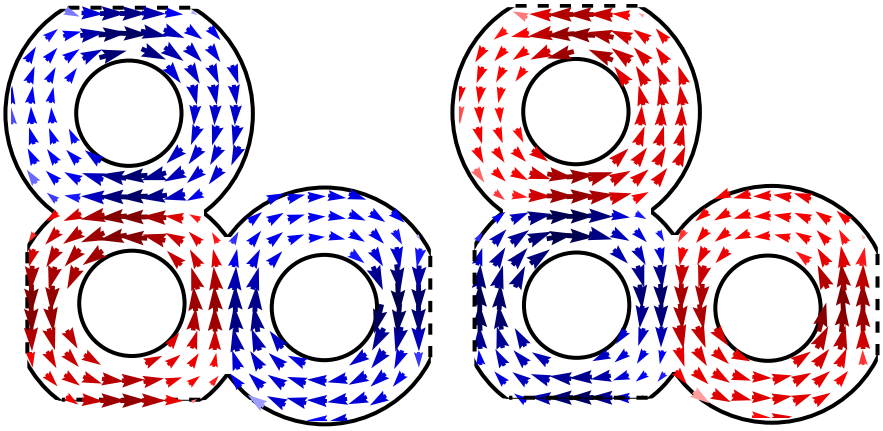

Figure 4: Schematic of a confined polar active liquid flow field with spontaneously broken chirality and left-handed (**left**) or right-handed (**right**) polarization.

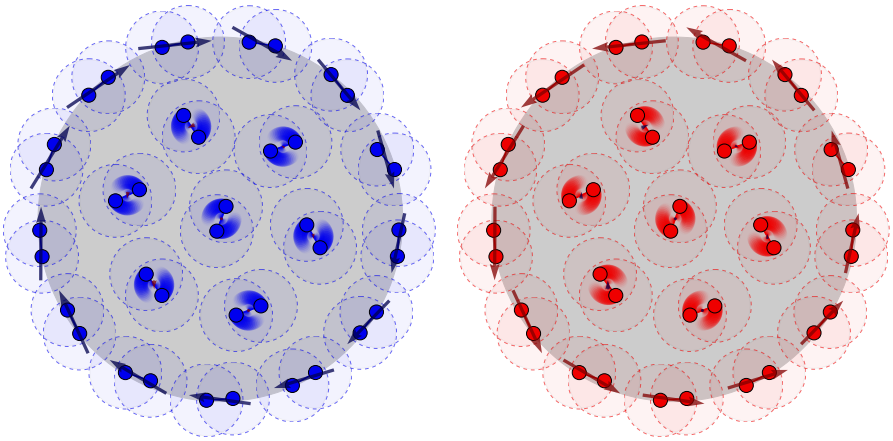

Figure 5: Snapshots of simulations done with 20 chiral dimers confined in a disk. We observe spatiotemporal order and edge currents. **Left**: a left-handed spinning system. **Right**: a right-handed system.

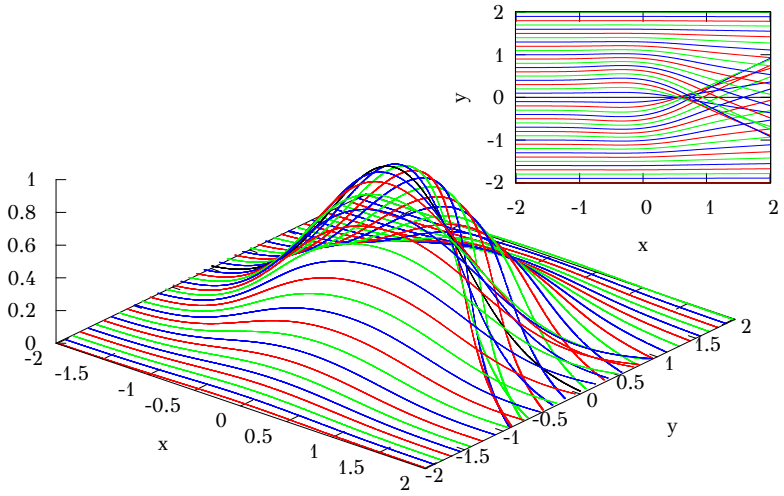

Figure 6: Geodesic lines on a Gaussian bump found using our developed integrator. The integrator solves Newton's equations of motion in the presence of Riemannian curvature symplectically. In the absence of a force term Newton's equations of motions are equal to the geodesic equation.

Chapter 1.

Chiral texture in toroidal liquid crystals

Nematic liquid crystals can be thought of as liquids compounds of elongated particles which tend to be axially aligned. The elongated particles can be thought of as rod-like molecules with a typical size of few nanometers. The nematic order refers to the alignment in the orientation of the rods, which is the ground state of nematic liquid crystals. Mathematically, nematic liquid crystals can be described by a double headed vector field $\mathbf{n}(\mathbf{x})$, often called the director field. The director field is assumed to align with the average orientation of the particles in a small patch. As the particles — or rods — are biaxially symmetric, their orientation is locally invariant under a rotation of π radians. Hence, an energy $F[\mathbf{n}(\mathbf{x})]$ describing such particles should be invariant under the following transformation:

$$F[\mathbf{n}(\mathbf{x})] = F[-\mathbf{n}(\mathbf{x})]. \tag{1.1}$$

As the director field purely contains orientational information we will assume $\mathbf{n}(\mathbf{x})^2 = 1$ for any given $\mathbf{x}$; the directory field is a unitary vector field.

As nematic liquid crystals align to yield the lowest-energy configuration, any distortion from this alignment comes at an energetic cost [119, 132, 154]. To account for these energetic costs, a phenomenological energy is constructed, called the Frank free energy $F[\mathbf{n}(\mathbf{x})]$. As the Frank free energy is essentially an elastic energy, for a strain u_{ij} the most general form is given by

$$F = \tfrac{1}{2} \int \mathrm{d}V \, K_{ijkl} u_{ij} u_{kl}, \tag{1.2}$$

where K_{ijkl} is the elastic tensor. In the case of a nematic, the strain is given by the gradient of the nematic director field $u_{ij} = \nabla_i n_j$, which yields

$$F = \tfrac{1}{2} \int \mathrm{d}V \, K_{ijkl} \nabla_i n_j \nabla_k n_l. \tag{1.3}$$

In three dimensions, the elastic tensor K_{ijkl} has only three independent components in the bulk due to the biaxial properties of the energy and the unitariness of $\mathbf{n}(\mathbf{x})$. This results in three terms. The first term, the splay energy, is given by

$$F_1 = \tfrac{1}{2} \int \mathrm{d}V \, K_1 (\nabla \cdot \mathbf{n})^2. \tag{1.4}$$

The second term, the twist energy is given by

$$F_2 = \tfrac{1}{2} \int \mathrm{d}V \, K_2 (\mathbf{n} \cdot \nabla \times \mathbf{n})^2. \tag{1.5}$$

The third term, the bend energy is given by

$$F_3 = \tfrac{1}{2} \int \mathrm{d}V \, K_3 (\mathbf{n} \times \nabla \times \mathbf{n})^2. \tag{1.6}$$

It turns out, however, that there is also a physically relevant surface term: saddle-splay, given by: [119]

$$F_{24} = -K_{24} \int \mathbf{dS} \cdot \left(\mathbf{n} \nabla \cdot \mathbf{n} + \mathbf{n} \times \nabla \times \mathbf{n} \right). \tag{1.7}$$

The total Frank free energy for nematic liquid crystals confined in a space is the sum of all these energies, as given by eq. (1.8).

At low temperatures, the nematic liquid crystal would like to align completely throughout space, as it yields the lowest-energy state. This is, however, not always possible due to the geometry and topology of the confining space.

1.1 Toroidal confinements

The confinement of liquid crystals in non-trivial geometries forms a rich and interesting area of study because the preferred alignment at the *curved* bounding surface induces bulk distortions of the liquid crystal — that is, the boundary conditions *matter*. This results in a great diversity of assemblies and

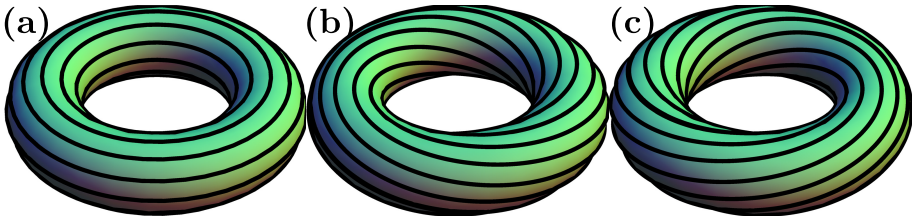

Figure 1.1: Schematic of (a) achiral, (b) right-handed and (c) left-handed toroidal nematic liquid crystals. The black lines are director field lines on the bounding torus.

mechanical phenomena [72, 130, 137, 138, 146]. Water droplets dispersed in a nematic liquid crystal interact and assemble into chains due to the presence of the anisotropic host fluid [139, 141, 145], defect lines in cholesteric liquid crystals can be knotted and linked around colloidal particles [71, 77, 100, 101], and surface defects in spherical nematic shells can abruptly migrate when the thickness inhomogeneity of the shell is altered [50, 73]. In these examples, spherical droplets (or colloids), either filled with — or dispersed in — a liquid crystal, create architectures arising from their coupling to the orientational order of the liquid crystal. Nematic structures where the bounding surface of the colloid or the liquid crystal droplet is topologically different from a sphere have also been studied [45, 51, 60]. Though there has been much interest in the interplay between order and toroidal geometries [45, 63, 74, 90, 96, 97, 112, 114, 135], it was only recently that experimental realisations of nematic liquid crystal droplets with toroidal boundaries were reported [55, 86]. Polarised microscopy revealed a twisted nematic orientation in droplets with planar degenerate (tangential) boundary conditions, despite the achiral nature of nematics. This phenomenon, which we will identify as spontaneous chiral symmetry breaking♠, is subject of theoretical study in this article. The chirality of nematic toroids is displayed by the local average orientation of the nematic molecules, called the director field and indicated by the unit vector $\mathbf{n}$. Motivated by experiment, we will assume this director field to be aligned in the tangent plane of the bounding torus. Figure 1.1a shows an achiral nematic toroid which has its fieldlines aligned along the azimuthal direction, $\hat{\phi}$. In contrast, the chiral nematic toroids in fig. 1.1 b and fig. 1.1 c show a right- and left-handedness, respectively, when following the fieldlines anticlockwise (in the azimuthal direction).

♠Technically, it is spontaneous *achiral* symmetry breaking since the symmetry is the *lack* of chirality. We will, however, conform to the standard convention.

The origin of the chirality lies in two elastic effects of geometric confinement. Firstly, there is a trade-off between bend and twist deformations. Secondly, another type of director distortion called saddle-splay couples the director to the curvature of the boundary, and can consequently favor the chiral state.

These nematic toroids share similarities with polymer bundles [53, 75, 83, 92, 93, 114, 143]. In fact, twisted DNA toroids have been analysed with liquid crystal theory [68, 75, 114]. Under the appropriate solvent conditions DNA condenses into toroids [143, 166]. These efficient packings of genetic material are interesting as vehicles in therapeutic gene delivery; it has been argued [114] that a twist in DNA toroids, for which there are indications both in simulations [122, 131] and experiments [118], would unfold more slowly and could therefore be beneficial for this delivery process. Thus, besides a way to engineer complex structures, the theory of geometrically confined liquid crystals may also provide understanding of biological systems.

The organisation of this article is as follows. In section 1.2 we will discuss our analytical method, which involves a single variational ansatz only for the director fields of both chiral and achiral toroidal nematics. In section 1.3 we will consider its energetics in relation to the slenderness, elastic anisotropies, cholesteric pitch and external fields, and discuss the achiral–chiral transition in the light of the mean field treatment of the Ising model.

1.2 Toroidal director fields

1.2.1 Free energy of a nematic toroid

We will study the general case in which the director lies in the tangent plane of the boundary assuming that the anchoring is strong so that the only energy arises from elastic deformations captured by the Frank free energy functional [119, 154]:

$$\begin{aligned} F[\mathbf{n}(\mathbf{x})] = \frac{1}{2}\int \mathrm{d}V \Big(& K_1(\nabla\cdot\mathbf{n})^2 \\ & + K_2(\mathbf{n}\cdot\nabla\times\mathbf{n})^2 + K_3(\mathbf{n}\times\nabla\times\mathbf{n})^2\Big) \\ & - K_{24}\int \mathbf{dS}\cdot(\mathbf{n}\nabla\cdot\mathbf{n}+\mathbf{n}\times\nabla\times\mathbf{n}), \end{aligned} \tag{1.8}$$

where $\mathrm{d}\mathbf{S} = \boldsymbol{\nu}\,\mathrm{d}S$ is the area element, with $\boldsymbol{\nu}$ the unit normal vector (outward pointing) and where $\mathrm{d}V$ is the volume element. Due to the anisotropic nature of the nematic liquid crystal, this expression contains three bulk elastic moduli, K_1, K_2, K_3, rather than a single one for fully rotationally symmetric systems. In addition, there is a surface elastic constant K_{24}. K_1, K_2, K_3 and K_{24} measure the magnitude of splay, twist, bend and saddle-splay distortions, respectively. We now provide a geometrical interpretation of the saddle-splay distortions. Firstly, observe that under perfect planar anchoring conditions $\mathbf{n} \cdot \boldsymbol{\nu} = 0$, so the first term in the saddle-splay energy does not contribute:

$$F_{24} = -K_{24} \int \mathrm{d}S\; \boldsymbol{\nu} \cdot (\mathbf{n} \times \nabla \times \mathbf{n})\,. \tag{1.9}$$

This remaining term in the saddle-splay energy is often rewritten as

$$F_{24} = K_{24} \int \mathrm{d}S\; \boldsymbol{\nu} \cdot (\mathbf{n} \cdot \nabla)\,\mathbf{n}, \tag{1.10}$$

because

$$\begin{aligned} (\mathbf{n} \times \nabla \times \mathbf{n})_a &= \epsilon_{abc} n_b \epsilon_{cpq} \partial_p n_q \\ &= (\delta_{ap}\delta_{bq} - \delta_{aq}\delta_{bp})\, n_b \partial_p n_q \\ &= -n_b \partial_b n_a \end{aligned} \tag{1.11}$$

where in the last line the identity $0 = \partial_a (1) = \partial_a (n_b n_b) = 2 n_b \partial_a n_b$ is used. In other words, the bend is precisely the curvature of the integral curves of $\mathbf{n}$. Employing the product rule of differentiation $0 = \partial_a (\nu_b n_b) = \nu_b \partial_a n_b + n_b \partial_a \nu_b$ yields:

$$F_{24} = -K_{24} \int \mathrm{d}S\; \mathbf{n} \cdot (\mathbf{n} \cdot \nabla)\,\boldsymbol{\nu}. \tag{1.12}$$

Upon writing $\mathbf{n} = n_1 \boldsymbol{e}_1 + n_2 \boldsymbol{e}_2$, with $\boldsymbol{e}_1$ and $\boldsymbol{e}_1$ two orthonormal basis vectors in the plane of the surface, one obtains

$$F_{24} = K_{24} \int \mathrm{d}S\; n_i L_{ij} n_j, \tag{1.13}$$

where we note that $i, j = 1, 2$ (rather than running till 3). Thus the nematic director couples to the extrinsic curvature tensor [126], defined as

$$L_{ij} = -\boldsymbol{e}_i \cdot (\boldsymbol{e}_j \cdot \nabla)\,\boldsymbol{\nu}. \tag{1.14}$$

If $\boldsymbol{e}_1$ and $\boldsymbol{e}_2$ are in the directions of principal curvatures, κ_1 and κ_2, respectively, one finds:

$$F_{24} = K_{24} \int dS \left(\kappa_1 n_1^2 + \kappa_2 n_2^2\right). \tag{1.15}$$

We conclude that the saddle-splay term favors alignment of the director along the direction with the smallest principal curvature if $K_{24} > 0$. The controversial surface energy density $K_{13}\mathbf{n}\nabla \cdot \mathbf{n}$ is sometimes incorporated in eq. (1.8), but is in our case irrelevant, because the normal vector is perpendicular to $\mathbf{n}$, and so $\mathbf{n} \cdot \boldsymbol{\nu} = 0$.

We will consider a nematic liquid crystal confined in a handle body bounded by a torus given by the following implicit equation for the Cartesian coordinates x, y, and z:

$$\left(R_1 - \sqrt{x^2 + y^2}\right)^2 + z^2 \leq R_2^2. \tag{1.16}$$

Here, R_1 and R_2 are the large and small radii, respectively, of the circles that characterise the outer surface: a torus obtained by revolving a circle of radius R_2 around the z-axis (fig. 1.2).

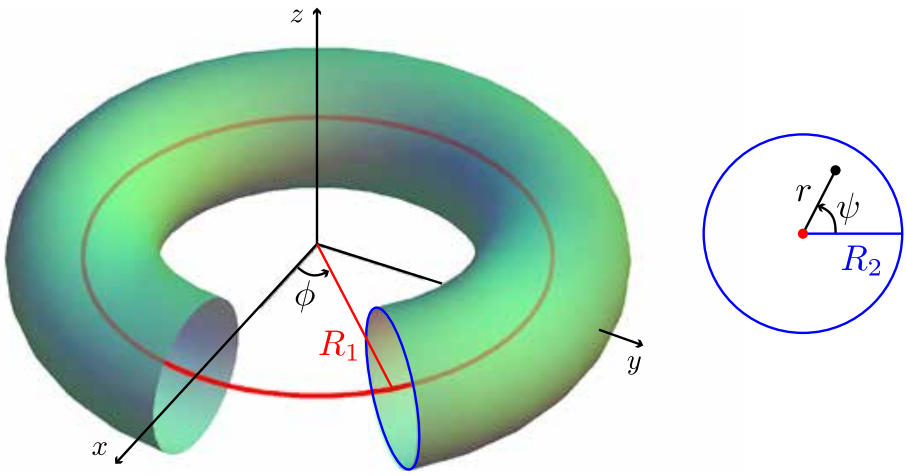

Figure 1.2: *Left panel*: Schematic of the boundary of the geometry-specified eq. (1.16) including graphical definitions of ϕ and R_1. The torus is characterised by a large (red) and a small (blue) circle. The large circle, or centerline, has radius R_1. *Right panel*: Schematic of a cut including graphical definitions of r, ψ and R_2.

We can conveniently parametrise this solid torus by the coordinates $r \in [0, R_2]$, $\phi \in [0, 2\pi)$ and $\psi \in [0, 2\pi)$ (illustrated in fig. 1.2):

$$x = (R_1 + r\cos\psi)\cos\phi, \tag{1.17}$$

$$y = (R_1 + r\cos\psi)\sin\phi, \tag{1.18}$$

$$z = r\sin\psi. \tag{1.19}$$

The metric reads:

$$g_{\mu\nu} = \begin{pmatrix} 1 & 0 & 0 \\ 0 & (R_1 + r\cos\psi)^2 & 0 \\ 0 & 0 & r^2 \end{pmatrix}, \tag{1.20}$$

with $\mu, \nu \in \{r, \phi, \psi\}$. It follows that $\mathrm{d}\mathbf{S} = \boldsymbol{\nu}\sqrt{g}\ \mathrm{d}\psi\,\mathrm{d}\phi$ and $\mathrm{d}V = \sqrt{g}\ \mathrm{d}r\,\mathrm{d}\psi\,\mathrm{d}\phi$, where $g = \det g_{\mu\nu}$.

For a torus the ϕ and ψ directions are the principal directions. The curvature along the ψ direction is negative everywhere (measured with respect to the outward pointing normal) and the smallest of the two, so when $K_{24} > 0$, the director tends to wind along the small circle with radius R_2.

1.2.2 Double twist

To minimise the Frank energy we formulate a variational ansatz built on several simplifying assumptions [114]. We consider a director field which has no radial component (i.e. $n_r = 0$), is tangential to the centerline ($r = 0$), and is independent of ϕ. Furthermore, since we expect the splay (K_1) distortions to be unimportant, we first take the field to be divergence-free (i.e. $\nabla \cdot \mathbf{n} = 0$). Recalling that in curvilinear coordinates the divergence is $\nabla \cdot \mathbf{n} = \frac{1}{\sqrt{g}}\partial_\mu\left(\sqrt{g}n^\mu\right)$, we write

$$n_\psi = \frac{f(r)\,R_1}{\sqrt{g_{\phi\phi}}}, \tag{1.21}$$

where the other terms in $\sqrt{g}$ play no role as they are independent of ψ. The ϕ-component of the director follows from the normalisation condition. For the radial dependence of $f(r)$ we make the simplest choice,

$$f(r) = \frac{\omega r}{R_2}, \tag{1.22}$$

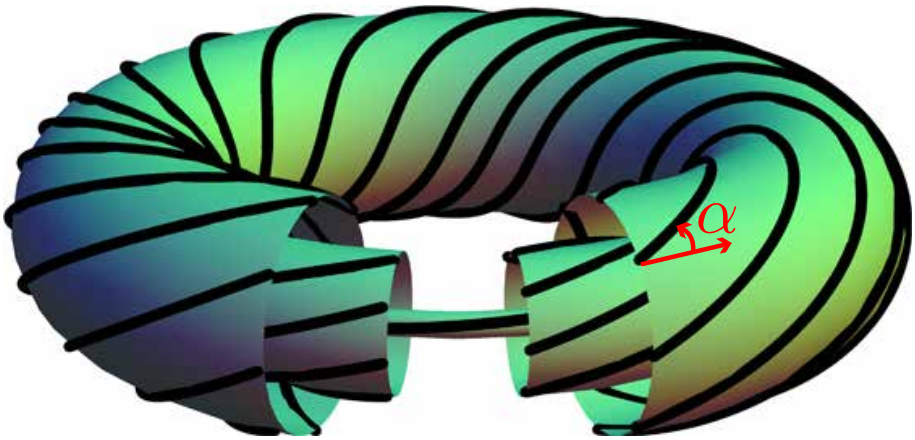

Figure 1.3: Schematic of the ansatz for the director fieldlines ($\omega = 0.6$ and $\xi = 3$), displaying a twist when going radially outward, including a graphical definition of α.

and obtain

$$n_\psi = \omega \frac{\xi r/R_2}{\xi + \frac{r}{R_2}\cos\psi}, \tag{1.23}$$

where we have introduced $\xi \equiv R_1/R_2$, the slenderness or aspect ratio of the torus. The variational parameter ω governs the chirality of the toroidal director field. If $\omega = 0$ the director field corresponds to the axial configuration in fig. 1.1 a. The sign of ω determines the chirality: right-handed when $\omega > 0$ (fig. 1.1 c) and left-handed when $\omega < 0$ (fig. 1.1 b). The magnitude of ω determines the degree of twist. Note that the direction of twist is in the radial direction, as illustrated in fig. 1.3. Therefore the toroidal nematic is doubly twisted, resembling the cylindrical building blocks of the blue phases [119, 154]. It may be useful to relate ω to a quantity at the surface, say the angle, α, that the director makes with $\hat{\phi}$. For the ansatz, this angle will be different depending on whether one measures at the inner or outer part of the torus, but for large ξ we find:

$$\omega \approx n_\psi \left(r = R_2\right) = \sin\alpha. \tag{1.24}$$

1.3 Chiral symmetry breaking

1.3.1 Results for divergence-free field

Since ω only determines the chirality of the double-twisted configuration but not the amount of twist, the free energy is invariant under reversal of the sign of ω, i.e. $F(-\omega) = F(\omega)$. This mirror symmetry allows us to write down a Landau-like expansion in which F only contains even powers of ω,

$$F = a_0(\{K_i\}, \xi) + a_2(\{K_i\}, \xi)\,\omega^2 + a_4(\{K_i\}, \xi)\,\omega^4 + \mathcal{O}\left(\omega^6\right) \tag{1.25}$$

where $\{K_i\}$ is the set of elastic constants.[♠] If the coefficient $a_2 > 0$, the achiral nematic toroid ($\omega_{eq} = 0$) corresponds to the minimum of F provided that $a_4 > 0$. In contrast, the mirror symmetry is broken spontaneously whenever $a_2 < 0$ (and $a_4 > 0$). The achiral–chiral critical transition at $a_2 = 0$ belongs to the universality class of the mean-field Ising model. Therefore, we can immediately infer that the value of the critical exponent β in $\omega_{eq} \sim (-a_2)^{\beta}$ is $\frac{1}{2}$. To obtain the dependence of the coefficients a_i on the elastic constants and ξ, we need to evaluate the integral in eq. (1.8). For the bend, twist and saddle-splay energies we find:

$$\begin{aligned}\frac{F_3}{K_3 R_1} = {} & \frac{2\pi^2}{\xi}\left(\xi - \sqrt{\xi^2-1}\right) \\ & + \pi^2 \frac{\xi - 9\xi^3 + 6\xi^5 + 6\xi^2\sqrt{\xi^2-1} - 6\xi^4\sqrt{\xi^2-1}}{(\xi^2-1)^{\frac{3}{2}}}\omega^2 + \mathcal{O}\left(\omega^4\right),\end{aligned} \tag{1.26}$$

$$\frac{F_2}{K_2 R_1} = 4\pi^2 \frac{\xi^3}{(\xi^2-1)^{\frac{3}{2}}}\omega^2 + \mathcal{O}\left(\omega^6\right), \tag{1.27}$$

$$\frac{F_{24}}{K_{24} R_1} = -4\pi^2 \frac{\xi^3}{(\xi^2-1)^{\frac{3}{2}}}\omega^2. \tag{1.28}$$

Though the bend and twist energies are Taylor expansions in ω, the saddle-splay energy is exact. The large ξ asymptotic behavior of the elastic energy reads:[♡]

$$\frac{F}{K_3 R_1} \approx \frac{\pi^2}{\xi^2} + 4\pi^2\left(k - \frac{5}{16\xi^2}\right)\omega^2 + \frac{\pi^2}{2}\omega^4 + \mathcal{O}\left(\omega^6\right), \tag{1.29}$$

[♠] Explicitly: $\{K_i\} = \{K_1, K_2, K_3, K_{24}\}$

[♡] The fourth-order term in the bend energy for general ξ, that reduces to $\frac{\pi^2}{2} K_3 R_2 \xi \omega^4$ in eq. (1.29), is not given in eq. (1.26), because it is too lengthy.

where $k \equiv \frac{K_2 - K_{24}}{K_3}$ is the elastic anisotropy in twist and saddle-splay. The achiral configuration contains only bend energy. For sufficiently thick toroids, bend distortions are exchanged with twist and the mirror symmetry is broken spontaneously, as expected; see fig. 1.4. Interestingly, if $K_{24} > 0$ the saddle-

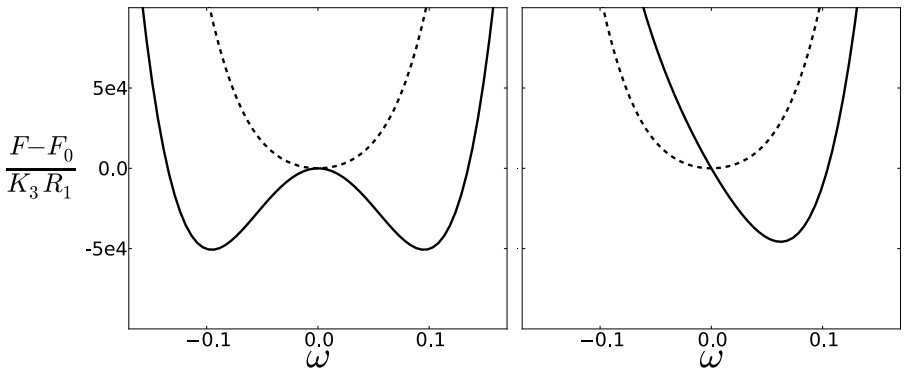

Figure 1.4: *Left panel:* The free energy as a function of ω for $\xi = 6$ (dashed) and $\xi = 5$ (solid), when $(K_2 - K_{24})/K_3 = 10^{-2}$. For $\xi = 5$ the chiral symmetry is broken spontaneously: the minimum values of the energy occur for nonzero ω. *Right panel:* The free energy as a function of ω for $q = 0$ (dashed) and $qR_2 = 10^{-3}$ (solid), when $\xi = 6$, $(K_2 - K_{24})/K_3 = 10^{-2}$ and $K_2/K_3 = 0.3$. For $qR_2 = 10^{-3}$ the chiral symmetry is broken explicitly: the minimum value of the energy occurs for a nonzero ω, because F contains a linear term in ω.

splay deformations screen the cost of twist. If $K_{24} < 0$ on the other hand, there is an extra penalty for twisting. Setting the coefficient of the ω^2 term equal to zero yields the phase boundary:

$$\begin{aligned} k_c &= \frac{-1 + 9\xi_c^2 - 6\xi_c^4 - 6\xi_c\sqrt{\xi_c^2 - 1} + 6\xi_c^3\sqrt{\xi_c^2 - 1}}{4\xi_c^2} \\ &\approx \frac{5}{16\xi_c^2} \qquad \text{if } \xi \gg 1. \end{aligned} \tag{1.30}$$

Figure 1.5 shows the phase diagram as a function of ξ and k. It is interesting to look at the critical behavior. The degree of twist close to the transition is

$$\alpha_{eq} \approx \omega_{eq} \approx 2\left(\frac{5}{16\xi^2} - k\right)^{1/2}, \tag{1.31}$$

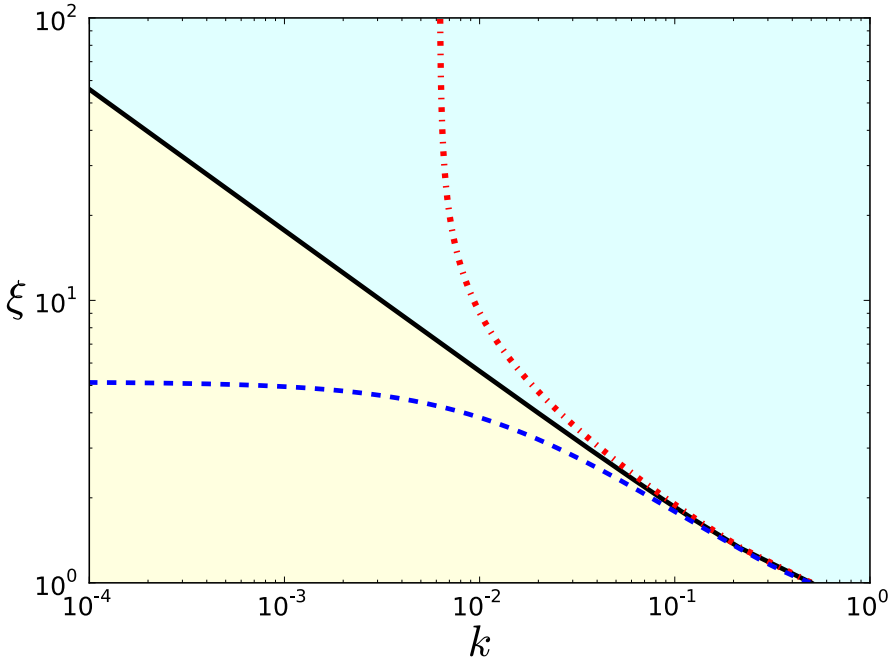

Figure 1.5: Phase diagram as a function of the toroidal slenderness and the elastic anisotropy in twist and saddle-splay constant, $k \equiv (K_2 - K_{24})/K_3$. The twisted (yellow region) and axial (cyan region) configuration are separated by a boundary line in the absence of an external field (solid black), when $\mathbf{H} = \sqrt{0.1K_3}/\left(\sqrt{\chi_a}R_2\right)\hat{\phi}$ (dashed blue) and when $\mathbf{H} = \sqrt{0.1K_3}/\left(\sqrt{\chi_a}R_2\right)\hat{\mathbf{z}}$ (dash-dotted red).

where we have used the identity $\sin\alpha_{eq} \approx \alpha_{eq}$ for small α_{eq}. Upon expanding $\xi = \xi_c + \delta\xi$ (with $\delta\xi < 0$) and $k = k_c + \delta k$ (with $\delta k < 0$) around their critical values ξ_c and k_c, respectively, we obtain the following scaling relations, while keeping k and ξ fixed, respectively:

$$\alpha_{eq} \approx \frac{\sqrt{5}}{2}\left(-\frac{\delta\xi}{\xi_c^3}\right)^{1/2}, \tag{1.32}$$

$$\alpha_{eq} \approx 2(-\delta k)^{1/2}. \tag{1.33}$$

Equations (1.32) and (1.33) are analogues to $m_{eq} \sim (-t)^{1/2}$, relating the equilibrium magnetization, m_{eq} (in the ferromagnetic phase of the Ising model in Landau theory), to the reduced temperature, t.

1.3.2 Effects of external fields and cholesteric pitch

Due to the inversion symmetry of nematics, $F[\mathbf{n}] = F[-\mathbf{n}]$, an external magnetic field, $\mathbf{H}$, couples quadratically to the components of $\mathbf{n}$ rather than linearly as in spin systems. The magnetic free energy contribution reads

$$F_m = -\frac{\chi_a}{2}\int \mathrm{d}V(\mathbf{n}\cdot\mathbf{H})^2, \tag{1.34}$$

where $\chi_a = \chi_\parallel - \chi_\perp$, the difference between the magnetic susceptibilities parallel and perpendicular to $\mathbf{n}$. Consequently, there is no explicit chiral symmetry breaking due to $\mathbf{H}$ as is the case in the Ising model. Rather, $\mathbf{H}$ shifts the location of the critical transition in the phase diagram. For concreteness, we will consider two different applied fields, namely a uniaxial field $\mathbf{H} = H_z\hat{\mathbf{z}} = H_z\sin(\psi)\hat{\mathbf{r}} + H_z\cos(\psi)\hat{\boldsymbol{\psi}}$ and an azimuthal field $\mathbf{H} = H_\phi\hat{\boldsymbol{\phi}}$, as if produced by a conducting wire going through the hole of the toroid. For $\mathbf{H} = H_z\hat{\mathbf{z}}$ we find:

$$\begin{aligned} F_m &= -\pi^2\chi_a H_z^2 R_1 R_2^2 \xi^2\left(2\xi\left(\xi - \sqrt{\xi^2-1}\right) - 1\right)\omega^2 \\ &\approx -\frac{\pi^2}{4}\chi_a H_z^2 R_1 R_2^2\omega^2 \qquad \text{if } \xi \gg 1. \end{aligned} \tag{1.35}$$

For a positive χ_a this energy contribution is negative, implying that a larger area in the phase diagram is occupied by the twisted configuration. The new phase boundary — fig. 1.5 — which is now a surface in the volume spanned by ξ, k and H_z instead of a line, reads

$$\begin{aligned} k_c &= \frac{1}{(4\xi_c^2)}\left[-1+9\xi_c^2-6\xi_c^4-6\xi_c\sqrt{\xi_c^2-1}+6\xi_c^3\sqrt{\xi_c^2-1}\right. \\ &\quad \left.-\frac{\chi_a(H_z)_c^2R_2^2}{K_3}\left(\xi_c^2-1\right)\xi_c\left(-2\xi_c+2\xi_c^3+\sqrt{\xi_c^2-1}-2\xi_c^2\sqrt{\xi_c^2-1}\right)\right] \\ &\approx \frac{5}{16\xi_c^2}+\frac{\chi_a(H_z)_c^2R_2^2}{16K_3} \quad \text{if } \xi \gg 1. \end{aligned} \tag{1.36}$$

In contrast, an azimuthal field favors the axial configuration, contributing a positive ω^2-term to the energy when $\chi_a > 0$:

$$\begin{aligned} F_m &= -\pi^2\chi_a H_\phi^2 R_1 R_2^2+\frac{2\pi^2}{3}\chi_a H_\phi^2 R_1 R_2^2\xi \\ &\quad\times\left(2\xi^2\left(\xi-\sqrt{\xi^2-1}\right)-\sqrt{\xi^2-1}\right)\omega^2 \\ &\approx -\pi^2\chi_a H_\phi^2 R_1 R_2^2+\frac{\pi^2}{2}\chi_a H_\phi^2 R_1 R_2^2\omega^2 \quad \text{if } \xi \gg 1. \end{aligned} \tag{1.37}$$

Consequently, this yields a shifted phase boundary, see fig. 1.5:

$$\begin{aligned} k_c &= \frac{1}{(4\xi_c^2)}\left[-1+9\xi_c^2-6\xi_c^4-6\xi_c\sqrt{\xi_c^2-1}+6\xi_c^3\sqrt{\xi_c^2-1}\right. \\ &\quad \left.-\frac{2\chi_a(H_\phi)_c^2R_2^2}{3K_3}\left(\xi_c^2-1\right)\left(1+\xi_c^2-2\xi_c^4+2\xi_c^3\sqrt{\xi_c^2-1}\right)\right] \\ &\approx \frac{5}{16\xi_c^2}-\frac{\chi_a(H_\phi)_c^2R_2^2}{8K_3} \qquad \text{if } \xi \gg 1. \end{aligned} \tag{1.38}$$

Similar results of eq. (1.35) to eq. (1.38) hold for an applied electric field $\mathbf{E}$ instead of a magnetic field; the analog of χ_a is the dielectric anisotropy. There could however be another physical mechanism at play in a nematic insulator, namely the flexoelectric effect [154, 169]. Splay and bend deformations induce a polarisation

$$\mathbf{P} = e_1\mathbf{n}\nabla\cdot\mathbf{n}+e_3\mathbf{n}\times\nabla\times\mathbf{n}, \tag{1.39}$$

where e_1 and e_3 are called the flexoelectric coefficients. Note that the first term in eq. (1.39) is irrelevant for the divergence-free ansatz. A coupling of $\mathbf{P}$ with $\mathbf{E}$:

$$F_P = -\int dV \mathbf{P} \cdot \mathbf{E} \tag{1.40}$$

could potentially lead to a shift of the transition. In the particular case when $\mathbf{E} = E_z\hat{\mathbf{z}} = E_z \sin(\psi)\hat{\mathbf{r}} + E_z \cos(\psi)\hat{\boldsymbol{\psi}}$, however, the ω^2 contribution from eq. (1.40) vanishes, thus not yielding such a shift.

If we now consider toroidal cholesterics rather than nematics, the chiral symmetry is broken explicitly, fig. 1.4. A cholesteric pitch of $2\pi/q$ gives a contribution to the free energy of:

$$F_{cn} = K_2\, q \int \mathrm{d}V \;\; \mathbf{n} \cdot \nabla \times \mathbf{n}. \tag{1.41}$$

Substituting eq. (1.23) yields:

$$\begin{aligned} F_{cn} &= -8\pi^2 K_2\, q\, R_1 R_2\, \xi \left(\xi - \sqrt{\xi^2 - 1}\right) \omega + \mathcal{O}\left(\omega^3\right) \\ &\approx -4\pi^2 K_2\, q\, R_1 R_2\, \omega + \mathcal{O}\left(\omega^3\right) \qquad \text{if } \xi \gg 1. \end{aligned} \tag{1.42}$$

Therefore, at the critical line in the phase diagram spanned by k and ξ, the degree of twist or surface angle scales (for large ξ) with the helicity of the cholesteric as:

$$\alpha_{eq} \approx \left(2K_2 R_2\, q/K_3\right)^{1/3} \sim q^{1/3}. \tag{1.43}$$

This is the analog scaling relation of $m_{eq} \sim H^{1/3}$ in the mean-field Ising model.

1.3.3 Results for the two-parameter ansatz

Motivated by experiments [55], we can introduce an extra variational parameter γ to allow for splay deformations, in addition to ω:

$$n_\psi = \omega \frac{\xi r/R_2}{\xi + \gamma \frac{r}{R_2} \cos\psi}. \tag{1.44}$$

(Note that eq. (1.23) is recovered by setting $\gamma = 1$ in eq. (1.44).) In section 1.3.1 analytical results for $\gamma = 1$ were presented. In this subsection we will slightly improve these results by finding the optimal value of γ numerically. First, we discretize the azimuthally symmetric director field in the r and ψ direction.

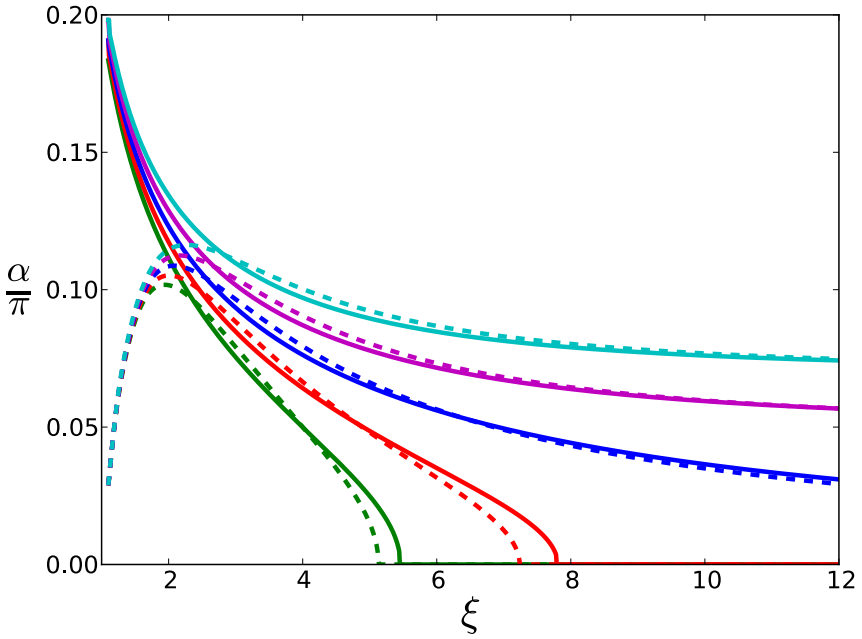

Figure 1.6: Twist angle α (in units of π) at $\psi = \pi/2$ versus the slenderness ξ for $k = 0.012$ (green), $k = 0.006$ (red), $k = 0$ (blue), $k = -0.006$ (magenta) and $k = -0.012$ (cyan). The dashed lines represent α for $\gamma = 1$, the solid lines represent α found for the optimal γ.

Next, we compute the Frank free energy density eq. (1.8) by taking finite differences [158] — see appendix section G.1 for details — of the discretized nematic field. After summation over the volume elements the Frank free energy will become a function of ω and γ for a given set of elastic constants and a given aspect ratio. Because of the normalisation condition on $\mathbf{n}$, the allowed values for ω and γ are constrained to the open diamond-like interval for which $-\xi < \gamma < \xi$ and $\frac{|\gamma|-\xi}{\xi} < \omega < \frac{\xi-|\gamma|}{\xi}$ holds.

The minima of the energy surface can be found by employing the conjugate gradient method — see appendix N for details. We have looked at the difference between the $\gamma = 1$ case and the case where the value of γ is chosen to minimise the energy. This was done for various choices of k. We have chosen the material properties of 5CB, i.e. $K_1 = 0.64K_3$ and $K_2 = 0.3K_3$ [119]. The value of K_{24} has not been so accurately determined, but previous measurements [55, 147, 151, 152, 153, 155] seem to suggest that $K_{24} \approx K_2$, corresponding to $k \approx 0$.

We are interested in how the phase boundary changes when the variational parameter γ is introduced. Therefore, the twist angle α, evaluated at the surface of the torus at $\psi = \frac{\pi}{2}$, versus the slenderness ξ is shown in fig. 1.6. For the particular choices of k there are two noticeable differences between the single-parameter ansatz and the two-parameter ansatz. Firstly, for small values of ξ, α is changed significantly. Secondly, for larger values of ξ we see that if there is a chiral–achiral phase transition, ξ_c is shifted by a small amount. In fig. 1.7 we further investigate how introducing γ influences the phase boundary, by plotting the phase boundary as a function of the toroidal slenderness ξ and elastic anisotropy k for both γ as a variational parameter (solid) and for $\gamma = 1$ (dashed). Observe that, for both the small ξ and small k regime, the difference is significant.

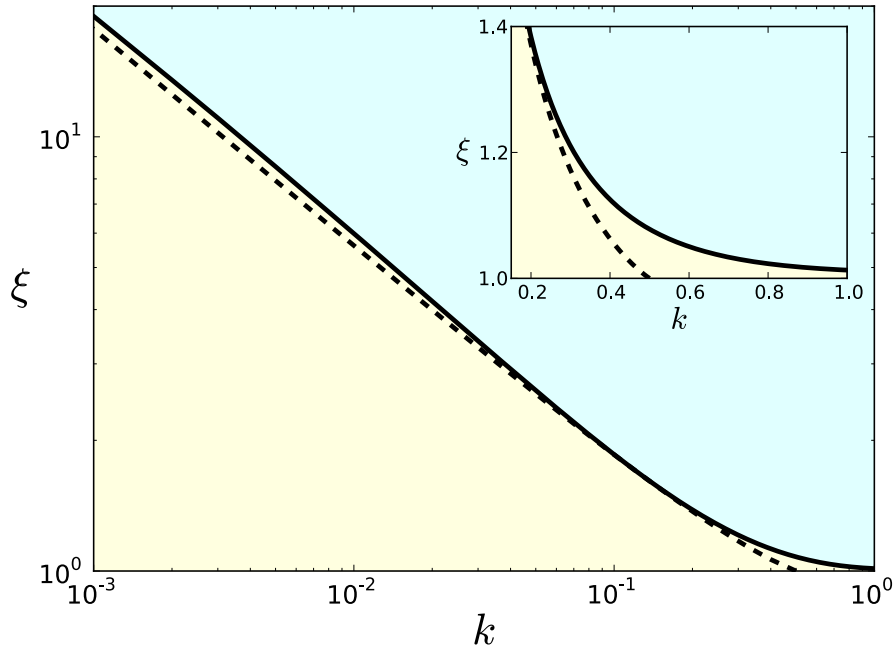

Figure 1.7: The phase boundary as a function of the toroidal slenderness ξ and elastic anisotropy k for γ as a variational parameter (solid) and for $\gamma = 1$ (dashed). The inset zooms in on the phase boundary for small ξ.

1.4 Experiments

Chiral symmetry breaking in toroidal nematics has been verified experimentally at Georgia Tech in the Fernandez-Nieves lab [55]. The experiment was done by first developing a method to construct nematic liquid crystals in a toroidal shape, and then exploiting the light-polarising properties of liquid crystals to measure the presence of a twist. Additionally, higher-order tori — tori with multiple handles — were measured as well.

The construction of the toroidal nematic droplet is done by injecting 5CB♠ through a rotating needle into a bath. The bath contains a mixture with a high yield stress. The mixture consists of 64.5 wt% ultra pure water, 30 wt% ethanol, 3 wt% glycerin, 1.5 wt% polyacrylamide microgels (carbopol ETD 2020), and 1 wt% polyvinyl alcohol. The polyvinyl alcohol ensures that the nematic liquid crystals align tangentially at the boundary as confirmed by making spherical droplets and checking their bipolar character. Also the continuous phase is neutralized to pH 7, where the sample transmission is more than 90% [125]. The most relevant property of this phase, however, is its yield stress, σ_y. During formation of the torus — the injection of 5CB into the bath — the stresses involved are larger than σ_y and hence the continuous phase essentially behaves as if it were a liquid. The combination of the viscous drag exerted by the outer phase over the extruded liquid crystal and its rotational motion causes the liquid crystal to form a curved jet, as shown in fig. 1.8 A, which eventually closes onto itself, resulting in a toroidal nematic droplet, such as that shown in fig. 1.8 B in bright field and in fig. 1.8 C between cross-polarizers. Once the torus has been formed, the elasticity of the continuous phase provides the required force to overcome the surface tension force that would naturally tend to transform the toroidal droplet into a spherical droplet [94]. Remarkably, when these droplets are observed along their side view under cross polarizers, their central region remains bright irrespective of the orientation of the droplet with respect to the incident polarization direction, as shown in fig. 1.8 D–F; the corresponding bright-field images are shown in fig. 1.8 G–I. Note that for an axial torus with its director field along the tube, the cross-polarized image should appear black for an orientation of 0 and 90° with respect to the incident polarization direction. Hence our result is suggestive of a twisted structure. In fact, twisted bipolar droplets also have a central bright region, when viewed between cross-polarizers, irrespective of their orientation [146, 157, 161, 163].

♠5CB is short for 4-n-pentyl-4'-cyanobiphenyl which is a commonly used material for liquid crystals.

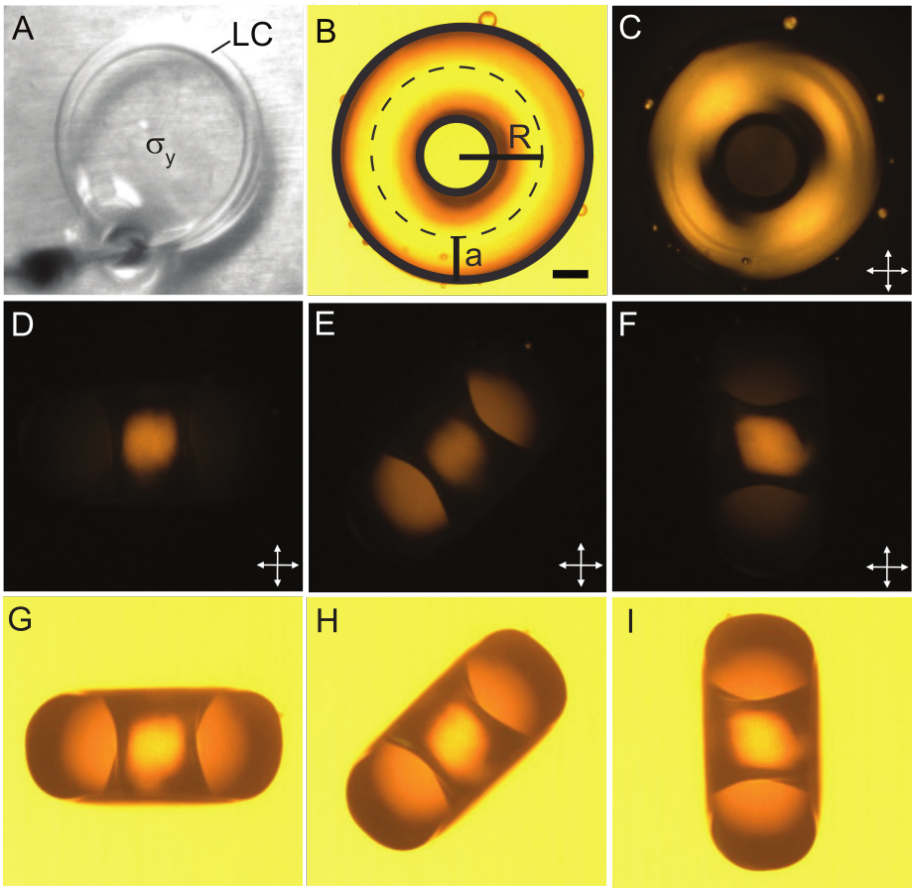

Figure 1.8: Toroidal droplets. (A) Formation of a toroidal liquid crystal droplet inside a material with yield stress σ_y. (B and C) The top view of a typical stable toroidal droplet of nematic liquid crystal, having tube and inner radii a and R, is shown in (B) when viewed in bright field and in (C) when viewed under cross-polarizers. (D–F) Side view of a typical toroidal droplet with $\xi = 1.8$ when viewed under cross-polarizers for orientations of 0°, 45°, and 90° with respect to the incident polarization direction. Note that the center part of the toroid remains bright irrespective of its orientation. (G–I) Corresponding bright-field images. The dark regions of the toroid in these images are due to light refraction. (Scale bar: 100μm.) [55]

The results are then quantified by measuring the twist angle in the toroidal droplets along the $\hat{z}$ direction, from $(r = a, \theta = 90^\circ)$ to $(r = a, \theta = 270^\circ)$, see fig. 1.2. The method relies on the fact that linearly polarized light follows the twist of a nematic liquid crystal if the polarization direction is either parallel or perpendicular to the nematic director at the entrance of the sample, provided the Mauguin limit is fulfilled [89]; the corresponding mode of propagation is referred to as extraordinary or ordinary waveguiding, respectively. We then image the torus is from above (fig. 1.9 A), rotate the polarizer to ensure that the incident polarization direction is parallel or perpendicular to the nematic director at $(r = a, \theta = 90^\circ)$, and then rotate the analyzer by an angle ϕ_{exit} with respect to the polarizer while monitoring the transmitted intensity, T. The minimum in T, shown in fig. 1.9 B, reflects the lack of light propagation through the analyzer, indicating that the incident polarization direction has rotated an amount τ such that it is perpendicular to the analyzer after exiting the torus at $(r = a, \theta = 270^\circ)$. The image of the torus in this situation exhibits four black regions where extinction occurs, as shown in fig. 1.9 C; these correspond to waveguiding of ordinary and extraordinary waves. It is along these regions that we measure T. The counterclockwise rotation of the incident polarization direction by an angle of -0.98 exactly corresponds to the twist angle of the nematic along the $\hat{z}$ direction through the center of the circular cross section. However, to increase the precision of our estimate, we fit the T vs. ϕ_{exit} results to the theoretically expected transmission [89], leaving τ as a free parameter. We find $\tau = (52.9 \pm 0.4)^\circ$ for $\xi = 3.5$. Moreover, within the experimentally accessed ξ-range, we find that the twist is nonzero and that it monotonously decreases with increasing aspect ratio, as shown in fig. 1.9 D. Remarkably, these features are captured by our theoretical calculations for large ξ, as shown by the dashed line in fig. 1.9 D. We note that the deviations of the experiment and the theory for small ξ result from the inadequacy of the ansatz in describing the highly twisted structures observed experimentally at these low values of ξ. This can be partially resolved by lifting the constraint that $\gamma = 1$. This introduces a second variational parameter in the ansatz, which allows the nematic field to splay. The result qualitatively captures the experimental trend for all aspect ratios, as shown by the solid line in fig. 1.9 D. By further comparing the experiment to the theory in the high ξ-region, we obtain a value for the saddle-splay elastic constant of $K_{24} = 1.02K_2$, which is slightly larger than the twist elastic constant, confirming our previous con-

clusions and supporting our interpretation on the relevance of saddle-splay distortions. However, our analysis cannot exclude the possibility of a slightly smaller value of K_{24} and hence of a twisted-to-axial transition for extremely large ξ.

1.5 Conclusions

We investigated spontaneous chiral symmetry breaking in toroidal nematic liquid crystals. As in the case of nematic tactoids [78, 116], the two ingredients for this macroscopic chirality are orientational order of achiral microscopic constituents and a curved confining boundary. This phenomenon occurs when both the aspect ratio of the toroid and $\frac{K_2-K_{24}}{K_3}$ are small. The critical behavior of this structural transition belongs to the same universality class as the ferromagnet–paramagnet phase transition in the Ising model in dimensions above the upper critical dimension. The analogues of the magnetization, reduced temperature and external field are the degree of twist (or surface angle), slenderness or $\frac{K_2-K_{24}}{K_3}$, and (cholesteric) helicity in liquid crystal toroids, respectively. Critical exponents are collected in table 1.1.

Liquid crystal toroid	Mean-field Ising model	Exponent
$\alpha_{eq} \sim (-\delta\xi)^{\beta}$	$m_{eq} \sim (-t)^{\beta}$	$\beta = 1/2$
$\alpha_{eq} \sim (-\delta k)^{\beta}$		
$\alpha_{eq} \sim q^{1/\delta}$	$m_{eq} \sim H^{1/\delta}$	$\delta = 3$

Table 1.1: Dictionary of the critical behavior of the structural transition in liquid crystal toroids and the thermal phase transition in the mean-field Ising model.

Thus, the helicity rather than an external field breaks the chiral symmetry explicitly. Remarkably, since an external field couples quadratically to the director field, it induces a shift of the phase boundary. An azimuthally aligned field favors the mirror symmetric director configuration, whereas a homogeneous field in the $\hat{z}$-direction favors the doubly twisted configuration.

A minimization of the elastic energy analogous to the one presented in this article for toroidal droplets has also been carried out for spherical droplets [161]. The analytical results qualitatively reproduce the twisted textures observed experimentally in spherical bipolar droplets [163]. In this case,

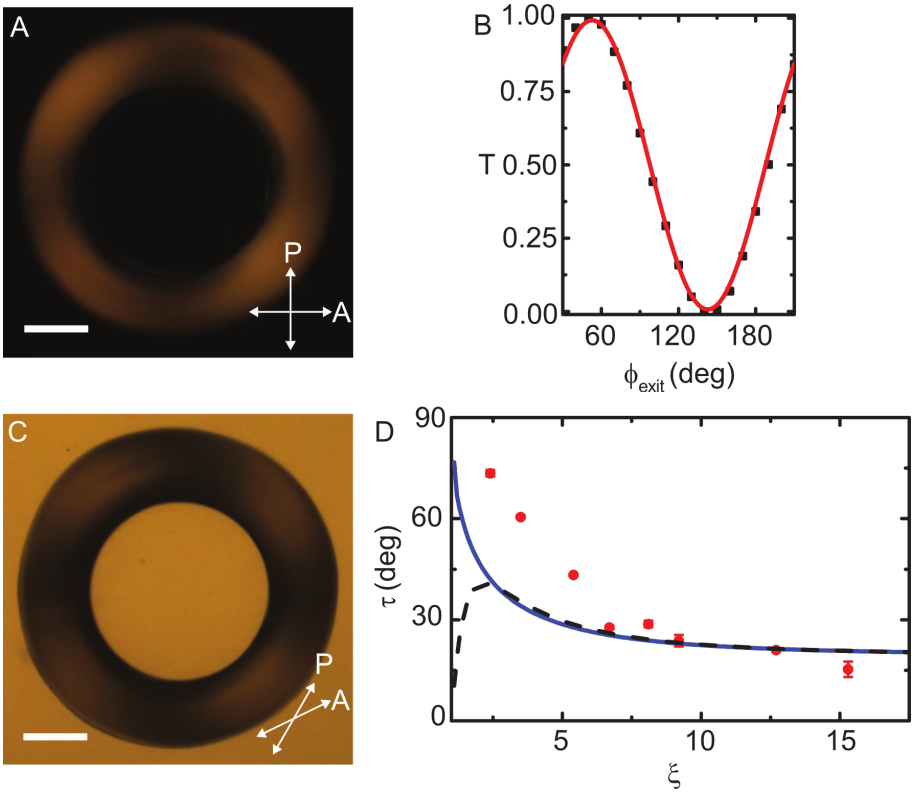

Figure 1.9: Determination of the twist angle and its dependence with slenderness. (A) A torus with $\xi = 3.5$ when viewed from the top and between cross-polarizers. (B) Transmission, T, as a function of the angle between the incident polarization direction and the analyzer, ϕ_{exit}. The line is a fit to the theoretical expectation in the Mauguin limit [89] with the twist angle, τ, as the only free parameter. We obtain $\tau = (52.9 \pm 0.4)^{\circ}$. (C) Top view of the same torus at the minimum of the transmission curve. We measure T along the four black regions that are observed, which are darkest for the indicated direction of the polarizer and analyzer. The sense of rotation of the analyzer indicates the nematic arrangement is right-handed; this likely results from the way the torus is generated, as all tori generated in the same way have the same handedness. (D) Twist angle as a function of ξ. The dashed line represents the theoretical prediction based on eq. (1.23), for $K_{24} = 1.02K_2$. The solid line represents the theoretical prediction based on the improved ansatz including the second variational parameter γ for the same value of K_{24}, where we have used the values $K_1 = 0.64K_3$ for 5CB [119]. (Scale bar: 200μm.) [55]

detailed measurements of the dependence of the twist angle on the elastic moduli were carried out by changing temperature which in turn affects the elastic moduli. The measured exponent β was 0.75 ± 0.1 for 8CB♠ and 0.76 ± 0.1 for 8OCB♡ [157], rather than the $\frac{1}{2}$ exponent we calculated in our mean field energy minimizations that entirely neglect thermal fluctuations.

♠8CB is short for 4'-n-octyl-4-cyano-biphenyl.
♡8OCB is short for 4-cyano-4'-octyloxybiphenyl.

Chapter 2.

Topological chiral sound in active liquids

Polar active fluids are fluids formed by particles that propel themselves in a certain direction. The study of self propelled particles has been a popular subject of research for the last two decades. Early theoretical progress [33, 52, 69] has been accompanied by the engineering of soft materials made of self-propelled polymers, colloids, emulsions, and grains [11, 43, 56, 59, 76, 79, 84, 85], which exhibit novel nonequilibrium phenomena. Prominent examples include phase separation of repulsive spheres, giant number fluctuations away from criticality, and long-range orientational order in two-dimensional flocks [27, 110, 148].

On the other hand, the study of topological states has been a topic of intense study in the quantum domain. One of the most notable topological effect in the quantum realm is the so called quantum Hall effect which is an precursor of a class of topological insulators.

Schematically, the quantum Hall effect is found when a two-dimensional electron gas is put in the presence of a strong external magnetic field — breaking time-reversal-symmetry [82]. The magnetic field causes the electrons to form classical cyclotron orbits. At edges of the system, however, the electrons are interrupted in their orbit causing an edge current. Upon analysing this system, it turns out that the bulk of this system is insulating, as the system is band-gapped. At the edge, however, the system will conduct. This property can be linked to the existence of a topological invariant that makes it robust to various perturbations that do not change the topology. This robustness is often referred to as topological protection.

It turns out these topological states are not exclusive to the quantum domain but are thus also present in the classical domain [14, 25, 28, 49, 57, 95]. Recent studies have shown that interesting topological quantum electronic effect often translate to similarly interesting topological acoustic effects [16, 18, 19, 34]. Here, we will combine topological mechanics and active matter to find topological insulating states. As active matter naturally breaks time-reversal-symmetry, it is an excellent candidate to achieve a self-assembled analogue of a certain class of topological insulators.

2.1 Classical quantum Hall fluids

Liquids composed of self-propelled particles have been experimentally realized using molecular, colloidal, or macroscopic constituents [8, 39, 43, 79, 85]. These active liquids can flow spontaneously even in the absence of an external drive [52, 69, 110]. Unlike spontaneous active flow [7, 9], the propagation of density waves in confined active liquids is not well explored. Here, we exploit a mapping between density waves on top of a chiral flow and electrons in a synthetic gauge field [14, 31] to lay out design principles for artificial structures termed topological active metamaterials. We design metamaterials that break time-reversal symmetry using lattices composed of annular channels filled with a spontaneously flowing active liquid. Such active metamaterials support topologically protected sound modes that propagate unidirectionally, without backscattering, along either sample edges or domain walls and despite overdamped particle dynamics. Our work illustrates how parity-symmetry breaking in metamaterial structure combined with microscopic irreversibility of active matter leads to novel functionalities that cannot be achieved using only passive materials.

We design active metamaterials with transport properties akin to those of quantum Hall fluids [82] by confining active liquids in periodic geometries that generate gapped density-wave spectra. Recent studies of topological acoustics have revealed that spectral bands characterized by topological invariants host (in their spectral gaps) robust mechanical states [18, 34, 49] and sound modes that propagate unidirectionally along sample edges and interfaces [4, 13, 14, 16, 25, 28, 31, 95]. However, the translation of topological-acoustic designs from macroscopic prototypes to soft materials has so far proven challenging, because overdamped particle dynamics overcome inertia and suppress the propagation of ordinary sound waves at the microscale. To address this challenge, we

elucidate the relationship between emergent active flow and the spectrum of topological density waves in a confined liquid composed of self-propelled particles that have overdamped dynamics and align their velocities, i.e., a confined polar active liquid.

In order to obtain generic results, we use a continuum mechanics description of polar active flow. The analog of Navier–Stokes equations that describe a one-component fluid of self-propelled particles (with overdamped particle dynamics, see section 2.2.3) are the Toner–Tu equations [52, 110, 148], which in their simplest form read

$$\partial_t \varrho + v_0 \boldsymbol{\nabla} \cdot (\varrho \mathbf{p}) = D_\rho \nabla^2 \varrho, \tag{2.1}$$

$$\partial_t \mathbf{p} + \lambda v_0 (\mathbf{p} \cdot \boldsymbol{\nabla}) \mathbf{p} = \left(\beta |\mathbf{p}|^2 - \alpha\right) \mathbf{p} - \frac{v_1}{\varrho_0} \boldsymbol{\nabla} \varrho + \nu \Delta \mathbf{p}, \tag{2.2}$$

where $\varrho(\mathbf{r}, t)$ is the density of active particles that fluctuates around its mean value ϱ_0. The polarization field of the material, $\mathbf{p}(\mathbf{r}, t)$, denotes the local average orientation of the velocities of the self-propelled units which, when isolated, all move at the same speed v_0. The effective viscosity, ν, the diffusivity, D_ρ, and the other (positive) hydrodynamic coefficients λ, v_1, α, and β have been computed from a number of microscopic models in Suzuki et al. [26], Bricard et al. [43], Solon et al. [61], Farrell et al. [65], and Bertin et al. [102]; α and β are the Landau coefficients used to model the spontaneous breaking of rotational symmetry; v_1 relates pressure and density. In section 2.3, we provide a concise introduction to the Toner–Tu model and explain how the left hand side of eq. (2.2) originates from overdamped dynamics of $\mathbf{p}$ and not from momentum conservation.

Numerically solving eq. (2.1) and eq. (2.2) in the connected-annuli geometry of fig. 2.1 a, we find the emergence of a uniform steady chiral flow in each annulus. As this flow is a consequence of spontaneous symmetry breaking, left-handed and right-handed orientations are equally likely to occur. These general continuum-mechanics results are confirmed by particle-velocity maps measured from a prototypical microscopic model shown in fig. 2.1 b, see section 2.2.3. As particle velocities align in the region shared between two adjacent annuli, the fluid within these annuli circulates in opposite directions, in analogy with either engaged counter-rotating gears or antiferromagnetic spins. Similar behavior was observed in bacterial fluids experiments [7] and simulations of agent-based models [20].

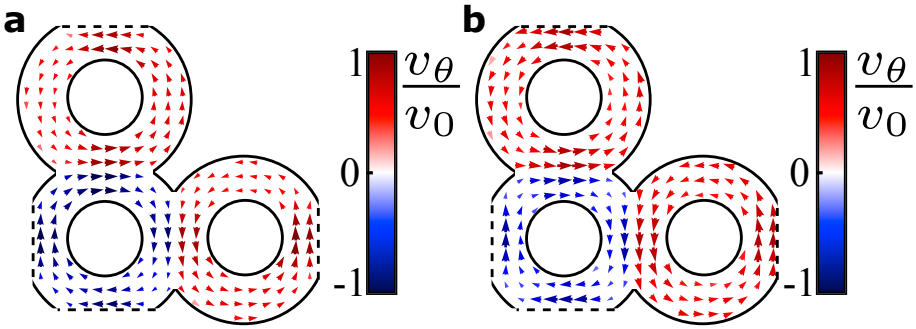

Figure 2.1: Steady states of polar active liquids in coupled annular channels. (a) Steady state of a polar active liquid described by the hydrodynamic eqs. (2.1) and (2.2), in a confinement geometry based on the Lieb lattice. Note that the inter-annular coupling leads to a stable steady-state order reminiscent of either engaged gears or spins in an antiferromagnet. The colors indicate the azimuthal component v_θ of the velocity field (also shown in arrows) around the center of the corresponding annulus. (b) Steady state of the same liquid simulated using a particle-based model that is described in section 2.2.3. (Dashed lines indicate periodic boundary conditions.)

When a homogeneous polar liquid flows through interconnected annuli, the channel geometry determines the mean polarization $\mathbf{p}_0(\mathbf{r})$, which is proportional to the steady-state velocity field. We now elucidate how this emergent spontaneous flow impacts sound propagation. We linearize eq. (2.1) and eq. (2.2) deep in the polar liquid phase, in which case both α and β are only weakly dependent on ρ. We define $\boldsymbol{\pi}(\mathbf{r},t) = \mathbf{p}(\mathbf{r},t) - \mathbf{p}_0(\mathbf{r})$ and $\rho(\mathbf{r},t) = \varrho(\mathbf{r},t) - \varrho_0$, and confirm that density waves propagate over a finite range of wave numbers q: $|\alpha|/c \ll q \ll c/(\nu + D_0)$, where $c \equiv \sqrt{v_0 v_1}$ sets the magnitude of the speed of sound, see [52, 110] and section 2.4. In this regime, density fluctuations obey a wave equation that depends on $\mathbf{p}_0$:

$$[\partial_t + \lambda v_0(\mathbf{p}_0 \cdot \nabla)][\partial_t + v_0(\mathbf{p}_0 \cdot \nabla)]\rho = c^2\nabla^2\rho. \tag{2.3}$$

Whereas (acoustic) density waves in simple driven fluids [14, 31] arise only in systems with inertial dynamics, such waves in polar active liquids survive even in the overdamped limit — in the latter case, these waves originate from Goldstone modes associated with broken rotational symmetry, see [110] and section 2.4. Figure 2.2 a shows the dispersion relation of density waves for a homogeneous polar liquid uniformly flowing along the x-direction ($\mathbf{p}_0(\mathbf{r}) = p_0\hat{x}$). Note that the speed of sound depends on the orientation of the wavevector $\mathbf{q}$ relative to $\mathbf{p}_0$, because Galilean invariance is broken in eq. (2.2).

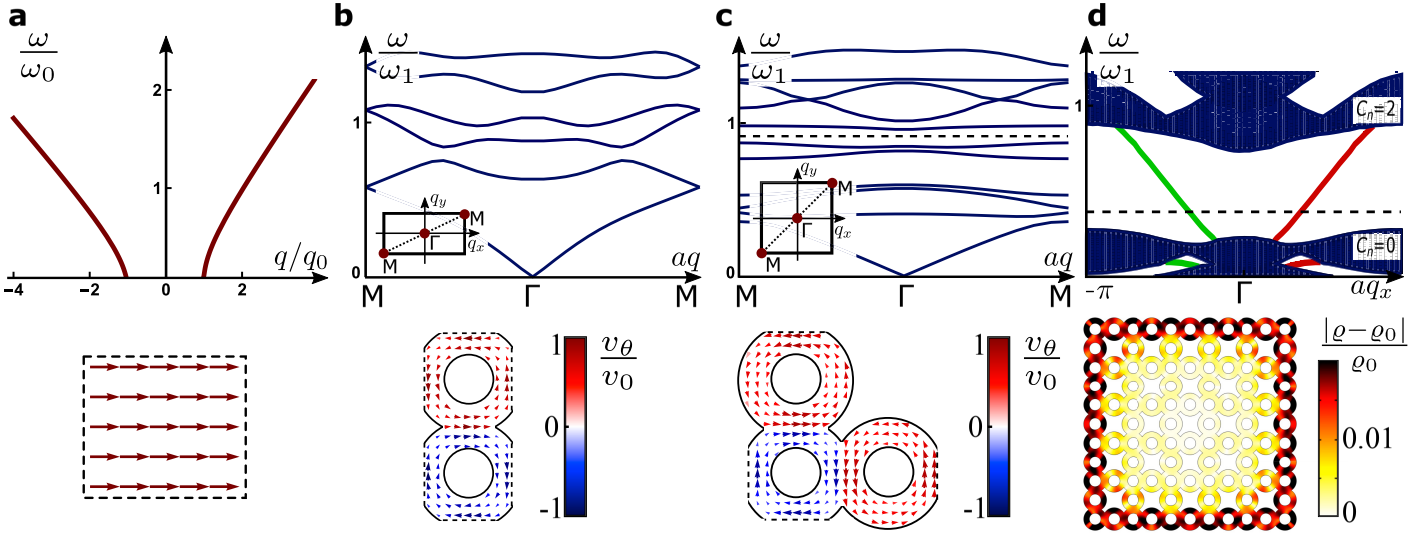

Figure 2.2: Dispersion of density waves in active metamaterials either with or without topological edge states. (a) Dispersion of longitudinal density waves in an active liquid with a uniform steady-state flow. For wavenumbers $|q| \gg q_0 \equiv \alpha/c$, these waves have a linear dispersion, reminiscent of pressure waves in a simple fluid. The spectrum is asymmetric due to the breaking of Galilean invariance by $\mathbf{p}_0$ (bottom row, a-c: corresponding steady-state flow). (b) Dispersion of density waves described by eq. (2.3) in the square-lattice geometry. Because the system retains time-reversal symmetry (TRS), bands cross at the point M in the Brillouin zone and the bands' Chern numbers are not well defined. (c) Dispersion of these density waves in the Lieb-lattice geometry. Due to broken TRS, the bands generically do not cross. (d) Zoom-in of the dispersion of these waves in a quasi-one-dimensional waveguide based on the Lieb lattice, with free edges on the top and bottom (also see fig. 2.3 d). The bulk modes (blue) correspond to the bands in (c). In addition, we observe chiral topological edge states plotted in red and green colors which indicate state chirality (defined by group velocity $d\omega/dq$) and, correspondingly, the edge on which these modes are located. These states inhabit gaps between bands with well-defined Chern number $C_n \neq 0$. (below: A density-wave eigenmode of a finite Lieb-lattice sample with frequency in this band gap. The frequency value is indicated by the dashed lines in c-d.)

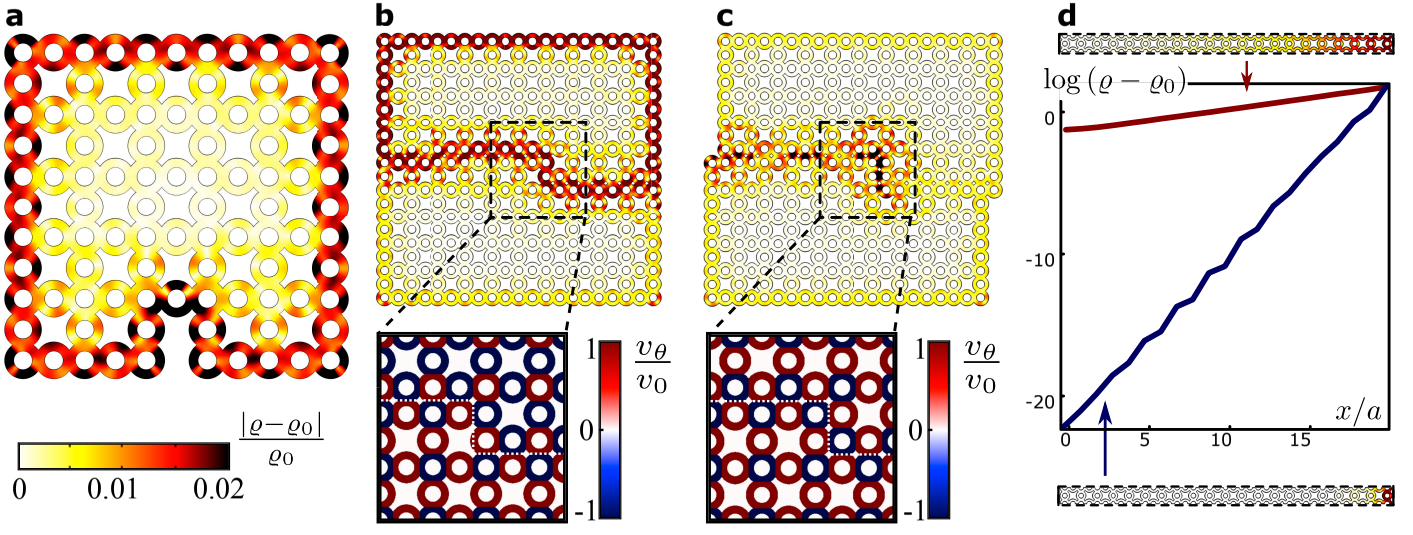

Figure 2.3: Topologically protected waveguides composed of an active metamaterial. (a) The chiral edge state in fig. 2.2 d is robust against defects along the edge: the state goes around a defect instead of backscattering. (b) This robustness extends to domain walls separating two different topological phases, constructed by taking advantage of antiferromagnetic interannular coupling and deleting a row of the Lieb lattice. Note that the edge state follows the domain wall, no matter the wall's shape. (c) By contrast, along a domain wall that doesn't separate different topological phases, the edge states are not robust to backscattering. They can scatter off kinks in the wall shape, in the middle of the sample. (bottom row, b–c: zoom-ins of the steady-states.) (d) Profile of the density within edge states shows that the state decays exponentially into the bulk. These exponentially localized edge states are characterized by their penetration depth, which can be controlled by changing the flow speed (top: $p_0 = 0.42$, bottom: $p_0 = 0.5$).

Our design of topological metamaterials exploits (i) microscopic irreversibility induced by activity and (ii) parity-symmetry breaking of the structure. To highlight how the interplay between activity and structural design leads to metamaterials that globally break time reversal symmetry, we contrast two simple geometries of interconnected channels: one based on the square lattice, fig. 2.2 b, and one based on the Lieb lattice, fig. 2.2 c. Solving eq. (2.3) numerically in a square lattice geometry (see section 2.2.2), we show that the wave spectrum contains degeneracies at the edge of the Brillouin zone where two spectral branches intersect (point M). Note that the corresponding steady-state flow is invariant with respect to simultaneously inverting the arrow of time and performing a lattice translation. By contrast, the degeneracy at point M is lifted for the Lieb lattice and a gap opens. Unlike the square lattice, the Lieb lattice has an odd number of rings per unit cell and, therefore, a net circulation of steady-state flow. Heuristically, the spectral-gap opening stems from the frequency difference between density waves propagating along versus opposite to flow with a non-vanishing net circulation. As a result, a gap opens only for unit cells that are chiral. In the limit $v_0 p_0/c \ll 1$, we rewrite eq. (2.3) as

$$\left[(\nabla - i\mathbf{A})^2 + \omega^2/c^2\right] \rho = 0, \tag{2.4}$$

where $\mathbf{A} \equiv \omega(\lambda+1) v_0 \mathbf{p}_0/(2c^2)$, and note that the steady-state velocity field $v_0\mathbf{p}_0$ couples minimally to the wavenumber of the density wave [31]. The emergent chiral flow plays the role of a synthetic gauge field for a charged quantum particle, whereas its curl, the vorticity, acts analogously to a magnetic field that lifts spectral degeneracies.

We establish the topological nature of the band structure corresponding to eq. (2.3) in the Lieb lattice by calculating (for each band) an integer-valued topological invariant called the Chern number, C_n, see section 2.2.1 and Hasan et al. [82] for an introduction. For almost all of the bands in the spectrum, and for a wide range of values of the mean polarization p_0, we find that $C_n \neq 0$, fig. 2.2 c-d. As C_n is an integer, it cannot vary smoothly from within the sample to the exterior (where $C_n = 0$). Therefore, C_n can only change if the band gap closes along the sample edge, locally enabling edge-mode propagation [82]. Such edge modes, shown in fig. 2.2 d, are called *topologically protected* because they arise from the presence of topological invariants in the bulk, irrespectively of the sample's shape or disorder. As in quantum Hall fluids, the topological edge modes are chiral, i.e., they propagates along a single direction. The chirality of the edge modes reflects the chirality of the flow within the unit

cell. The system edge acts as a robust acoustic diode — topological density waves, unlike ordinary waves, propagate unidirectionally along the boundary and do not backscatter even if obstacles or sharp corners are introduced, as demonstrated in fig. 2.3 a.

Similarly, along the boundary between two regions of distinct flow chirality, C_n varies from one integer value to another. Therefore, in this region of space, the band gap must vanish, which leads to the existence of topologically protected waves along this interface. A topological waveguide can be sculpted in the bulk by deleting a row of annuli, as in fig. 2.3 b. For this sample, topologically robust density waves propagate through the irregularly shaped domain wall in the bulk of the metamaterial. However, if the domain wall has both a row deletion *and* a half-column displacement, then the chirality of flow does not change across the wall. Consequently, modes associated with the domain wall are not topologically protected and do backscatter in the bulk, as exemplified in fig. 2.3 c.

Whereas the existence of edge waves in polar active liquids is topologically protected, their penetration depth into the bulk can be tuned by changing the flow speed. As shown in the section 2.6, by considering the minimal coupling form of eq. (2.4) relevant to the motion of density waves in the limit $v_0 p_0/c \ll 1$, we expect the penetration to be exponential with a penetration depth ℓ scaling as $\ell \sim |\mathbf{A}|^{-1} \sim ac/(v_0 p_0)$, where a is the lattice spacing. We stress that this spatial structure differs from the Gaussian profiles of quantum Hall states that share similar topological properties. These predictions are in good agreement with the numerical resolution of the full equations of motion: as shown in fig. 2.3 d, the penetration of the edge modes is exponential and decreases with the mean-flow speed.

Having explored the phenomenology of chiral states in confined active liquids, we can now compare this realization of a topological metamaterial with those achieved in driven liquids [14, 31]. First, in both cases, to achieve a small penetration depth it is necessary that the speed of flow be appreciable relative to the speed of sound. For a simple fluid, this is a limitation — driving the fluid at speeds near the speed of sound leads to flow instabilities either in the bulk or in the boundary layer of the fluid. By contrast, for active liquids, the speed of flow $v_0 p_0$ and the speed of sound c are distinct parameters entering the hydrodynamic eq. (2.2) and may, in general, be comparable, so that the chiral edge state may be readily observable. Second, whereas metamaterials composed of driven fluids require motors at each component to provide the drive, for an active liquid the drive is provided by the particles composing the liquid, whereas the confining channels prescribe the emergent chiral

flow. Third, topological density waves in polar active liquids originate from Goldstone modes due to broken rotational symmetry. As a consequence, they can propagate even if particle dynamics are overdamped — paving the way towards colloidal and other soft matter realizations of mechanical topological insulators.

We examined topological sound in metamaterials based on polar active liquids, but our approach can be applied to wave propagation in other time-reversal-symmetry-broken active systems. Our results epitomize the defining feature of topological active metamaterials: they combine the microscopic irreversibility inherent in active matter with structural design to achieve functionalities absent in passive materials.

2.2 Methods

2.2.1 Chern numbers

We establish the topological nature of the active-liquid metamaterial by calculating (for the Lieb-lattice spectrum) an integer-valued topological invariant called the *Chern* number associated with each band, see [82]. The Chern number C_n is analogous to the Euler characteristic of a closed surface with Gaussian curvature. Using the Gauss-Bonnet theorem, we can compute C_n by integrating a curvature called the *Berry curvature* $B_n(\mathbf{q})$ over a closed surface formed by the first Brillouin zone (which by construction is periodic in both directions):

$$C_n \equiv \frac{1}{2\pi}\int_{\mathrm{BZ}} B_n(\mathbf{q})d\mathbf{q}, \tag{2.5}$$

where $B_n(\mathbf{q}) \equiv \nabla\times\mathcal{A}_n(\mathbf{q})$, $\mathcal{A}_n(\mathbf{q}) \equiv i(\mathbf{u}^n_\mathbf{q})^\dagger\cdot(\nabla_\mathbf{q}\mathbf{u}^n_\mathbf{q})$ is the Berry connection calculated from the $\mathbf{u}^n_\mathbf{q}$ eigenstate of band n and wavenumber $\mathbf{q}$. For our discrete data set, we use the gauge-choice-independent protocol described in Fukui et al. [46] to efficiently calculate the Chern number using a coarse discretization of the first Brillioun zone.

2.2.2 Finite element simulations

We solve eq. (2.3) for both a finite geometry and for a unit cell with Floquet boundary conditions (i.e., periodic boundary conditions with an additional phase factor) using COMSOL Multiphysics finite element analysis simulations on a highly refined mesh. To obtain the dispersion relations shown in fig. 2.2 b–

c, we perform a sweep through the wavenumbers (q_x, q_y) along the $M\Gamma M$ cut and assign the appropriate phase factors for (Floquet) boundary conditions across the unit cell. Then, we solve the corresponding eigenvalue problem at each wavenumber and plot the corresponding bands. We numerically obtain the solutions in the form of frequencies $\omega_n(\mathbf{q})$ as well as the density eigenstates $\tilde{\varrho}(\omega, \mathbf{q})$, for which the density waves are $\varrho(x,t) = \tilde{\varrho}(\omega, \mathbf{q})e^{i(\omega t - \mathbf{q}\cdot\mathbf{x})}$. Unless otherwise noted, to obtain good numerical accuracy, we use for the corresponding background flow a simplified model with constant $|\mathbf{v}| = p_0 v_0 = 0.5c$, pointed along the azimuthal direction of the corresponding annulus (see visualizations in insets of fig. 2.3 b–c). In the regions of annular overlap, we patch the flow field using an interpolation that is linear along the x-direction, and then normalize the result. For fig. 2.2 d, we begin with a quasi-one-dimensional lattice geometry (also see fig. 2.3 d), and impose a phase factor only along the periodic boundaries in the x-direction. Again, the eigenvalues are plotted, and those forming a solid region corresponding to the bulk bands are shaded in blue. For parts of fig. 2.2 d and fig. 2.3 a–c, we use a finite geometry and plot a single eigenmode located in the band gap that contains topological states.

2.2.3 Particle-based model

We used a particle-based model as an illustrative example to check the steady-state flow that we obtained from the Toner–Tu equations. We emphasize that the conclusions obtained in the section 2.1 are based on the continuum Toner–Tu equations, which form a description that has a more general applicability than the specific particle-based model presented below. We choose a continuous-time model that includes Vicsek-like alignment interactions and repulsive interactions that prevent clustering [128, 149]. The position $\mathbf{x}_i$ and velocity $\mathbf{v}_i$ of the i^{th} particle is evolved using a symplectic Euler integrator♠ for Newton's laws of motion with the force term

$$\begin{aligned}\mathbf{F}_i = m\dot{\mathbf{v}}_i = &-\gamma\mathbf{v}_i + F_0\left(\hat{\mathbf{v}}_i + \sum_{\langle \mathbf{x}_i, \mathbf{x}_j\rangle}\hat{\mathbf{v}}_j/N\right)\\ &+\sum_{k}^{N}\nabla_i U(|\mathbf{x}_i - \mathbf{x}_k|) + \sqrt{2\gamma k_B T}\,\hat{\boldsymbol{\zeta}}_i(t),\end{aligned} \tag{2.6}$$

♠The symplectic Euler integration scheme is described in appendix K.

where γ is a friction coefficient, m is the particle mass, and F_0 is the active force such that $v_0 = F_0/\gamma$. The neighbors in the F_0 term are denoted as $\langle \mathbf{x}_i, \mathbf{x}_j \rangle$ and include all particles $\mathbf{x}_j$ within a distance R ($= a/20$) of $\mathbf{x}_i$, see fig. 2.4. We use a Yukawa potential $U(r)$:

$$U(r) = \frac{b}{re^{\kappa r}} \tag{2.7}$$

to account for excluded-volume effects, where $\kappa^{-1} = R/6$ sets the repulsion range, and $b = 4 \times 10^3 F_0/\kappa^2$ sets the Yukawa coupling constant. The white-noise stochastic forcing term $\hat{\boldsymbol{\zeta}}_i(t)$, where $\left\langle \hat{\boldsymbol{\zeta}}_i(t)\hat{\boldsymbol{\zeta}}_i(t') \right\rangle = \delta(t-t')$, mimics thermal fluctuations. The temperature is set by $k_B T = 10^{-3} b\kappa = 2 \times 10^{-2} m v_0^2$. The nonlinear forcing term $F_0\hat{\mathbf{v}}$, where $\hat{\mathbf{v}} \equiv \mathbf{v}/|\mathbf{v}|$, breaks the equilibrium fluctuation-dissipation relation for this far-from-equilibrium system. The overdamped limit is defined as the regime for which the velocity relaxation time $\tau_\mathrm{p} \equiv m/\gamma$ is much smaller that the characteristic oscillation time τ_o associated with the interaction potential: $\tau_o \equiv \sqrt{mb^{-1}\rho^{-3}}$, where ρ is the particle density. Time integration is done using the following time step $\Delta t = 10^{-5} m/\gamma$, where m is the mass of an individual particle.

Both the square and Lieb lattices have lattice spacing $a = 120\kappa^{-1}$ and are implemented by confining particles in overlapping annuli.♠ A single annulus has an inner radius $R_\mathrm{in} = \frac{3}{10}a$ and $R_\mathrm{out} = 2R_\mathrm{in}$. The confining boundaries are implemented using a steep one-sided harmonic repulsive potential $\frac{1}{2}k_w x^2$ with $k_w = 3.14 \times 10^5 \gamma^2/m$ experienced by all particles. The area fraction of particles is

$$\phi = \frac{NR^2}{R_\mathrm{out}^2 - R_\mathrm{in}^2} \approx 6.17, \tag{2.8}$$

where N is the number of particles per annulus. (We choose units in which $m = 1$, $a = 6$, and $a/v_0 = 60$.)

In the steady state, the flow for the k-th annulus is measured by the azimuthal component of the velocity field

$$v_\theta = \frac{1}{v_0}\left\langle \sum_{i=1}^{N} \mathbf{v}_i \cdot \hat{\theta}_k \right\rangle, \tag{2.9}$$

♠For a possilbe algorithm to generate square lattices and Lieb lattices respectively see appendix sections Q.1 and Q.4.

where $\hat{\theta}_k$ is the azimuthal unit vector around the annulus center, and $\langle \ldots \rangle$ denotes a time average over 8000 configuration, with 1000 timesteps between subsequent configurations. $v_\theta = \pm 1$ for an ideally flowing system; the sign indicates flow chirality. Two examples of steady states are plotted in fig. 2.5 and the dependence of v_θ on ϕ within the Lieb lattice is plotted in fig. 2.6. At low area fraction, the particles undergo the alignment transition for their velocities, whereas at high area fraction they jam. The flowing steady state occurs over a wide range of intermediate area fractions.

2.3 Toner–Tu hydrodynamics of polar active liquids

The hydrodynamic equations of a *passive* polar liquid take into account three slow variables: the usual density, $\rho(\mathbf{r}, t)$, and velocity, $\mathbf{v}(\mathbf{r}, t)$ fields, as well as a broken-symmetry field, the polarization $\mathbf{p}(\mathbf{r})$, defined as the local average of the particle orientations. When the polar units that form the liquid propel themselves on a solid surface, momentum is no longer conserved, because the substrate acts as a momentum sink. Such systems are referred to as *dry active matter*, even though the particles may propel in a fluid medium as in, e.g., Bricard et al. [43] and Schaller et al. [85]. The substrate enables preferential alignment of the particles' velocities with their polar orientation. The hydrodynamic equations of the resulting polar *active* liquid read

$$\partial_t \varrho + \nabla_i(\varrho v_i) = D^\rho \nabla^2 \rho, \tag{2.10}$$

$$\partial_t(\varrho v_j) + \nabla_i\left(\varrho v_i v_j\right) = \nabla_i \sigma_{ij} - \Gamma^v(v_j - v_0 p_j), \tag{2.11}$$

$$\partial_t p_j + v_i \nabla_i p_j + \omega_{ji} p_i = \nu_1 v_j + \nu_2 v_{ji} p_i - \Gamma^p \frac{\delta \mathcal{H}}{\delta p_j}, \tag{2.12}$$

where we have introduced the symmetric part of the strain-rate tensor $v_{ji} \equiv \frac{1}{2}\left(\partial_j v_i + \partial_i v_j\right)$ and the vorticity tensor $\omega_{ji} \equiv \frac{1}{2}\left(\partial_j v_i - \partial_i v_j\right)$. Note that the components of the velocity vector v_i for this one-fluid model are the coarse-grained velocities of the self-propelled particles composing the active liquid and *not* of the potential surrounding fluid (e.g., air or solvent). The first (continuity) equation reflects mass conservation and includes a diffusive term $D^\rho \nabla^2 \rho$. The second equation includes the liquid stress tensor σ as well as an active frictional term proportional to Γ^v. This terms differentiates eq. (2.11) from the usual Navier–Stokes equations as it explicitly breaks momentum conservation. For the sake of simplicity, we consider here a linear coupling between the velocity and the polarization (the hydrodynamic coefficient v_0 has the dimensions of a speed and scales with the speed of an isolated active particle). Equation (2.12)

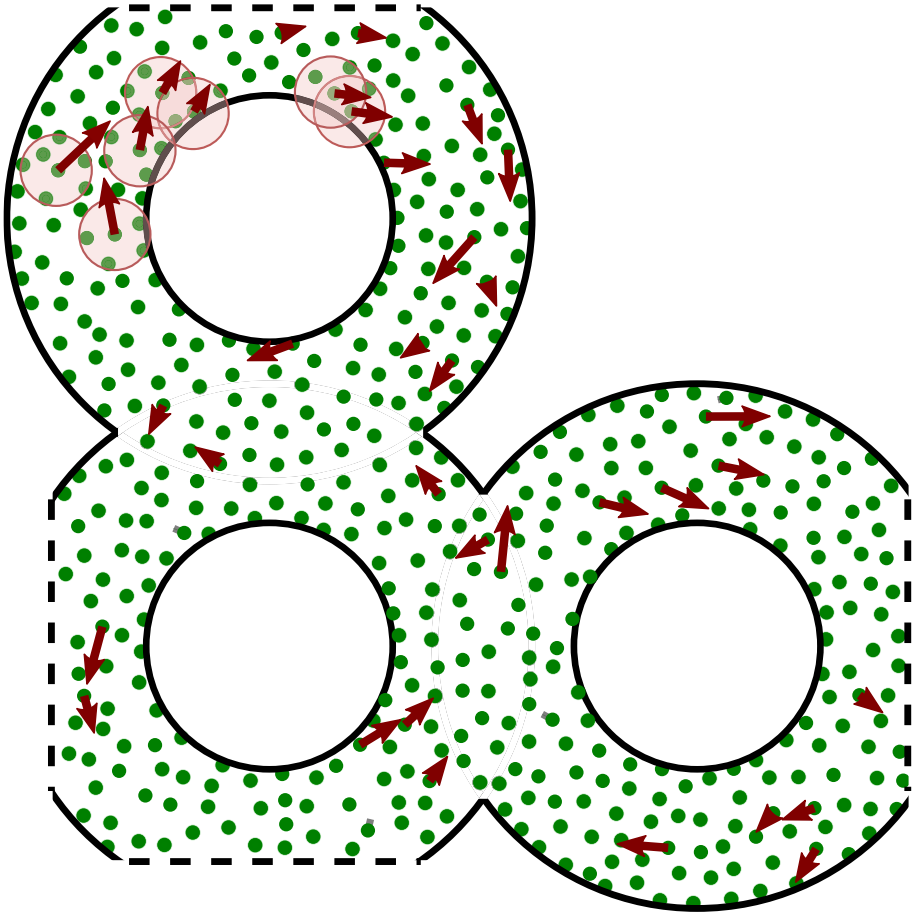

Figure 2.4: One configuration of the particle-based simulation in a periodic geometry based on the Lieb lattice. For each particle, the radius of the short-range repulsive interaction is indicated in green. For a few chosen particles, the radius of the longer-range alignment interaction is indicated in pink. For some particle, their instantaneous velocity is indicated by a red arrow.

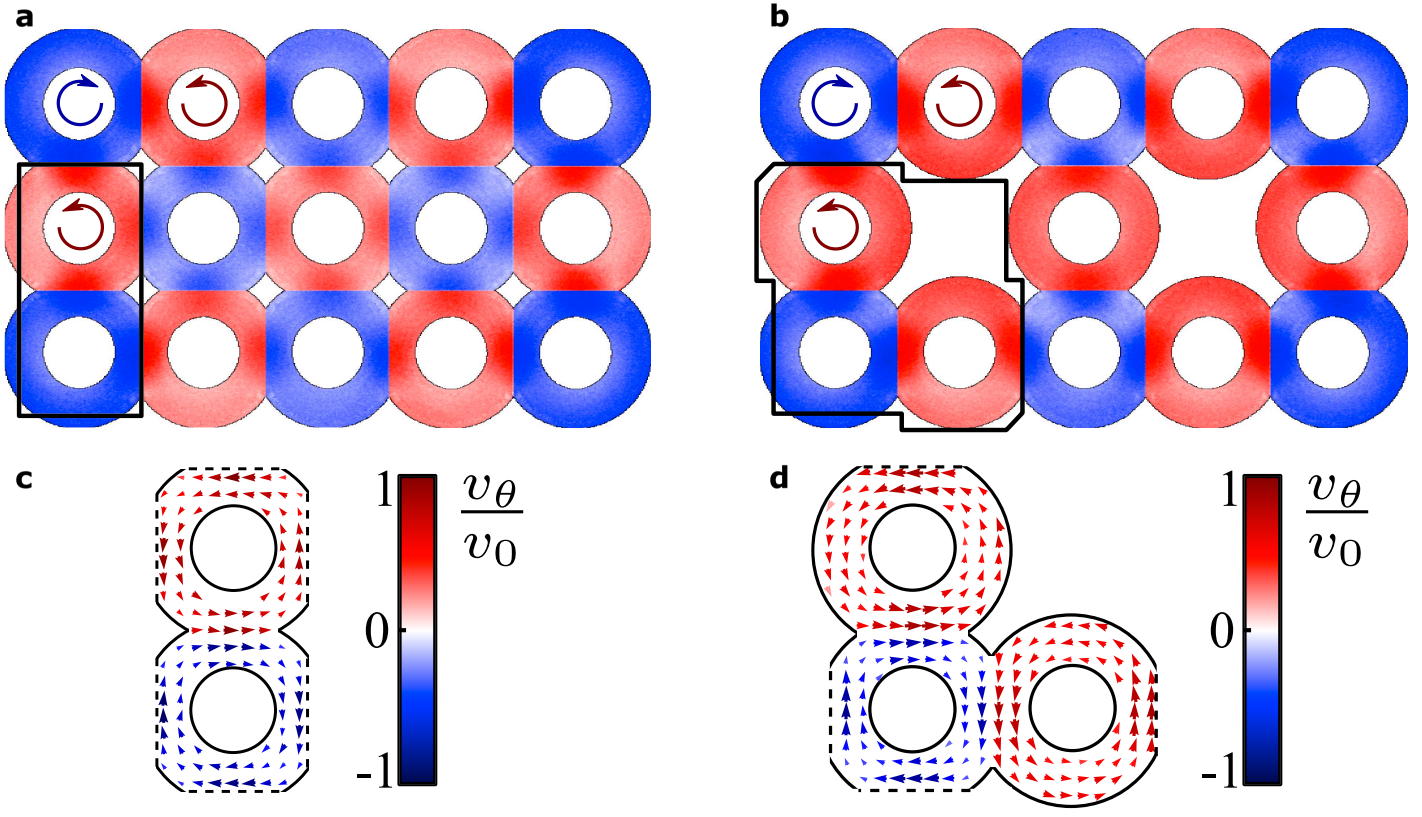

Figure 2.5: The steady state for the flow of a polar active liquid in active metamaterials for (a,c) square lattice and (b,d) topological Lieb lattice, all obtained from molecular dynamics (MD) simulations. For both geometries we also reproduce parts of fig. 2.2, showing the spatially-dependent flow within a single unit cell (c,d), with the color scale for the azimuthal component of the flow field.

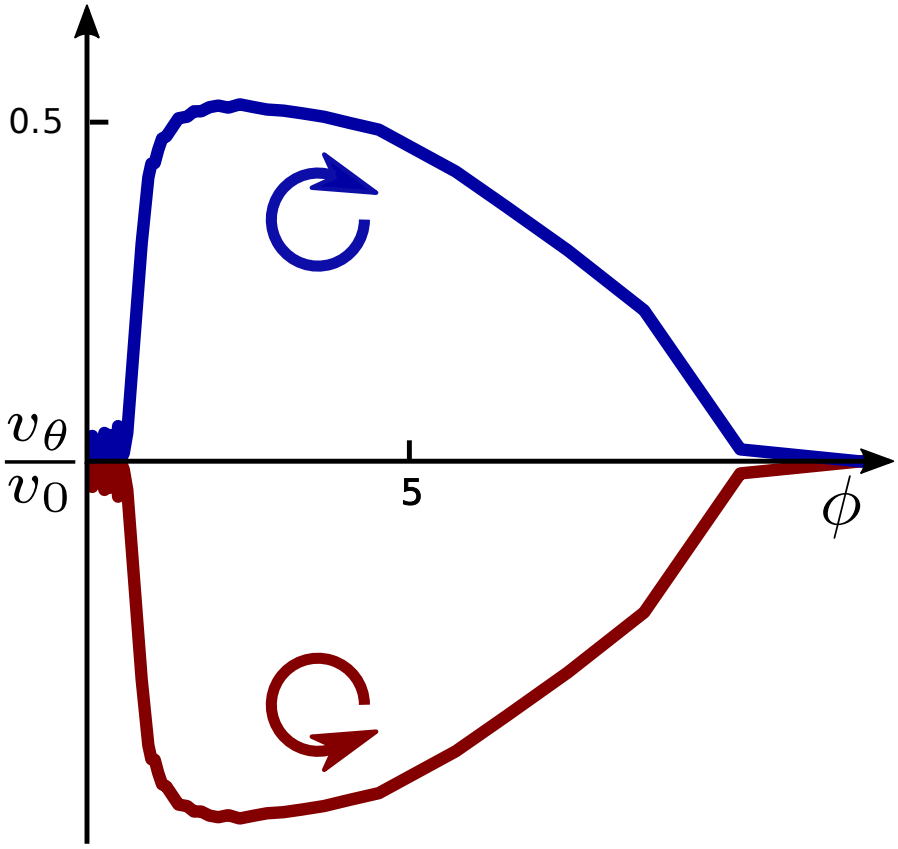

Figure 2.6: (a) The average normalized azimuthal component v_θ/v_0 (measured relative to the center of each annulus) as a function of particle density ϕ in the Lieb lattice geometry measured relative to the (large) radius of the alignment interaction (see section 2.2.3, fig. 2.4).

describes the relaxational dynamics of the polarization, see [52]. The left-hand side of eq. (2.12) contains the comoving (2nd term), corotational (3rd term) time-derivative of the polarization. The right-hand side of eq. (2.12) includes the effective Hamiltonian $\mathcal{H}$ and the dissipative coefficient Γ^p along with two frictional terms. The first frictional term in eq. (2.12) contains the friction coefficient ν_1 and describes the friction between particle and substrate — this terms is responsible for the "weathercock effect" i.e., the polar particles' local alignment with the flow see, e.g., Kumar et al. [39] and Brotto et al. [44]. The second friction term in eq. (2.12) contains the friction coefficient ν_2 and originates from the friction between an individual polar particle and the surrounding active fluid (itself composed of polar particles). The sign and the magnitude of ν_2 controls the strength of alignment of the particle polarization with the local elongation (or compression) axis of the flow.

We can also consider eqs. (2.10) to (2.12) in the limit for which the frictional Γ^v term dominates eq. (2.11). In this overdamped limit, eq. (2.11) reduces to a constraint equation, $\mathbf{v} = v_0\mathbf{p}$, and the hydrodynamics is fully captured by mass conservation and the dissipative dynamics of the polarization field. A gradient expansion of $\mathcal{H}$ then yields [110, 148]:

$$\partial_t \varrho + v_0 \boldsymbol{\nabla} \cdot (\varrho \mathbf{p}) = D_0 \nabla^2 \varrho, \tag{2.13}$$

$$\begin{aligned} \partial_t \mathbf{p} + \lambda v_0 \mathbf{p} \cdot \boldsymbol{\nabla} \mathbf{p} = \left(\beta |\mathbf{p}|^2 - \alpha\right) \mathbf{p} - \frac{v_1}{\varrho_0} \boldsymbol{\nabla} \varrho + \nu \Delta \mathbf{p} \\ + \lambda_2 v_0 \nabla |\mathbf{p}|^2 - \lambda_2 v_0 \mathbf{p} (\nabla \cdot \mathbf{p}), \end{aligned} \tag{2.14}$$

where all of the hydrodynamic coefficients depend *a priori* on the local density. Note that whereas for a system with Galilean invariance, $\lambda = 1$ and $\lambda_2 = 0$, for the polar active liquid, which lacks this symmetry, these parameters may be arbitrary. Studies of realistic microscopic models have found λ to be positive, less than, and of order 1, and for the numerical computations performed in this work, we assume $\lambda = 0.8$ [43, 65, 102]. The lack of Galilean invariance as well as momentum conservation leads to the α and β terms in eq. (2.14), which suggests a preference for either zero or nonzero velocity — depending on the sign of α. In the article, for the sake of simplicity we focus on the case in which the λ_2 terms are negligible. In this case, eqs. (2.13) and (2.14) reduce to eqs. (2.1) and (2.2), and are reproduced here:

$$\partial_t \varrho + v_0 \boldsymbol{\nabla} \cdot (\varrho \mathbf{p}) = D_\rho \nabla^2 \varrho, \tag{2.15}$$

$$\partial_t \mathbf{p} + \lambda v_0 (\mathbf{p} \cdot \boldsymbol{\nabla}) \mathbf{p} = \left(\beta |\mathbf{p}|^2 - \alpha\right) \mathbf{p} - \frac{v_1}{\varrho_0} \boldsymbol{\nabla} \varrho + \nu \Delta \mathbf{p}. \tag{2.16}$$

Equations (2.15) and (2.16) are sufficient to capture the phenomena associated with linear density waves in a polar active liquid relevant to our analysis. In that limit, the polarization field itself defines the fluid velocity, so that the coupling between the polarization field and the density gradient has an effect analogous to that of a pressure gradient in an equilibrium liquid.

2.4 Linear density waves for Toner–Tu liquids

For the case $\alpha < 0$, the Toner–Tu equations result in a steady state of the fluid with spontaneous flow in the bulk, such that $p_0^2 \equiv |\mathbf{p}_0|^2 = -\alpha/\beta$. Although in the bulk, the spontaneous flow direction $\hat{\mathbf{p}}_0$ could be arbitrary, in physical realizations of active liquids, the boundaries fix $\hat{\mathbf{p}}_0$. For example, in an open channel, $\hat{\mathbf{p}}_0$ is parallel to the channel walls. In the Lieb lattice geometry, we have solved eqs. (2.15) and (2.16) for a sufficient time for the dynamics to relax to a steady state. We find that this steady state, plotted in fig. 2.1 a (also see fig. 2.5), has the features of the spatial profile observed from our particle-based simulations, although the particle-based simulations lead to a smoother profile, fig. 2.1 b.

In the analysis performed for the density wave computations, we take a particularly simple form of the steady state, based on the profile we observe. We postulate the polarization has magnitude unity everywhere and is oriented azimuthally, i.e., perpendicular to the vector connecting the position of the fluid to the nearest annulus center. In the regions of overlap between annuli, we linearly interpolate between the two annular flow profiles. This spatial profile is plotted in a large sample in fig. 2.1 a.

Thus, given a spontaneous steady-state flow field $\mathbf{p}_0$, we expand $\boldsymbol{\pi}(\mathbf{r}, t) = \mathbf{p}(\mathbf{r}, t) - \mathbf{p}_0(\mathbf{r})$ and $\rho(\mathbf{r}, t) = \varrho(\mathbf{r}, t) - \varrho_0$ to find

$$\partial_t \rho + (v_0 \mathbf{p}_0 \cdot \nabla)\rho = -v_0 \rho_0 \nabla \cdot \mathbf{v} + D_0 \nabla^2 \rho, \tag{2.17}$$

$$\partial_t \mathbf{v} + \lambda v_0 (\mathbf{p}_0 \cdot \nabla)\mathbf{v} = -(v_1/\rho_0)\nabla\rho + 2\alpha(\mathbf{v} \cdot \hat{\mathbf{p}}_0)\hat{\mathbf{p}}_0 + \nu \nabla^2 \mathbf{v}. \tag{2.18}$$

For the case of propagating waves, the right-hand side can be decomposed as the sum of a dominant anti-Hermitian matrix that governs wave dispersion and a perturbatively small Hermitian matrix that governs wave attenuation. As we are interested in the behavior of an active fluid deep in the ordered phase, we have assumed α to be constant. The ρ dependance of α, which leads to additional dissipative terms, would be most significant near the phase transition from an isotropic to a flowing steady state. There are two notable differences for the propagation of density waves in an active liquid compared

to a simple fluid: (1) the α term acts as an additional dissipative term for sound in an active liquid, and (2) one of the convection terms contains the coefficient λ ($\neq 1$). Due to this second difference, the equation of motion can no longer be "Galilean boosted" into a different reference frame by replacing the lab-frame derivative ∂_t by a convective derivative.

To closely examine the mode structure in eqs. (2.17) and (2.18), we split the vector $\mathbf{v}$ into components $v_\parallel$ and $v_\perp$, respectively parallel and perpendicular to $\hat{\mathbf{p}}_0$. Note that due to the confinement of the active liquid inside a channel, we can assume that the density waves only propagate along the channel and, therefore, the derivatives of $\mathbf{p}$ and ρ along the direction perpendicular to $\hat{\mathbf{p}}_0$ can be ignored. Under this assumption, eqs. (2.17) and (2.18) reduce to:

$$\partial_t \rho + v_0 p_0 \partial_\parallel \rho = -v_0 \rho_0 \partial_\parallel v_\parallel + D_0 \partial_\parallel^2 \rho, \tag{2.19}$$

$$\partial_t v_\parallel + \lambda p_0 \partial_\parallel v_\parallel = -(v_1/\rho_0)\partial_\parallel \rho + 2\alpha v_\parallel + \nu \partial_\parallel^2 v_\parallel, \tag{2.20}$$

$$\partial_t v_\perp + \lambda p_0 \partial_\parallel v_\perp = \nu \partial_\parallel^2 v_\perp. \tag{2.21}$$

Let us now consider eqs. (2.19) to (2.21) for the density and the longitudinal velocity modes in an active liquid. Ignoring, for now, the effects of the flow, we can calculate the dispersion relation for density waves in active liquids in the limit $q \ll c/(D_0 + \nu)$, where q is the wavenumber of the density wave and $c \equiv \sqrt{v_0 v_1}$ is the speed of sound. The frequency is then given by $\omega(q) = i|\alpha| + \sqrt{q^2 v_0 v_1 - \alpha^2} + i(D_0+\nu)q^2/2$ (also see fig. 2.2 a). Whereas the real component of ω governs the propagation of sound waves, the imaginary component governs their dissipation. Due to spontaneous flow, the sound wave frequency may, generically, have a real component, which is plotted in fig. 2.1 a. Furthermore, in the limits $q \gg |\alpha|/c$, the imaginary component will always be much smaller than the real component. Thus, in the regime $|\alpha|/c \ll q \ll c/(D_0 + \nu)$, there exist longitudinal density waves that propagate and decay slowly in the ordered active liquid. Provided we are in this regime, for phenomena on sufficiently short time scales, we may ignore the dissipative terms and concentrate on the wave-like solutions to the equations of motion.

2.5 Analogy with Schrödinger equation

Note that when the dissipative components of the density wave equation can be neglected, eq. (2.3) may be recast as a single wave equation. By applying the convective derivative $\partial_t + \lambda v_0(\mathbf{p}_0 \cdot \nabla)$ to the continuity equation, eq. (2.19), and then substituting the velocity equation of motion, eq. (2.20), one obtains:

$$[\partial_t + \lambda v_0(\mathbf{p}_0 \cdot \nabla)][\partial_t + v_0(\mathbf{p}_0 \cdot \nabla)]\rho = c^2\nabla^2\rho. \tag{2.22}$$

The eigenvalue problem for the above wave equation has solutions in terms of the frequency ω of a time-dependent oscillation $\rho(\mathbf{x}, t) = \tilde{\rho}(\mathbf{x}, \omega)e^{i\omega t}$. The corresponding equation has the form, provided that $M \equiv v_0 p_0/c \ll 1$,

$$\left[c^2\nabla^2 + \omega^2 - i\omega(\lambda + v_0)\mathbf{p}_0 \cdot \nabla\right]\tilde{\rho} = 0, \tag{2.23}$$

or,

$$\left[(\nabla - i\mathbf{A})^2 + \omega^2/c^2\right]\tilde{\rho} = 0, \tag{2.24}$$

where $\mathbf{A} \equiv \omega(\lambda + 1)v_0\mathbf{p}_0/(2c^2)$. This shows that the velocity field $v_0\mathbf{p}_0$ acts as an effective vector potential for the propagation of density waves.

2.6 Scaling argument for penetration depth

From the form of eq. (2.24), we can deduce the following scaling argument for the penetration depth of a topological edge state in the relevant limit $v_0 p_0/c \ll 1$. Consider the first term, $(\nabla - i\mathbf{A})^2$, which shows the minimal coupling between density gradients and spontaneous flow [31]. The penetration depth is a lengthscale that originates from density gradients and therefore scales as $\ell \sim \mathbf{A}^{-1}$. Furthermore, $\mathbf{A} \sim v_0 p_0 \omega/c^2$ and depends on a characteristic frequency $\omega \sim c/a$, where c is the speed of sound and a is a characteristic lengthscale of the material, i.e., the lattice spacing. In addition, $\mathbf{A}$ is approximately the same from one unit cell to the next. Combining these scaling relations, $\ell \sim ac/(v_0 p_0)$. The length ℓ diverges as the flow velocity goes to zero and, therefore, as the material loses its bulk bandgap.

We also note that we expect and observe topological edge states to be localized near the edge with an *exponential* profile, see fig. 2.3 d. To see why we expect eq. (2.24) to lead to exponentially localized states, note that if we assume $\rho \sim f(\mathbf{x}/\ell)$, and the scaling law derived above for ℓ, $\ell \sim ac/(v_0 p_0)$, eq. (2.24) predicts $f'' \sim f$, with a dimensionless proportionality constant.

An exponential profile satisfies this approximate scaling form. Such a profile is a consequence of the fact that $\mathbf{A}$ does not vary over lengthscales larger than a unit cell, an argument that relies on the metamaterial structure of the topological state. By contrast, in the quantum Hall fluid, the frequency scale depends on the field strength and $\mathbf{A}$ varies over large distances, which leads to both a Gaussian profile of states in a Landau level as well as a different scaling for the penetration depth [172].

2.7 Conclusion

We have shown how polar active fluids confined in a two-dimensional Lieb lattice form a time-asymmetric steady state. Upon analyzing the dispersion of density waves in this system we find it is gapped between bands with a well-defined Chern number. In these gaps we find chiral topological edge states, similar to quantum Hall effect, yet in the classical domain. In order to probe the robustness of these states, we show that these edge states remain in a system with defects or domain walls with systems of different topological phases. Additionally, we show how the edge states of these systems are exponentially localized, with a penetration depth controlled by the flow speed of the active fluid.

Chapter 3.

Chiral active liquids with self-rotation

The last two decades have seen significant progress in our understanding of active matter. Early theoretical progress [33, 52, 69] has been accompanied by the engineering of soft materials made of self-propelled polymers, colloids, emulsions, and grains [11, 43, 56, 59, 76, 79, 84, 85], which exhibit novel nonequilibrium phenomena. Prominent examples include phase separation of repulsive spheres, giant number fluctuations away from criticality, and long-range orientational order in two-dimensional flocks [27, 110, 148].

The systems mentioned above share the characteristic that constituents acquire translational momentum due to active propulsion, but rotate only in response to collisions or diffusion. By contrast, insights into the consequences of active *rotation* without self-propulsion remain scarce, even though this situation is relevant to a wide range of experimental systems [6] including spinning microorganisms [21, 91], treadmilling proteins [2], sperm cell and microtubule aggregates [67, 108], shaken chiral grains [111], light-powered chiral colloids [23], thermally and chemically powered liquid crystals [17, 123], electrorheological fluids [98], and biological and synthetic cilia driven by rotary molecular motors [47].

Until now, theoretical and numerical studies on ensembles of active spinners have separately addressed their phase dynamics and their spatial organization. The emergence and robustness of synchronized rotation in lattices of hydrodynamically-coupled rotors [87, 88] has been studied as an archetype of Kuramoto dynamics in coupled oscillator systems [105]. In these models the lattice geometry is imposed, a situation relevant, for instance, to

the propagation of metachronal waves at the surface of ciliated tissues [10, 64, 81, 127]. Local orientational synchronization has also been observed in self-organized disordered arrays of rotating rods [48, 107]. A separate class of numerical studies has been devoted to the *spatial structures* of ensembles of active spinners interacting either via contact or hydrodynamic interactions [1, 12, 22, 24, 32, 41, 120]. Special attention has been paid to phase separation in binary mixtures of counterrotating spinners and to hydrodynamic interactions yielding spatial ordering.

Here, we bridge the gap between these two lines of research. Combining numerical simulations and analytical theory we demonstrate the inherent interplay between the spatial structure and the phase dynamics of active spinners. We uncover a generic competition between monopole-like interactions that dominate at large separations, and shorter-range multipole gear-like interactions. We find that their interplay frustrates ordered states but also yields novel spatiotemporal order and unanticipated collective flows including edge currents.

We study a prototypical system of soft dimers interacting via repulsive interactions and undergoing unidirectional active rotation as sketched in fig. 3.1. When isolated, dimers spin in response to the active torque, attaining a steady-state spinning speed due to background friction. As they get closer, the multipole character of the pair interactions resists the rotation of adjacent dimers, fig. 3.1 b–c. At very high densities, the relative motion of neighbours is completely obstructed, fig. 3.1 d. By tuning the density, we explore how the frustration between monopole and multipole interactions plays out as their relative strengths are varied. We observe transitions from collections of independently spinning dimers to unusual crystal states which are ordered in particle position as well as orientation over time, to active spinner liquids, to jammed states. Repulsive interactions with boundaries also obstruct spinning fig. 3.1 e; to compensate, the system channels the rotational drive into linear momentum, giving rise to robust edge currents and collective motion.

Our model system consists of a two-dimensional ensemble of N like-charge dimers, each consisting of two point particles of mass m connected by a stiff link of length d, fig. 3.1 a. Point particles interact only via a repulsive pair potential of the Yukawa form $be^{-\kappa r}/r$, where b sets the overall strength of the repulsion, r is the inter-particle separation distance, and κ is the inverse screening length, see fig. 3.1. By setting $\kappa^{-1} \sim d$, we discourage dimer links from crossing each other and also maximize the orientational dependence of the effective pair interaction between dimers.

Each dimer is actively driven implemented by a torque $\tau = Fd$ implemented as a force dipole, fig. 3.1 a. Energy is dissipated by drag forces acting on each particle with associated drag coefficient γ. The equations of motion for the position, $\mathbf{r}_i$ and orientation θ_i of the i^{th} dimer are

$$2m\ddot{\mathbf{r}}_i = -2\gamma\dot{\mathbf{r}}_i - \partial_{\mathbf{r}_i}\sum_{j\neq i} V(\mathbf{r}_j - \mathbf{r}_i, \theta_i, \theta_j), \tag{3.1}$$

$$I\ddot{\theta}_i = \tau - \gamma_\Omega\dot{\theta}_i - \partial_{\theta_i}\sum_{j\neq i} \mathcal{V}(\mathbf{r}_j - \mathbf{r}_i, \theta_i, \theta_j), \tag{3.2}$$

where $I = \frac{1}{2}md^2$ and $\gamma_\Omega = \frac{1}{2}\gamma d^2$ are the moment of inertia and rotational friction coefficients respectively, and the position- and orientation-dependent interaction potentials V and $\mathcal{V}$ are derived from the Yukawa pair interactions between the point particles. An isolated dimer attains a steady state of counterclockwise rotation about its center with a constant spinning speed $\Omega_0 = \tau/\gamma_\Omega$, see fig. 3.1 b. We emphasize, however, that the instantaneous orientation of the dimer is *not* dictated by the drive, in contrast to systems where the dimer orientation is slaved to an external field, e.g. colloids driven by a rotating magnetic field [30, 70].

Upon rescaling distances by κ^{-1} and time by Ω_0^{-1}, the dynamical equations are characterized by three dimensionless quantities: κd, $\alpha \equiv I\tau/\gamma_\Omega^2$ which measures the characteristic dissipation time for angular momentum in units of the spinning period, and $\beta^{-1} \equiv \tau/\kappa b$ which quantifies the drive in units of the characteristic interaction energy scale. We focus here on the competition between rotational drive and interactions as the dimer *density* is varied for fixed α and β, as sketched in fig. 3.1 b–d. We constrain ourselves to the asymptotic limit where both $\alpha \gg 1$ and $\beta \gg 1$.

3.1 Systems of Active Spinners

In order to study systems of active interacting spinners, we conducted molecular dynamic simulations for eqs. (3.1) and (3.2). First, we characterized the bulk behavior of systems of active interacting spinners through simulations under periodic boundary conditions in which the dimer density was varied by changing the dimensions of the simulation box with constant screening parameter $\kappa = 0.725/d$, particle number $N = 768$, and activity parameters

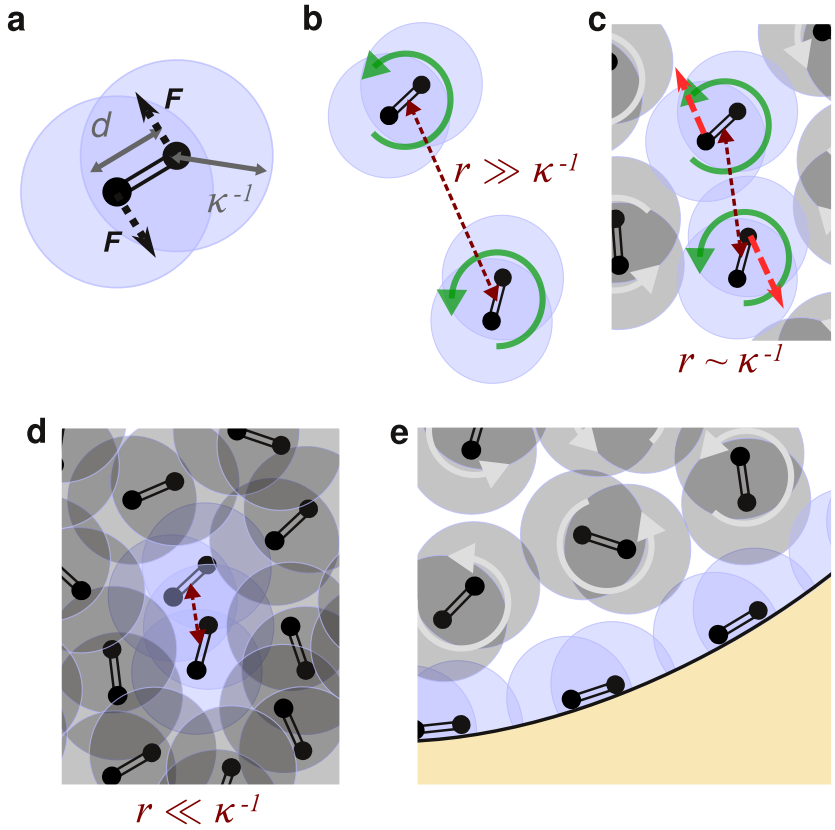

Figure 3.1: Competing rotation and interactions in active spinners. a, Make-up of a single self-spinning dimer, consisting of a pair of identically-charged particles (black dots), connected by a rigid rod of length d (double line). Particles repel each other with a Yukawa interaction with screening length κ^{-1} which determines the soft exclusion zone (light blue discs), beyond which the repulsion falls off exponentially with distance. Each particle experiences a force of magnitude F and direction indicated by dotted arrows, oriented to provide zero net force and a net torque $\tau = Fd$ on the dimer at all times. **b–d,** The density determines the influence of interactions on dimer dynamics. At large separations (**b**), interactions are negligible and dimers freely rotate at the terminal angular velocity set by the activity and the background drag. As separations become comparable to the screening length (**c**), adjacent dimers still rotate past each other but experience interaction forces (red dashed arrows show instantaneous force due to the interaction between two of the particles) that depend on their instantaneous orientations. At very high densities (**d**), interactions completely obstruct dimer rotation. **e,** Hard boundaries also obstruct dimer rotation, and their effect is transmitted into interior dimers by interactions.

$\alpha = 131$ and $\beta = 133$. Second, we characterized the behavior of bulk *and* edge of systems of active interacting spinners by confining such a system in a circular or slab-like geometry while we varied the density — similarly to the method used when characterizing the bulk behavior.

3.1.1 Phase behavior

We characterized the bulk behavior of interacting spinners through simulations under periodic boundary conditions in which the dimer density was varied by changing the dimensions of the simulation box with constant screening parameter $\kappa = 0.725/d$, particle number $N = 768$, and activity parameters $\alpha = 131$ and $\beta = 133$. Density is quantified by the packing fraction $\phi = A\rho$, where ρ is the number density of dimers and $A = \pi(d + 2\kappa^{-1})^2/4$ is the soft excluded area of a spinning dimer on time scales $t \gg 1/\Omega_0$. Figure 3.2 characterises the phase behavior of our system via changes in particle ordering, orientational ordering and dynamics in the nonequilibrium steady states reached at long times. Nearly identical behavior is observed for simulations with $N = 3072$, indicating that finite-size effects are negligible.

3.1.2 Active spinner crystals

At low packing fractions, the dimers self-organize into a hexagonal crystalline pattern, with little or no change in position, as shown for two representative densities in the first two panels of fig. 3.2 a. In this regime, the repulsions between dimers give rise to a Wigner-like crystal, quantified by high values of the bond-orientational order parameter $|\langle\psi_6\rangle|$ fig. 3.2 d [triangles]. Although the dimers are highly restricted in their position, they continue to spin without hindrance, attaining the same angular speed as an isolated dimer ($\langle\dot{\theta}\rangle \equiv \Omega \approx \Omega_0$, fig. 3.2 e). Apart from small fluctuations, the orientation of dimer i at time t has the form $\theta_i(t) = \Omega_0 t + \delta_i$ with the angular phase δ_i defined up to a global phase shift. This state is reminiscent of plastic crystals, but with the equilibrium fluctuations of the orientational degrees of freedom replaced by active rotation: we term this state an *active spinner crystal*.

The crystals display ordering not only in dimer positions, but also in dimer orientations which are phase-locked into regular spatial patterns. The angular phases δ_i take on a few discrete values determined by the lattice position. We find evidence for two distinct configurations. At low densities, δ_i acquires one of three values $\{0, \pi/3, 2\pi/3\}$, with no two neighbors sharing the same value fig. 3.2 c [first panel]. This pattern is identical to the equilibrium

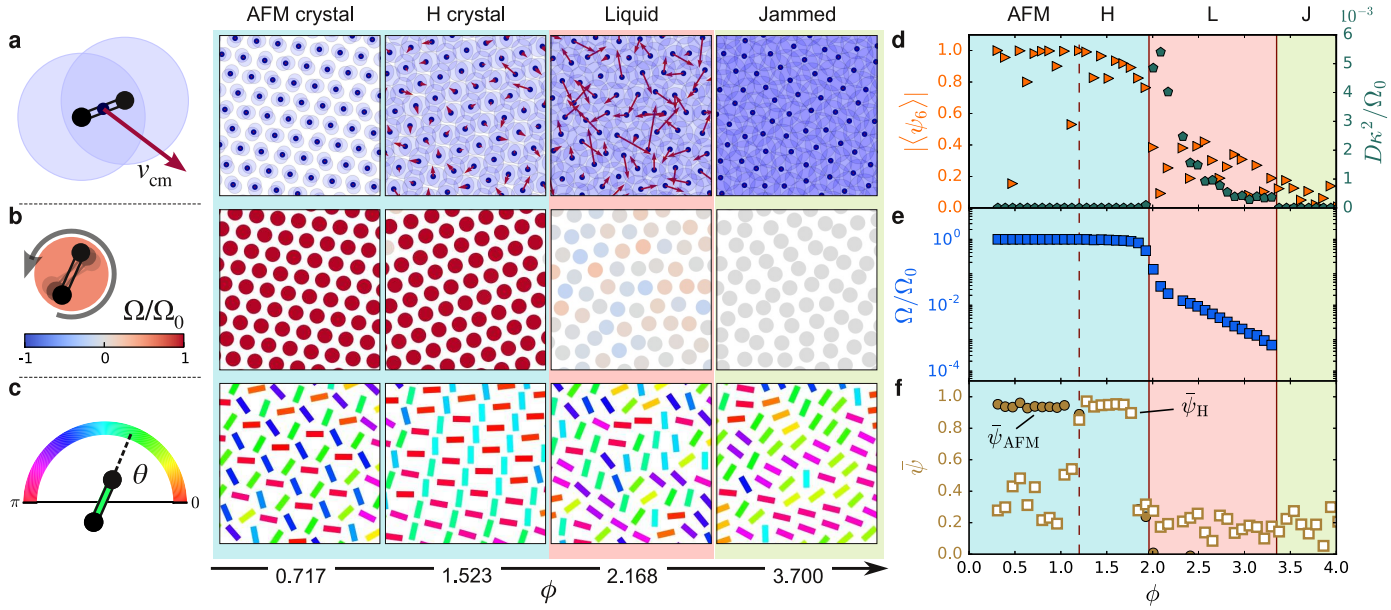

Figure 3.2: Bulk phases of the active spinner system. The behavior of dimer positions and orientations is investigated as a function of packing fraction ϕ, for constant activity level $\alpha = 131.026$. Each row highlights different physical quantities of the system, shown schematically and displayed for simulation snapshots for four representative values of ϕ in **a–c**. The snapshots cover roughly 10% of the simulation area. **a**: Center-of-mass position (dark dots) and velocities (red arrows), shown along with the soft exclusion area of individual charges (translucent discs); **b**: angular rotation speed Ω/Ω_0; **c**: orientation, represented by a fixed-length segment coloured by the angle made by the dimer with the x axis. Segment length does not represent actual dimer size. **d–f,** Ensemble measurements of steady-state physical quantities, as a function of ϕ. **d**: bond-orientational order parameter, and diffusivity of dimer positions; **e**: average angular speed. These quantities identify three distinct phases in different density ranges: crystal (blue background), liquid (red), and jammed (green). The rotational speed abruptly drops to zero (within numerical precision) in the jammed phase. **f**: order parameters quantifying Potts antiferromagnet (ψ_{AFM}) and striped herringbone (ψ_H) order in the phase relationships between rotating dimers in the crystal.

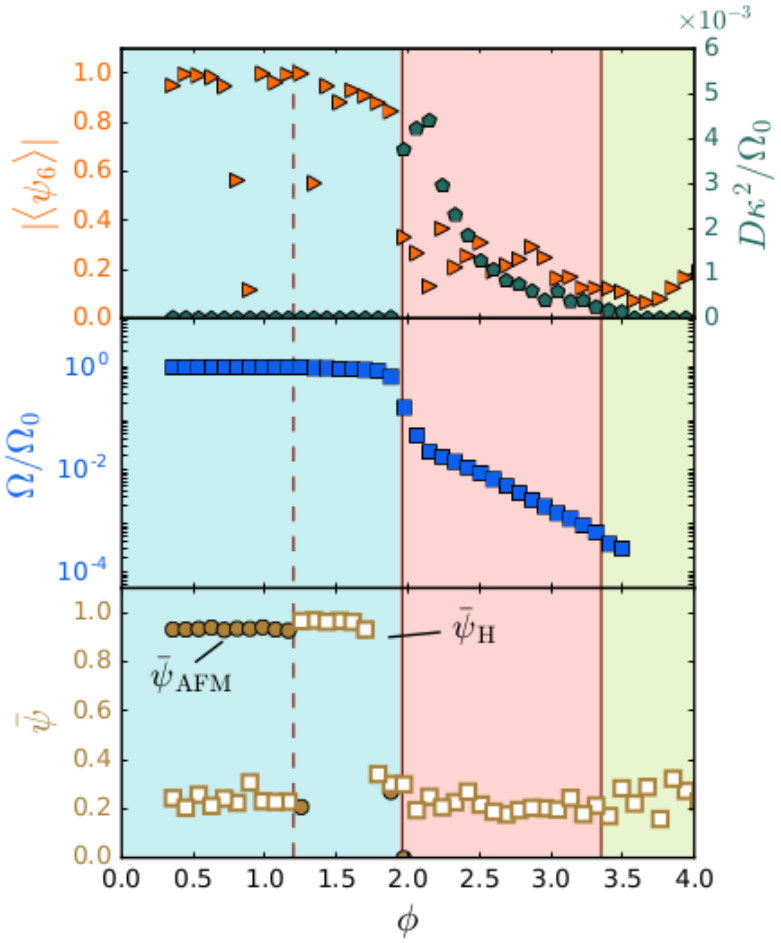

Figure 3.3: Ensemble measurements of steady-state physical quantities as a function of ϕ for a system with $N = 3072$ dimers, four times the system size of the simulations reported in fig. 3.2. **Top row**: bond-orientational order parameter, and diffusivity of dimer positions; **Middle row**: average angular speed. These quantities identify three distinct phases in different density ranges: crystal (blue background), liquid (red), and jammed (green). The rotational speed abruptly drops to zero (within numerical precision) in the jammed phase. **Bottom row**: order parameters quantifying Potts antiferromagnet (ψ_{AFM}) and striped herringbone (ψ_{H}) order in the phase relationships between rotating dimers in the crystal. The vertical lines are at the same values of ϕ as in fig. 3.2. The density ranges for the distinct phases are almost identical for $N = 768$ and $N = 3072$. The transition from liquid to jammed occurs at a slightly higher density, $\phi_{\mathrm{J}} \approx 3.5$ for $N = 3072$ (compared to $\phi_{\mathrm{J}} \approx 3.3$ for $N = 768$).

ground state of the 3-state Potts antiferromagnet (3P-AFM) on the triangular lattice [167]. When $\phi > \phi_{C_3\text{-}C_2} \approx 1.2$, the rotational symmetry of the pattern changes from C_3 to C_2 as stripes of alternating $\delta_i \in \{0, \pi/2\}$ form along a spontaneously-chosen lattice direction fig. 3.2 c [second panel]. This phase is a dynamical analogue of the striped herringbone (H) phase observed in lattices of elongated molecules [164]. Local order parameters ψ_{AFM} and ψ_{H}, defined in section 3.1.3, measure the extent to which phase differences among neighbouring dimers match those prescribed by the respective ordered states. As shown in fig. 3.2 f, the 3P-AFM and H states are each observed over a range of densities.

To understand the origin of the phase-locked patterns, we study a minimal model of the dimer–dimer interactions. To lowest order in dimer size d, each dimer is a superposition of a charge monopole and a charge quadrupole. The monopole repulsion arranges the dimer centers into a triangular crystal with lattice constant $a \sim 1/\sqrt{\phi}$. We assume that the dimer positions are thus fixed and focus on the orientation dynamics, (3.2), due to the quadrupolar interactions. When averaged over the common rotation period $2\pi/\Omega_0$, (3.2) reduces to $\partial_{\theta_i} \langle \sum_{j \neq i} \mathcal{V}(\mathbf{r}_j - \mathbf{r}_i, \theta_i, \theta_j) \rangle_t = 0$; i.e. the nonequilibrium steady states extremize the time-averaged potential energy as a function of orientation.

Upon ignoring fluctuations around the constant-speed evolution $\theta_i(t) = \Omega_0 t + \delta_i$, and considering only nearest-neighbour interactions among dimers, the average effective energy takes the compact form:

$$V_{\text{eff}} \equiv \langle \sum_{j \neq i} \mathcal{V}(\theta_i - \theta_j) \rangle_t = \sum_{\langle ij \rangle} \left[A_1 + A_2 \left(\frac{d}{a} \right)^4 \cos 2(\delta_i - \delta_j) \right], \qquad (3.3)$$

where A_1 and A_2 vary with density, see section 3.1.4 for details. For an infinite lattice of dimers, V_{eff} has arbitrarily many extrema. However, the extrema can be exhaustively listed for a *triangle* of neighbouring dimers. Up to a global phase shift and vertex permutations, the effective energy as a function of the phase shifts $\{\delta_1, \delta_2, \delta_3\}$ on the triangle vertices has three unique extrema at $\{0, \pi/3, 2\pi/3\}$, $\{0, 0, \pi/2\}$, and $\{0, 0, 0\}$. The 3P-AFM and H phases respectively extend the first and second of these extrema onto the infinite triangular lattice, and are thus also extremal states of the periodic crystal. In fact, the 3P-AFM state is the *global* energy minimum for V_{eff}, as seen by mapping the

effective energy to the antiferromagnetic XY model on the triangular lattice [162]♠. The extremum with phase values $\delta_i = 0$, which would correspond to all dimers sharing the same orientation at all times, maximizes the frustration of spinning by interactions and is not observed in our simulations.

In summary, spinning dimers are frustrated. The spatiotemporal-crystal states that are compatible with the mutual frustration of the position and orientation degrees of freedom are captured by the extrema of the effective potential V_{eff}. However, in principle, active spinner crystals could harbour a multitude of other phase-locked patterns, which cannot be reduced to repetitions of a single triangular unit but nevertheless extremize V_{eff}. These may be accessible by modifying the initial or boundary conditions, or the dynamics of approaching the nonequilibrium steady state.

3.1.3 Order parameters

The local bond-orientational order parameter $\psi_{6,i} = \sum_{j=1}^{n_i} e^{6\mathrm{i}\theta_{ij}}/n_i$, where j indexes the n_i nearest neighbours of i and θ_{ij} is the angle made by the bond connecting i and j with the x axis, measures the extent to which the neighbours of dimer i match the orientational order of the triangular lattice. The global order parameter $|\langle\psi_6\rangle| = |\sum_{i=1}^{N} \psi_{6,i}/N|$ measures the extent to which local bond orientations are aligned across the system. A perfect triangular lattice has $|\langle\psi_6\rangle| = 1$.

The local order parameters $\psi_{\text{AFM},i}$ and $\psi_{\text{H},i}$ report whether the orientations of dimer i and its nearest neighbours j (identified via a Delaunay triangulation) are consistent with the expected phase differences for the 3P-AFM and H crystal phases respectively. To identify the 3P-AFM phase, we check whether orientation differences between neighbours are $\pm\pi/3$, by computing:

$$\psi_{\text{AFM},i} = \frac{1}{z_i}\sum_{j=1}^{z_i} 1 - \frac{1}{3}\left[4\cos^2(\theta_{ij}) - 1\right]^2, \tag{3.4}$$

♠The effective energy inherits a discrete and a continuous ground-state degeneracy from the antiferromagnetic XY model. An arbitrary global phase shift gives the same state, but this is equivalent to a choice of $t = 0$ in the description of the orientations. The discrete degeneracy is in the chirality of phase order ($0 \to \pi/3 \to 2\pi/3$ vs. $0 \to 2\pi/3 \to \pi/3$) upon circling a plaquette. Adjacent plaquettes always have opposite chirality, and the two possible chirality arrangements on the triangular lattice provide two distinct ground states.

where $\theta_{ij} = \theta_i - \theta_j$ and z_i is the number of neighbours of dimer i. The expression evaluates to unity if $[(\theta_i - \theta_j) \mod \pi] \in \{\pi/3, 2\pi/3\}$ for all neighbours, and has an expectation value of zero if angle differences are randomly distributed.

For the H phase, we first arrange the neighbours in order of increasing angle made by the link connecting i and j with the x axis. Our goal is to evaluate the closeness of all possible circular shifts of this neighbour arrangement with the sequence $S \equiv \{0, \pi/2, \pi/2, 0, \pi/2, \pi/2\}$. We define the shift k as the integer in $\{0, 1, 2\}$ which minimizes $\sin^2(\theta_{ik}) + \sin^2(\theta_i - \theta_{k+3})$ in the ordered arrangement. The local order parameter is then computed via:

$$\psi_{\mathrm{H},i} = -\frac{1}{z_i}\sum_{j=1}^{z_i} \cos\left(\begin{cases} 2\theta_{ij} + \pi, & \text{if } j \mod 3 = k \\ 2\theta_{ij}, & \text{otherwise} \end{cases}\right), \tag{3.5}$$

which evaluates to unity only if the sequence of θ_{ij} starting from $j = k$ matches S and is close to zero for a random distribution of dimer orientations.

Under periodic boundary conditions, the crystals form phase-locked domains separated by defects and grain boundaries which bring down the value of the order parameters from unity when averaged over all points. In fig. 3.2 f, we identify the predominant local order within domains by plotting the most probable values $\bar{\psi}_{\mathrm{AFM}}$ and $\bar{\psi}_{\mathrm{H}}$. These are obtained by binning the local values ψ_i from every 50^{th} frame in the range $8000 \leq p \leq 10000$ into 20 equally spaced bins, and reporting the coordinate of the bin with highest occupancy.

3.1.4 Effective interaction between dimer pairs

In the limit that the dimer length d is small compared to the dimer separation, each dimer can be considered a superposition of a monopole carrying the net charge $2b$ and a quadrupole charge distribution. Therefore, the interaction between a pair of dimers can be written as a sum of monopole–monopole, monopole–quadrupole, and quadrupole–quadrupole terms. The monopole–monopole contribution is independent of dimer orientation. Suppose the angle made by dimer i evolves in time as $\theta_i = \Omega_0 t + \delta_i$. By symmetry considerations, the monopole–quadrupole contribution integrates to a quantity which is independent of the phases δ_i. The quadrupole–quadrupole contribution does depend on the relative phases, and has the form

$$E_{ij} = J(r_{ij})\cos(2\theta_i - 2\theta_j) + K(r_{ij})\cos(2\theta_i + 2\theta_j - 4\phi_{ij}), \tag{3.6}$$

where ϕ_{ij} is the angle made by the link connecting i and j with the x-axis, and J, K are functions of the center-of-mass separation r_{ij}, set by the Yukawa parameters:

$$J(r) = \frac{b}{128r}\left(\frac{d}{r}\right)^4 e^{-\kappa r}[9(1+\kappa r) + 5(\kappa r)^2 + 2(\kappa r)^3 + (\kappa r)^4], \tag{3.7}$$

$$K(r) = \frac{b}{128r}\left(\frac{d}{r}\right)^4 e^{-\kappa r}[105(1+\kappa r) + 45(\kappa r)^2 + 10(\kappa r)^3 + (\kappa r)^4]. \tag{3.8}$$

For the rotating dipoles with constant angular speed Ω_0 with fixed center-of-mass positions separated by the lattice spacing a, we have

$$E_{ij} = J(a)\cos(2\delta_i - 2\delta_j) + K(a)\cos(4\Omega_0 t + 2\delta_i + 2\delta_j - 4\phi_{ij}). \tag{3.9}$$

When the energy is integrated over a cycle, the second term integrates to zero, and hence the average potential energy over the cycle is $(1/T)\int_0^T E_{ij}\,dt = J(a)\cos(2\delta_i - 2\delta_j)$.

3.1.5 Melting and kinetic arrest

We now elucidate how synchronized spinning motion frustrates positional order and melts dense spinner crystals. As the packing fraction is increased, we observe a *loss* of crystalline ordering, signalled by a sharp drop in $|\langle\psi_6\rangle|$ from 1 to 0.2 at $\phi = \phi_{\text{melt}} \approx 1.9$. This drop coincides with the onset of diffusive dynamics of the dimer centers of mass at long times. The diffusivity $D \equiv \lim_{t\to\infty}\langle|\mathbf{r}_i(t_0+t) - \mathbf{r}_i(t)|^2\rangle_i/t$ is nonzero for a range of densities above ϕ_{melt}, characteristic of a liquid phase. Melting is accompanied by a disruption of the phase-locked spinning dynamics, as quantified by (i) a drop in the average spin velocity to below $0.1\Omega_0$, fig. 3.2 e, (ii) a marked increase in spin speed fluctuations, fig. 3.4, and (iii) a loss of H order in the orientations, fig. 3.2 f. Figure 3.2 a–c (third column) shows a typical liquid configuration with no discernible order in the positions, orientations, or spinning speeds.

The melting of the dimer crystal upon increasing the density, at odds with the typical behavior of athermal or equilibrium repulsive particles, is a direct result of the orientational dependence of dimer–dimer interactions coupled with the active spinning. The monopole part of the pair interaction is responsible for the crystalline arrangement of dimer centers. The quadrupolar component generates a gearing effect, which hinders the activity-driven co-rotation of

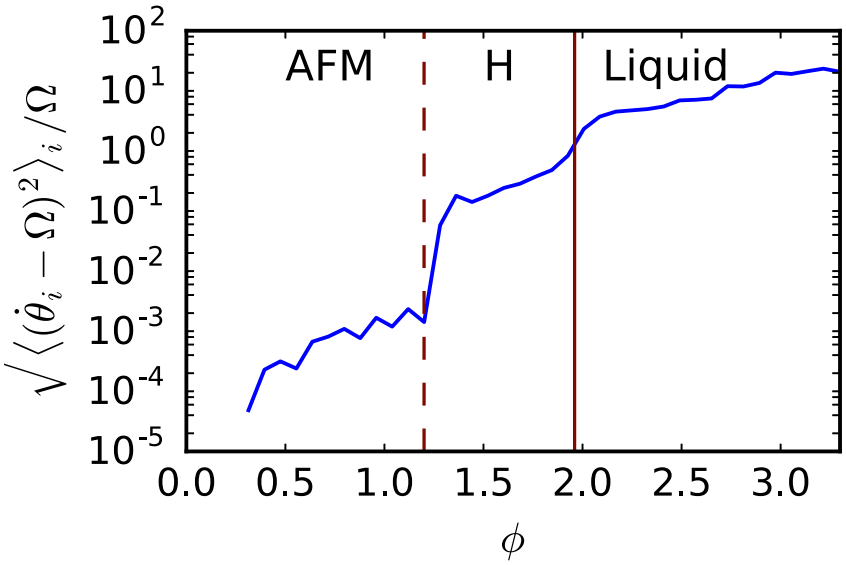

Figure 3.4: Fluctuations in dimer spin velocities $\dot{\theta}_i$ around their mean value Ω in the steady state for the simulations under periodic boundary conditions with $\alpha = 131$, $\beta = 0.0075$. The fluctuations are quantified by the standard deviation of spin velocities, normalized by their mean. The normalized fluctuations are negligible in the 3P-AFM crystal phase ($\phi < 1.2$) and small in the H crystal phase ($1.2 < \phi < 1.9$). They become very large in the liquid phase ($\phi > 1.9$), showing that dimers no longer rotate uniformly in the liquid; their rotational dynamics are dominated by interactions, which change constantly as dimers diffuse through the liquid. In the jammed phase ($\phi > 3.3$), the mean spin velocity $\Omega = 0$ and the normalized spread in spin velocities is undefined.

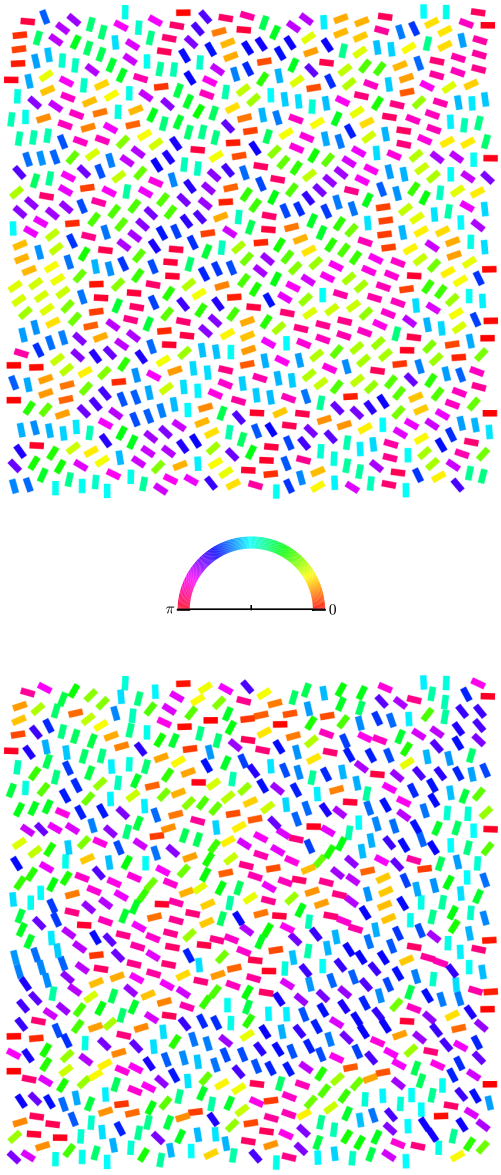

Figure 3.5: Snapshot of a simulation in the jammed phase ($\alpha = 131.026, \phi = 3.7$) coloured by (top) orientation angle and (bottom) orientation angle multiplied by 3. Regions of uniform colour on the right indicate regions where dimers are aligned modulo $\pi/3$.

adjacent dimers as shown schematically in fig. 3.2 1c. The competition between interactions and active spinning results in geometrical frustration of the crystalline order, akin to the frustration of antiferromagnetic Ising spins on the triangular lattice. Increasing the density strengthens the quadrupolar component of the interactions relative to the monopole component, *de*stabilizing the crystal at the threshold packing fraction ϕ_{melt}. In the liquid state, the frustration of in-place dimer rotation by interactions is partially relieved by dimers constantly sliding past each other, at the cost of crystalline and phase-locked order.

Upon increasing the packing fraction beyond ϕ_{melt}, the diffusive and spinning dynamics slow down as interactions become more prominent. At $\phi = \phi_{\text{J}} \approx 3.3$, the diffusivity and spinning speed of the ensemble both drop abruptly to zero, signifying a sharp transition from a liquid to a frozen solid in which interactions completely overwhelm the external drive [36]. As shown by representative snapshots fig. 3.2 a–c [fourth column] and the hexagonal order parameter fig. 3.2 d, the dimer positions and orientations in the frozen state do not exhibit the ordering of the crystalline phases. However, a different form of short-range orientational order persists: dimers tend to form ribbon-like assemblies which share a common alignment, see fig. 3.2 c [fourth panel], and fig. 3.5. This structure, which locally resembles smectic ordering in liquid crystals, is a consequence of the constraints on tightly packing repulsive dimers. The full description of this state, reminiscent of a degenerate crystal [156], goes beyond the scope of our work.

3.2 Confinement-induced collective motion

At a microscopic level, the bulk phases are distinguished by the relative importance of rotational drive and orientation-dependent interactions. For a steady state to be attained, torques must be balanced globally as well; in a confined system, the overall torque may be balanced by viscous drag as well as boundary forces. To investigate the interplay between rotational drive, interactions, and confinement, we simulated a system confined by a circular frictionless boundary as depicted in fig. 3.6 a, for the same particle number ($N = 768$), activity level and density range as in fig. 3.2. Densities are changed by varying the circle radius, since $\phi = NA/\pi R^2$. Figure 3.6 a shows the dimer center-of-mass motion for three representative densities across different phases, all of which display spontaneous macroscopic flows.

Measurements of the coarse-grained azimuthal velocity $v_\theta(r)$ as a function of distance r from the disc center, see section 3.3, reveal qualitative differences in the collective flows across phases. In both the crystal ($\phi = 0.827$) and frozen ($\phi = 3.750$) phases, the angular velocity about the disc center, $\omega(r) = v_\theta(r)/r$, is constant throughout the disc fig. 3.6 b, showing that the ensemble rotates around the center in unison as a rigid body. By contrast, the angular velocity profile is nonuniform for the liquid ($\phi = 2.395$), growing monotonically with distance from the disc center. These distinct behaviors persist over the entire phase diagram, as shown in fig. 3.6 c which compares the steady-state values of the flow angular velocity at the center [$\omega(0)$] and edge [$\omega(R)$] of the disc as a function of density. The center and edge values coincide in the solid phases, consistent with rigid-body rotation, whereas the liquid phase shows a persistent enhancement of flow at the edge. Collective vortical motion and boundary flows were previously demonstrated in suspensions of swimming cells [40, 62]. Their spatial structure and physical origin are, however, profoundly different from the confinement-induced flows reported here, which depend on the chiral activity of the spinners as we now elucidate.

3.2.1 Spontaneous collective rotation of rigid phases

The rigid-body rotation in the two solid phases, ordered and jammed, can be understood by balancing torques about the center of the circular boundary to obtain an acceleration-free steady state. The forces exerted by the boundary, being radially oriented, do not exert torque. Thus, the driving torques acting on the dimers must be balanced by drag forces. In the crystal interior, dimers homogeneously and steadily spin about their individual centers at a rate Ω_0, fig. 3.6 a, and the resulting friction balances the driving torques at all times. However, the spinning of the outermost layer of N_e dimers is obstructed by the hard boundary as shown schematically in fig. 3.1 e, which implies that the driving torques on these dimers are not balanced by spinning. Rather, these torques drive an overall rotation of the crystal. The corresponding rigid-body rotation speed, ω_rb, is obtained by balancing the net drive $N_\mathrm{e}\tau$ against the net drag torque due to the rigid-body rotation which scales as $N\gamma\Omega R^2$, thereby leading to $\omega_\mathrm{rb} \sim (N_\mathrm{e}/N)\tau/\gamma R^2 \propto \phi$.

In the frozen phase, local spinning of dimers relative to their neighbours is completely frustrated by interactions. Therefore, the entire external torque $N\tau$ is balanced solely by the drag due to orbital motion, giving rise to $\omega_\mathrm{rb} \sim \tau/\gamma R^2 \propto \phi$. The measured rotation speeds quantitatively match the predictions due to overall torque balance — solid and dashed lines in fig. 3.6 c.

3.2.2 Emergent edge current in active spinner liquids

The rigid-body motion of the two solid phases relies on the transmission of torque via shear stresses throughout the sample. If the disc is partitioned into circular annuli, the net external drive acting on each annulus differs from the net drag torque; neighboring annuli must exert shear forces on each other to balance the total torque. Unlike the solid phases, the liquid cannot support a shear stress through elastic deformations, which qualitatively explains the absence of pure rigid-body rotation, fig. 3.6 a and b. For a quantitative description of the emergent flow, we use a continuum theory of an active chiral liquid coupled to a solid substrate. This phenomenological model, introduced in Stark et al. [109] and Tsai et al. [111], generalizes the so-called micropolar-fluid hydrodynamics [66, 171] by including couplings to a frictional substrate.

Assuming incompressibility (as justified by the lack of significant spatial variations in dimer density), the hydrodynamic description relies solely on the conservation of momentum and angular momentum, and therefore involves two coarse-grained fields: the flow velocity $\mathbf{v}(\mathbf{r})$, and the internal angular rotation, or spin, field $\Omega(\mathbf{r})$. The hydrodynamic equations take on a compact form when written in terms of $\Omega(\mathbf{r})$ and the scalar vorticity, $\zeta(\mathbf{r}) = \frac{1}{2}\hat{\mathbf{z}} \cdot \nabla \times \mathbf{v}(\mathbf{r})$. In the viscous steady-state limit, these equations, which respectively amount to local torque and force balance, are [109, 111]:

$$D_\Omega \nabla^2 \Omega - \Gamma^\Omega \Omega - \Gamma(\Omega - \zeta) + \rho\tau = 0, \tag{3.10}$$

$$(4\eta + \Gamma)\nabla^2 \zeta - 4\Gamma^v \zeta - \Gamma \nabla^2 \Omega = 0, \tag{3.11}$$

where ρ is the active-spinner-fluid density, η is the shear viscosity, and D_Ω is a spin viscosity controlling the diffusive transport of angular momentum. The coefficients Γ^Ω and Γ^v quantify the dissipation of angular and linear momentum respectively due to substrate friction. The crucial spin-vorticity coupling is embodied in the rolling friction Γ, which coarse-grains the frustration between rotations and interactions outlined in fig. 3.1 c. Orientation-dependent interactions hinder the free spinning of adjacent fluid elements, causing shear stresses proportional to Γ unless the elements flow past each other in such a way that the vorticity cancels the local spin.

Analysis of the hydrodynamic equations reveals that spatial variations in the local spin field induce persistent flows. In the absence of boundaries, the equations admit the flow-free solution $\Omega = \rho\tau/(\Gamma^\Omega + \Gamma) = \Omega$, $\zeta = 0$. If a hard boundary hinders spinning, however, $\Omega(\mathbf{r})$ varies from its value imposed by the boundary to the constant interior value Ω over a length scale $\lambda_\Omega =$

$[D_\Omega/(\Gamma+\Gamma_\Omega)]^{\frac{1}{2}}$ set by the competition between diffusion and dissipation of local spin. The spatial variations in Ω, confined to the boundary, act as a source for vorticity which itself decays over a length scale $\lambda_\zeta = [(4\eta+\Gamma)/(4\Gamma^v)]^{\frac{1}{2}}$ set by drag. These predictions match the simulation results, and a fit to radially symmetric spin and flow fields (dashed lines in fig. 3.6 b second panel) provides quantitative agreement with four fitting parameters, see section 3.2.3 for more details.

The spontaneous liquid flow only requires the obstruction of spinning by the boundary, independently of its geometry. To highlight the robustness of this emergent flow, we also study active spinner liquids in a slab geometry with two edges aligned perpendicular to the x axis and periodic boundary conditions along y, as shown in fig. 3.6 e. This geometry suppresses rigid-body rotation in all phases; excess driving torques are balanced by normal boundary forces. Accordingly, no dimer motion is measured in the crystal and jammed phases, fig. 3.6 d. However, a persistent flow parallel to the slab edges arises in the liquid phase, demonstrating that the emergence of localized shear flows at edges is a *robust* feature of geometrically confined active spinner liquids. The mechanism for the edge current is the exchange between local spin and vorticity described above, which hinges on the orientation dependence of dimer-dimer interactions. The hydrodynamic description quantitatively reproduces the flow velocity profile $v_y(x)$ and spin field $\Omega(x)$, fig. 3.6 e [dashed lines].

3.2.3 Hydrodynamic model

In this section, we derive closed-form approximate solutions to the hydrodynamic equations, eqs. (3.10) and (3.11) of the main text, which are useful for numerical fitting to the spin and velocity profiles of the active spinner liquid under confinement. We follow Tsai et al. [111] and introduce lengths via $\lambda_\Omega^2 = D_\Omega/(\Gamma+\Gamma_\Omega)$ and $\lambda_\zeta^{-2} = 4\Gamma^v/(4\eta+\Gamma)$, and unitless parameters $p = \Gamma/(\Gamma+\Gamma^\Omega)$ and $q = \Gamma/(4\eta+\Gamma)$. Then the equations become:

$$(\lambda_\Omega^2\nabla^2 - 1)\Omega + p\zeta + \tilde{\tau} = 0, \tag{3.12}$$

$$(\nabla^2 - \lambda_\zeta^{-2})\zeta - q\nabla^2\Omega = 0, \tag{3.13}$$

where $\tilde{\tau} = \rho\tau/(\Gamma^\Omega+\Gamma) \sim \tau/(\gamma_\Omega + \Gamma/\rho)$. In the interior of a sample, away from the edges, we expect (and observe) $\Omega \approx \tilde{\tau} - p\zeta$. We also observe numerically that $p\zeta$ is negligible compared to the other two terms. Since $\langle\Omega\rangle \ll \Omega_0$ in the liquid phase, this implies $\Gamma \gg \Gamma^\Omega \Rightarrow p \approx 1$. With these

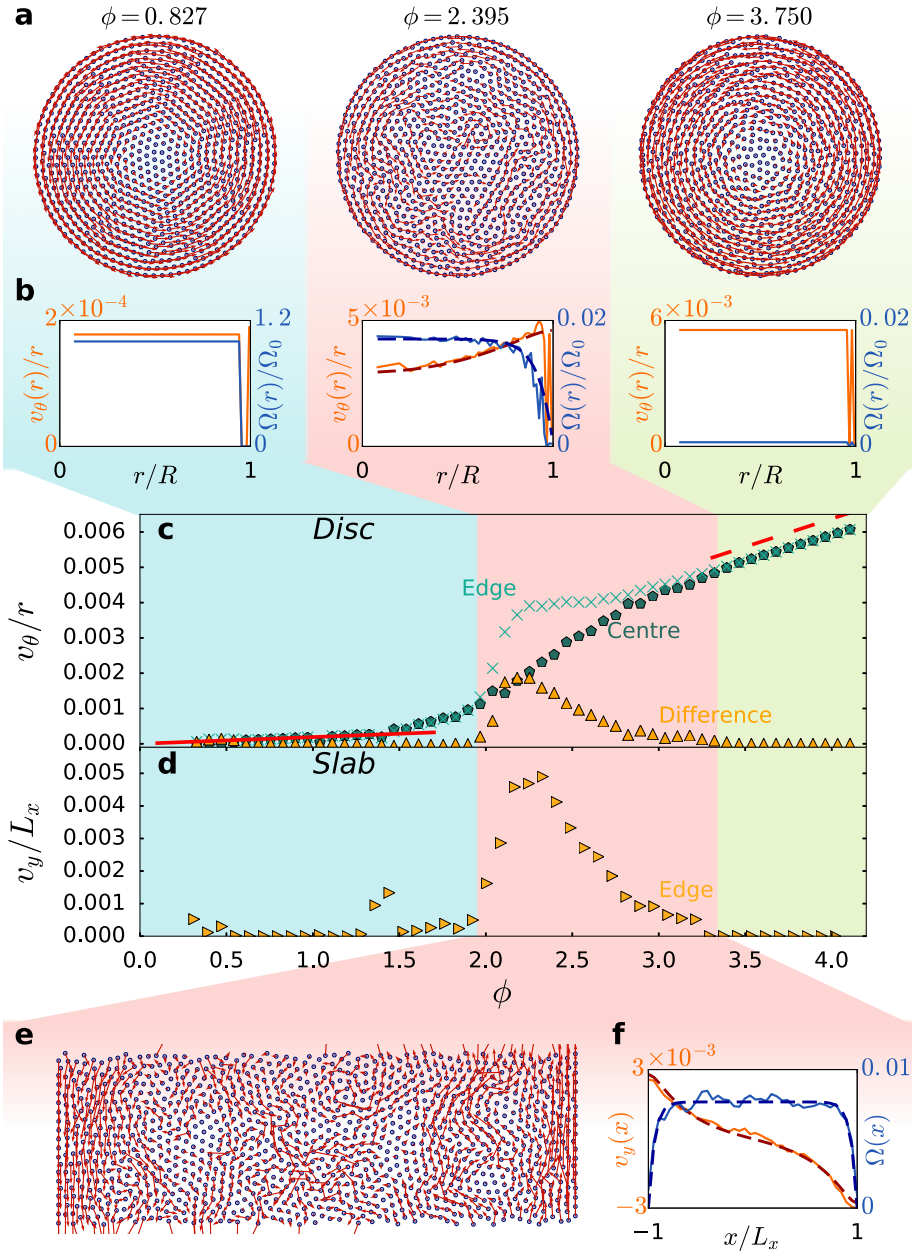

Figure 3.6: Collective motion reflects phase changes…

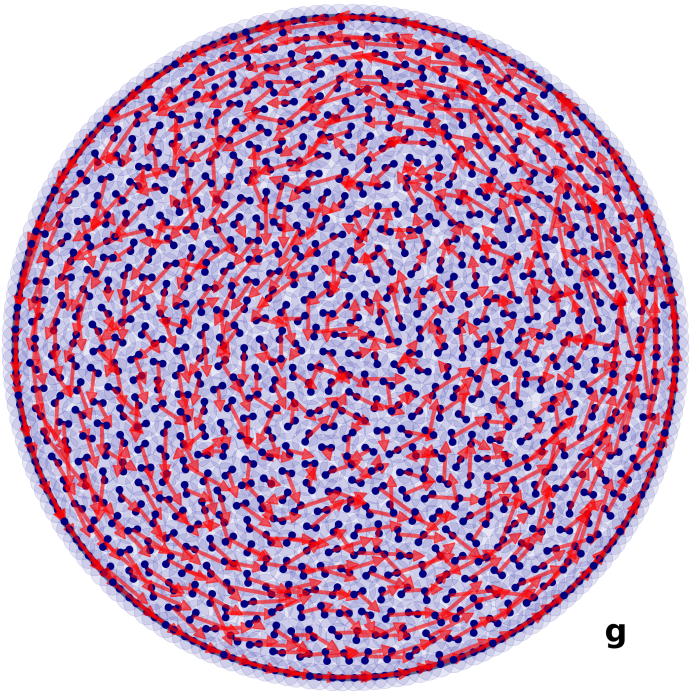

Figure 3.6: Collective motion reflects phase changes. a, Snapshots showing the drift of $N = 768$ dimers confined by a circular boundary. Arrows indicate the displacements after $\Delta t = 164/\Omega_0$ for (from left to right) $\phi = 0.827$ (crystal), $\phi = 2.395$ (liquid), and $\phi = 3.750$ (jammed). Arrows are scaled differently for visibility. **b,** Time-averaged steady-state radial distributions of the orbital angular speed $\omega(r)$ around the disc center (orange) and the local spin speed (blue), for the simulations shown in **a**. Dashed lines are fits to the hydrodynamic theory. **c,** Steady-state orbital angular speed $\omega(r)$ in simulation units as a function of density, measured at the disc center ($r = 0$) and edge ($r = R$). Coincidence of the two values is consistent with rigid-body rotation. The solid and dashed red lines show the theoretical prediction for the rigid-body rotation speed in the crystal and jammed phases respectively. **d,** Steady-state tangential speed of dimers at the wall as a function of density, for $N = 768$ dimers confined by two parallel walls perpendicular to the x direction and periodic boundary conditions along y. Density is varied by changing the area between the slabs while keeping the aspect ratio $L_y/L_x = 2$ unchanged. **e,** Snapshot of dimer motion for 768 dimers confined between parallel slabs at $\phi = 2.410$, with $L_y/L_x = 1/3$. **f,** Averaged steady-state velocity profile between the slabs (orange) and local spin speed (blue line) for the simulation shown in **e**. Dashed lines are fits to the hydrodynamic theory. **g** Snapshots zoom in showing the drift of $N = 768$ dimers confined by a circular boundary in the liquid phase. Arrows indicate the time averaged velocity.

simplifications, and the requirement of zero spin and zero tangential forces at the boundary, we get a closed-form solution for the two hydrodynamic fields. In the slab geometry, with slab boundaries at $x = \pm L/2$, they have the form:

$$\Omega(x) = \tilde{\tau}\left[1 - \operatorname{sech}\left(\frac{L}{2\lambda_\Omega}\right)\cosh\left(\frac{x}{\lambda_\Omega}\right)\right], \tag{3.14}$$

$$\zeta(x) = \frac{q\tilde{\tau}\left[\operatorname{sech}\left(\frac{L}{2\lambda_\zeta}\right)\cosh\left(\frac{x}{\lambda_\zeta}\right) - \operatorname{sech}\left(\frac{L}{2\lambda_\Omega}\right)\cosh\left(\frac{x}{\lambda_\Omega}\right)\right]}{1 - \lambda_\Omega^2/\lambda_\zeta^2}. \tag{3.15}$$

The corresponding velocity field is obtained by integrating the vorticity. The current magnitude at the edges ($x = \pm L/2$) is:

$$v_{\text{edge}} = \frac{2q\tilde{\tau}\left[\lambda_\zeta \tanh\left(\frac{L}{2\lambda_\zeta}\right) - \lambda_\Omega \tanh\left(\frac{L}{2\lambda_\Omega}\right)\right]}{1 - \lambda_\Omega^2/\lambda_\zeta^2}. \tag{3.16}$$

Using these results, we can extract the values of the lengths and dimensionless parameters from the simulations. We first fit the spin field $\Omega(x)$ since the decay length λ_Ω tends to be much smaller than λ_ζ, allowing the former to be fit accurately for narrow slabs where the width might be comparable to the latter. The fit to the spin field fixes the parameters $\tilde{\tau}$ and λ_Ω. The second fitting of the velocity field then fixes the remaining two parameters q and λ_ζ.

The parameter values obtained from the fit for the slab simulation in main text fig. 3.6 f, with $L = 121.43d$, are $\tilde{\tau} = 0.06627, q = 0.0150, \lambda_\Omega = 3.554d, \lambda_\zeta = 22.65d$. The approximation that $p\zeta \ll \Omega$ requires $q \ll 1$, satisfied by the fit.

The same procedure is used for a liquid confined to a disc of radius R, for which the approximate radially symmetric solution for the spin and vorticity fields is:

$$\Omega(r) = \tilde{\tau} - \frac{\tilde{\tau}R\left(1-\lambda_\Omega^2/\lambda_\zeta^2\right)I_2\left(\frac{R}{\lambda_\zeta}\right)I_0\left(\frac{r}{\lambda_\Omega}\right)}{2b\lambda_\zeta I_1\left(\frac{R}{\lambda_\zeta}\right)I_2\left(\frac{R}{\lambda_\Omega}\right)+I_2\left(\frac{R}{\lambda_\zeta}\right)\left(R(1-\lambda_\Omega^2/\lambda_\zeta^2)I_0\left(\frac{R}{\lambda_\Omega}\right)-2b\lambda_\Omega I_1\left(\frac{R}{\lambda_\Omega}\right)\right)}, \tag{3.17}$$

$$\zeta(r) = \frac{bR\tilde{\tau}\left[I_0\left(\frac{r}{\lambda_\zeta}\right)I_2\left(\frac{R}{\lambda_\Omega}\right)-I_0\left(\frac{r}{\lambda_\Omega}\right)I_2\left(\frac{R}{\lambda_\zeta}\right)\right]}{2\lambda_\zeta\left((b-1)+\lambda_\Omega^2/\lambda_\zeta^2\right)I_0\left(\frac{R}{\lambda_\Omega}\right)I_1\left(\frac{R}{\lambda_\zeta}\right)+I_0\left(\frac{R}{\lambda_\zeta}\right)\left[R(1-\lambda_\Omega^2/\lambda_\zeta^2)I_0\left(\frac{R}{\lambda_\Omega}\right)-2b\lambda_\Omega I_1\left(\frac{R}{\lambda_\Omega}\right)\right]}. \tag{3.18}$$

Here, I_m is the modified Bessel function of first kind of order m. The parameters obtained from the fit to the approximate solution for the disc simulation in fig. 3.6 b of the main text ($\phi = 2.395,\ R = 33.65d$) are $\tilde{\tau} = 0.1475, q = 0.0161, \lambda_\Omega = 2.484d, \lambda_\zeta = 15.61d$.

3.3 Computational methods

Our molecular dynamics simulations solve Newton's equations for a system of point particles with specified pairwise interactions, external forces, and drag coefficients. Particles interact with a pairwise repulsive Yukawa potential with identical charge b and screening length κ, enabled for all particle pairs with separation $r < 10\kappa^{-1}$. Dimers are created by connecting pairs of particles with stiff harmonic springs of equilibrium length d and spring constant $k = 10^4 b\kappa^3$. Torques are applied via an external force $F = \tau/d$ oriented perpendicular to the link at all times. Each point particle also experiences a drag force proportional to velocity with coefficient $-\gamma$. Simulations are initialized with dimers at random positions and orientations within the simulation box. Particle positions and velocities are updated by integrating Newton's equations using a symplectic Euler method with time step $\Delta t = 0.0086/\Omega_0$. A typical simulation runs for 10^7 time steps, taking roughly 100 CPU hours for system size $N = 768$ at the highest densities, with a snapshot of dimer data saved every 10^3 steps. Ensemble averages are carried out over the final 8000 snapshots.

Confining boundaries are implemented using a steep one-sided harmonic repulsive potential $V(x) = \frac{1}{2}k_\mathrm{w}x^2$ experienced by all particles, where x is the penetration distance into the boundary, and $k_\mathrm{w} = 3.14 \times 10^2 b\kappa^3$. For simulations confined by a circular boundary, coarse-grained fields of the form $f(r)$ are computed by dividing the simulation region into 39 concentric annuli with widths inversely proportional to their mean radius r so that the number of dimers is the same in each annulus on average. The relevant quantity averaged over all dimers occupying the annulus at r provides a discretized numerical estimate of the coarse-grained field value $f_p(r)$ in frame p. The estimate is then averaged over the final 8000 snapshots to obtain the coarse-grained field $f(r) = \langle f_p(r)\rangle_p$. A similar averaging provides the coarse-grained fields $\Omega(x)$ and $v_y(x)$ for the slab geometry, but with the simulation area between the slabs divided into 40 strips with edges parallel to the y axis. Averaging the relevant quantity over dimers occupying a strip centerd at x provides the discrete coarse-grained field value $f_p(x)$.

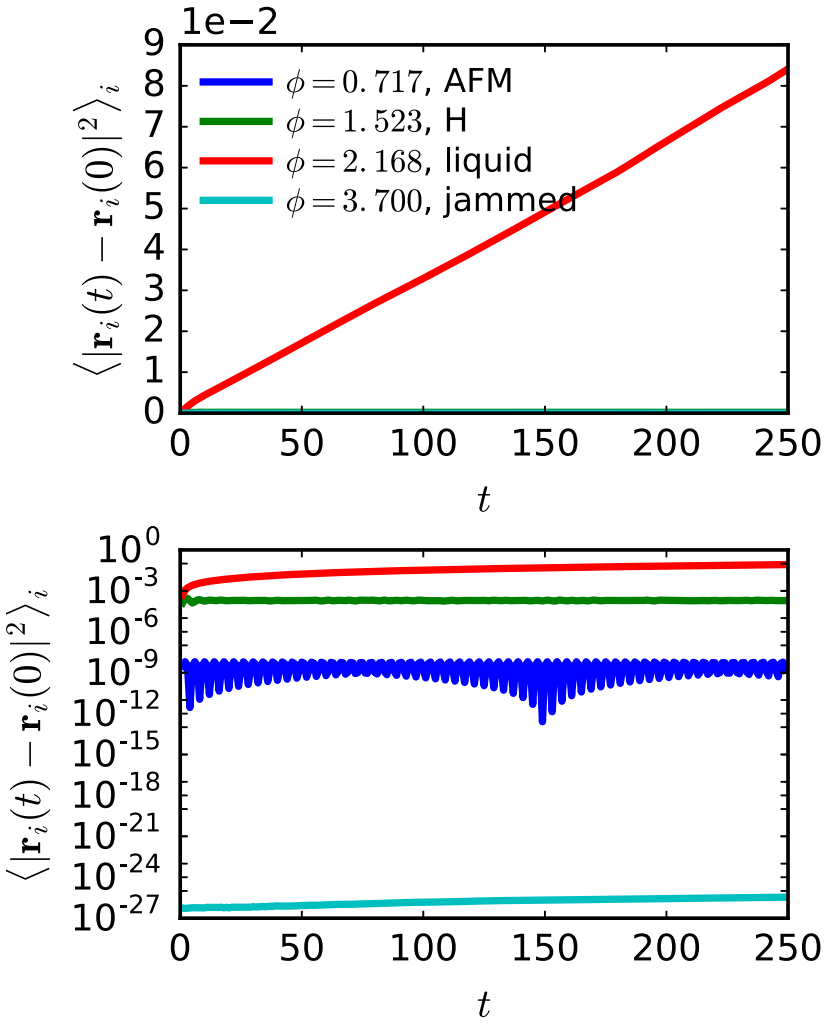

Figure 3.7: Mean squared displacement (MSD) of dimers over time, for the periodic system under four representative densities which are the same as in fig. 3.2. The MSD is calculated independently for 76 randomly chosen dimers (one-tenth of the total) and averaged over them. The bottom plot shows the same data on a logarithmic scale. The system in the liquid phase ($\phi = 2.168$) has diffusive dimer dynamics with the mean square displacement growing linearly with time. Dimers in the crystal ($\phi = 0.717$ and $\phi = 1.523$) and jammed ($\phi = 3.700$) states do not diffuse over long times. However, in the crystal phases there is a finite displacement at short times reflecting the vibrations of the dimers around their mean positions which are fixed over time. These vibrations are larger in the H phase compared to the AFM phase.

3.4 Conclusion

Combining numerical simulations and analytical theory, we have elucidated the phase behavior of interacting active spinners. The mutual frustration of positional and time-periodic orientational order has been shown to yield a variety of crystal and disordered phases. Although we have focused on the density dependence of the bulk and edge phenomena, the phases and their associated emergent flows persist over a broad range of activity strengths, see fig. 3.8, which makes experimental realizations feasible. Colloidal dumbbells [58, 121] spun by phoretic stresses [3] or Quincke rotation [43] would provide a near-literal realization of our model. More broadly, the essential ingredients of active spinners with orientation-dependent repulsive interactions are present in a wide variety of experimental systems including chiral liquid crystals confined to a monolayer and driven via the Lehmann effect [54], rotating nanorods propelled by biomolecular motors [134], and light-driven micromotors [15]. We also envision macroscopic realizations using chiral particles driven by airflow [35] or vibrations [111], with soft interactions provided by electrostatic or magnetic repulsion. Besides opening up new avenues to explore nonequilibrium physics in simple settings, the novel phases arising from the interplay between interactions and spinning may be exploited for tunable torque transmission [29] or for self-assembly of anisotropic particles into ordered patterns.

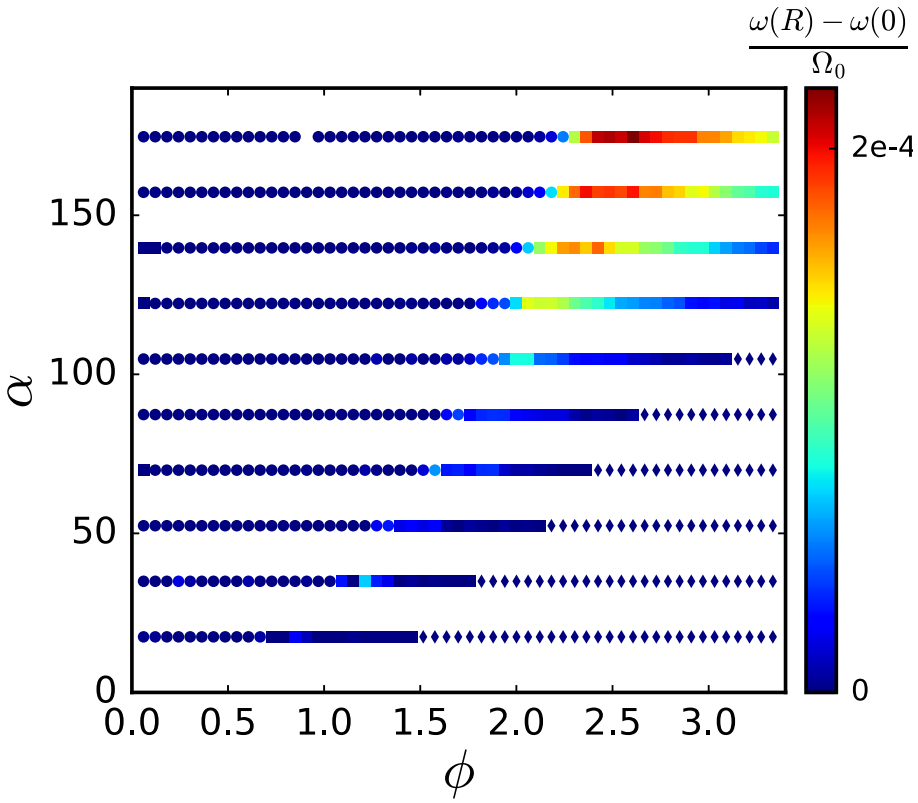

Figure 3.8: Bulk phases are reflected in edge currents and persist over a range of torques. The flow at the edge plotted as a function of activity level α and packing fraction ϕ in the disc geometry. In these simulations, the disc radius $R = 48.27d$ was kept constant and the density was varied by changing the number of dimers confined to the disc. The tangential flow velocity $v_\theta(r)$ was measured as for the systems in main text fig. 3.6, and the edge flow is reported as the difference in $\omega(r) = v_\theta(r)/r$ at the edge and center of the disc. Symbols are coloured by edge current magnitude, whereas symbol shapes are chosen by values of bulk properties that identify the different phases. **Circles,** Active rotator crystals, identified by $\langle\Omega\rangle > 0.4$ and $\langle\psi_6\rangle > 0.45$. **Diamonds,** Frozen phase, identified by $\langle\Omega\rangle < 10^{-5}$. **Squares,** Dynamic and disordered liquid-like states, that do not satisfy the previous criteria for the crystal and frozen phases.

Chapter 4.

Molecular dynamics on a curved substrate

The mathematical concept of space-time curvature has fundamentally changed the way we perceive and describe the physical world from the cosmological to the microscopic scale. In soft matter physics, substrate curvature has been shown to have a remarkable effect on two-dimensional films confined on it [5, 90, 104, 115, 124]. A common numerical method used to model such soft matter systems is molecular dynamics. Performing molecular dynamics on curved surfaces is not a straightforward task. The equations of motion become increasingly harder as the curvature becomes more complex. Where in the absence of curvature a free particle follows a straight line, in the presence of curvature a free particle follows a generalization of a straight line called a *geodesic* [113], see appendix D. Already in flat space, conventional numerical solutions to the equations of motion, called *integrators*, often fail to preserve the conserved quantities of these equations of motion, such as energy and momentum [103, 129, 136]. Examples of such integrators are *Forward Euler* and *Runge–Kutta method*, see appendices I and J, respectively. When an integrator *does* preserve these symmetries it is called *symplectic*. Examples of symplectic integrators in the absence of curvature are *Symplectic Euler* and *Velocity Verlet*, see appendices K and L. Even when a certain integrator is symplectic in the absence of curvature, however, it is not necessarily so in the presence of curvature, as these integrators are not explicitly designed to cope with curvature.

In this chapter, we will use the method of variational integrators [103, 129, 136] to derive a novel symplectic integrator that solves Newton's equations in the presence of curvature. First, we will derive Newton's equations in the presence of curvature. Second, we discuss how to discretize the equations of

motions in time whilst preserving the conserved quantities — by respecting the Lagrangian symmetries in accordance to Noether's theorem. Third, we apply the discussed techniques to derive a novel symplectic integrator algorithm that solves Newton's equations in the presence of curvature. Finally, we will illustrate how to apply the integrator to study the two-dimensional melting transition in the presence of curvature and give some preliminary results.

4.1 Newton's equations in the presence of curvature

Newton's equations on a Riemannian manifold can be found using Lagrangian mechanics, see appendix C. Let us define the metric tensor on our manifold to be $g_{\mu\nu}$ and we find the Lagrangian:

$$L = \tfrac{1}{2} m g_{\mu\nu} \dot{x}^\mu \dot{x}^\nu - V(x^\rho), \tag{4.1}$$

where m is the mass and $V(x^\rho)$ is some arbitrary interaction potential. Upon applying the Euler–Lagrange equations — eq. (C.3) — we find the conservative version of Newton's equations of motion in the presence of curvature:

$$m\left(\ddot{x}^\mu + \Gamma^\mu_{\sigma\rho} \dot{x}^\sigma \dot{x}^\rho\right) = -g^{\mu\nu} \partial_\nu V, \tag{4.2}$$

which can be made non-conservative by realizing that the right-hand side of eq. (4.2) is a force:

$$F^\mu = m\left(\ddot{x}^\mu + \Gamma^\mu_{\sigma\rho} \dot{x}^\sigma \dot{x}^\rho\right). \tag{4.3}$$

The symbols $\Gamma^\mu_{\sigma\rho}$ in eqs. (4.2) and (4.3) are called the Christoffel symbols of the second kind. Christoffel symbols of the second kind can be defined in terms of the metric tensor as:

$$\Gamma^\mu_{\sigma\rho} = \tfrac{1}{2} g^{\mu\lambda} \left(\partial_\sigma g_{\lambda\rho} + \partial_\rho g_{\sigma\lambda} - \partial_\lambda g^{\sigma\rho}\right), \tag{4.4}$$

Christoffel symbols of the first kind $\Gamma_{\mu\sigma\rho}$ are defined as such:

$$\Gamma_{\mu\sigma\rho} = g_{\mu\lambda}\Gamma^\lambda_{\sigma\rho} = \tfrac{1}{2}\left(\partial_\sigma g_{\mu\rho} + \partial_\rho g_{\sigma\mu} - \partial_\mu g_{\sigma\rho}\right). \tag{4.5}$$

It is worth noting that the Christoffel symbols are *not* tensors — they change when the coordinate system changes. From eq. (4.3) we obtain the geodesic equations

$$\ddot{x}^\mu + \Gamma^\mu_{\sigma\rho} \dot{x}^\sigma \dot{x}^\rho = 0. \tag{4.6}$$

The geodesic equations generalize the notion of a straight path♠ in the presence of curvature — see appendix D for a more detailed derivation.

♠Often, a straight path is also the shortest.

4.2 Variational integrators

Among the common methods to solve second order dynamical systems[♠] numerically are the Forward Euler and Runge–Kutta methods, see appendices I and J. For Newtonian systems there are, however, some shortcomings associated with these methods. The problem becomes apparent when considering the total energy or Hamiltonian H of such a system. When we look at $H_{i+j} - H_i > 0$ for $j > 0$ we realize that with increasing time steps the total energy of the system rises, see appendix M. The algorithms fail to preserve the Hamiltonian which ought to be constant, see appendix B. As a consequence, these numerical solutions will hence deviate from the actual path in phase space. The path could even be attracted by different fixed points — or worse, diverge, causing numerical *explosions*. The fundamental problem is that these algorithms do not respect the Lagrangian symmetries giving rise to conserved quantities by Noether's theorem. An energy-conserving numerical method would be highly desirable. Such an integrator would be symplectic.[♡] Symplectic integrators can be found using the method of *variational integrators* [103, 129, 136].

The idea behind variational integration is best illustrated within Lagrangian mechanics. We know how to derive Newton's equations of motion, eqs. (4.2) and (B.4), from the Lagrangian L using the Euler–Lagrange equation, eq. (C.3), by the so-called stationary action principle, as discussed in section 4.1 and appendix C. The Lagrangian L possesses symmetries that generate conserved quantities. Here, we want to solve the equations of motion for discrete time steps, recurrently, as our aim is to let a computer solve them. Hence, if we formulate a discretized version of the stationary action principle — appropriately — it should yield a discrete solution of the equations of motion *with* conservation of Lagrangian symmetries — at least up to certain order. The resulting numerical scheme is, hence, symplectic by definition. This is essentially what the method of variational integration accomplishes. We will continue to describe how the action can be discretized.

[♠] Systems of differential equations.

[♡] Strictly, symplecticity only preserves volume in phase space and total energy is only conserved for exponentially long periods of time. For variational integrators, however, also kinetic energy — or momentum — is strictly conserved.

Let us define the timestep h such that $t_{i+1} = t_i + h$. A discretized Lagrangian $L_D(x^\mu, \dot{x}^\mu)$ is found by:

$$L_D(x_i^\mu, x_{i+1}^\mu) = \int_{t_i}^{t_{i+1}} L(x^\mu, \dot{x}^\mu, t)\,\mathrm{d}t. \tag{4.7}$$

The action, eq. (C.1), in terms of the discretized Lagrangian is then given by

$$S = \sum_i L_D(x_i^\mu, x_{i+1}^\mu). \tag{4.8}$$

Now let us introduce the discrete-time partial derivative $\partial_\sigma^i = \frac{\partial}{\partial x_i^\sigma}$ for which:

$$\partial_\sigma^i x_k^\mu = \delta_\sigma^\mu \delta_{ik}. \tag{4.9}$$

The Euler–Lagrange equations are the equations that find the stationary points in the action, analogous to eqs. (C.2) and (C.3) in appendix C. The time-discrete version is given by:

$$\partial_\sigma^i S = 0, \tag{4.10}$$

which, hence, yields the discrete Euler–Lagrange equations:

$$\partial_\sigma^i L_D(x_{i-1}^\mu, x_i^\mu) + \partial_\sigma^i L_D(x_i^\mu, x_{i+1}^\mu) = 0. \tag{4.11}$$

The discrete Euler–Lagrange equations then yield the discrete-time equations of motion, *whilst preserving the Lagrangian symmetries*. Note that the discrete Lagrangian $L_D(x_i^\mu, x_{i+1}^\mu)$ is solely a function of position x_i^μ and not of velocity $\dot{x}_i^\mu$. The new velocity can be found explicitly by the following formula:

$$\dot{x}_{i+1}^\mu = \tfrac{1}{m}\delta^{\mu\sigma}\partial_\sigma^{i+1} L_D(x_i^\mu, x_{i+1}^\mu). \tag{4.12}$$

The old velocity is given by:

$$\dot{x}_i^\mu = -\tfrac{1}{m}\delta^{\mu\sigma}\partial_\sigma^{i} L_D(x_i^\mu, x_{i+1}^\mu). \tag{4.13}$$

This formula is generally implicit. Fortunately this is not a problem as most integration schemes only rely on eq. (4.12).

The method of variational integrators can be used to derive the symplectic Euler method and higher-order Velocity verlet method, reviewed in appendices K and L.

4.3 Symplectic integration with curvature

We will now move on to derive the analog of the symplectic Euler scheme in the presence of Riemannian curvature.[♠] The derivation will thus be very similar to the symplectic Euler derivation discussed in appendix K which also uses the variational integration method described in section 4.2. Now, however, we will use a Lagrangian that incorporates curvature $L = \frac{1}{2} m g_{\mu\nu} \dot{x}^\mu \dot{x}^\nu - V(x^\rho)$, as discussed in section 4.1 — particularly eq. (4.1). We will continue to discretize this Lagrangian using eq. (4.7). We approximate the integral using the rectangle method — see eq. (H.6) in appendix H. We will additionally invoke a discrete velocity:

$$\dot{x}^\mu = \tfrac{1}{h} \left(x^\mu_{i+1} - x^\mu_i \right). \tag{4.14}$$

Doing so results into the following discrete Lagrangian:

$$L_D^{\text{rect}}(x^\mu_i, x^\mu_{i+1}) = \tfrac{m}{2h} \left(g^i_{\mu\nu} x^\mu_{i+1} x^\nu_{i+1} - 2 g^i_{\mu\nu} x^\mu_{i+1} x^\nu_i + g^i_{\mu\nu} x^\mu_i x^\nu_i \right) - h V_i. \tag{4.15}$$

Note that contrary to the Euclidean space case, the metric $g_{\mu\nu}(x^\mu)$ in the Lagrangian *is* a function of position. Hence, its discrete counterpart is a function of the discrete position $g^i_{\mu\nu} = g_{\mu\nu}(x^\mu_i)$.[♡] We will then continue to apply the discrete Euler–Lagrange equations, eq. (4.11), to our discrete Lagrangian, eq. (4.15). In order to do so, we establish the following identities:

$$\partial^i_\sigma g^j_{\mu\nu} x^\mu_k x^\nu_l = \delta_{ij} \left(\Gamma^j_{\nu\sigma\mu} + \Gamma^j_{\mu\sigma\nu} \right) x^\mu_k x^\nu_l + g^j_{\mu\nu} \left(\delta_{ik} \delta^\mu_\sigma x^\nu_l + \delta_{il} x^\mu_k \delta^\nu_\sigma \right), \tag{4.16}$$

which holds because[♣]

$$\partial^i_\sigma g^j_{\mu\nu} = \delta_{ij} \left(\Gamma^{\lambda\, j}_{\sigma\mu} g^j_{\lambda\nu} + \Gamma^{\lambda\, j}_{\sigma\nu} g^j_{\mu\lambda} \right) = \delta_{ij} \left(\Gamma^j_{\nu\sigma\mu} + \Gamma^j_{\mu\sigma\nu} \right). \tag{4.17}$$

Using these identities we apply the Euler–Lagrange equations and obtain:

$$\begin{aligned} &\Gamma^i_{\nu\sigma\mu} \left(x^\mu_{i+1} x^\nu_{i+1} + x^\mu_i x^\nu_i \right) - \left(\Gamma^i_{\nu\sigma\mu} + \Gamma^i_{\mu\sigma\nu} \right) x^\mu_{i+1} x^\nu_i + \\ &g^i_{\sigma\mu} \left(x^\mu_i - x^\mu_{i+1} \right) + g^{i-1}_{\sigma\mu} \left(x^\mu_i - x^\mu_{i-1} \right) - \tfrac{h^2}{m} \partial^i_\sigma V_i = 0, \end{aligned} \tag{4.18}$$

[♠] As far as is known to the author, this will be the first explicit publication of this kind of symplectic integrator for Riemannian manifolds.

[♡] In the absence of curvature this remark becomes irrelevant because then $g_{\mu\nu} = \delta_{\mu\nu}$ an therefore $\delta^i_{\mu\nu} = \delta^j_{\mu\nu}$ for all i, j — see eq. (K.2) in appendix K.

[♣] The Christoffel symbols of first and second kind $\Gamma_{\mu\sigma\rho}$ and $\Gamma^\mu_{\sigma\rho}$ are respectively defined in eqs. (4.4) and (4.5).

which can be simplified by introducing the variable $\epsilon_i^\mu = x_{i+1}^\mu - x_i^\mu$ yielding:

$$\Gamma^i_{\nu\sigma\mu}\epsilon_i^\mu\epsilon_i^\nu - g^i_{\sigma\mu}\epsilon_i^\mu + g^{i-1}_{\sigma\mu}\left(x_i^\mu - x_{i-1}^\mu\right) - \tfrac{h^2}{m}\partial^i_\sigma V_i = 0. \tag{4.19}$$

Now let us introduce the following variables for our convenience:

$$A^i_{\sigma\mu\nu} = \Gamma^i_{\nu\sigma\mu}, \tag{4.20}$$

$$B^i_{\sigma\mu} = -g^i_{\sigma\mu}, \tag{4.21}$$

$$C^{i,i-1}_\sigma = g^{i-1}_{\sigma\mu}\left(x_i^\mu - x_{i-1}^\mu\right) - \tfrac{h^2}{m}\partial^i_\sigma V_i. \tag{4.22}$$

We then solve for ϵ_i^μ in the equation:

$$A^i_{\sigma\mu\nu}\epsilon_i^\mu\epsilon_i^\nu + B^i_{\sigma\mu}\epsilon_i^\mu + C^{i,i-1}_\sigma = 0. \tag{4.23}$$

Since denoting a particular timestep i at this point, has become unnecessary we may drop the Latin time index in order simplify even further:

$$A_{\sigma\mu\nu}\epsilon^\mu\epsilon^\nu + B_{\sigma\mu}\epsilon^\mu + C_\sigma = 0. \tag{4.24}$$

A natural way to solve eq. (4.24) numerically would be to apply fixed-point iterations as discussed in appendix F, eq. (F.12). Since, $B_{\sigma\mu} = -g_{\sigma\nu}$ is just minus the metric and hence $B_{\sigma\mu}$ is by definition invertible, we may proceed using the fixed-point iteration scheme. The fixed-point function is given by

$$F^\mu(\epsilon^\mu) = g^{\mu\sigma}A_{\sigma\rho\nu}\epsilon^\rho\epsilon^\nu + g^{\mu\sigma}C_\sigma. \tag{4.25}$$

Now let us assume that the ϵ^μ is small as it scales with the small timestep h. The fixed-point equations, eq. (4.25), then have a known solution up to first order in h:

$$F^\mu(\epsilon^\mu) = g^{\mu\sigma}C_\sigma + \mathcal{O}(h^2), \tag{4.26}$$

hence we can define ϵ_0^μ, the initial value for the fixed-point iteration:

$$\epsilon_0^\mu = g^{\mu\sigma}C_\sigma + \mathcal{O}(h^2), \tag{4.27}$$

which approximately solves eq. (4.25). As the fixed-point iteration algorithm converges we find the end result $\bar{\epsilon}^\mu$. Using eq. (4.12) we find that the new position and velocity on the manifold are given by

$$x^\mu_{i+1} = x^\mu_i + \bar{\epsilon}^\mu_i, \tag{4.28}$$

$$\dot{x}^\mu_{i+1} = \tfrac{1}{h}\bar{\epsilon}^\mu_i. \tag{4.29}$$

When $g^{\mu\nu} \to \delta^{\mu\nu}$ and therefore $\Gamma_{\mu\sigma\nu} \to 0$, we recover the symplectic Euler scheme as described in appendix K. In addition, we may modify our method a bit to solve the equations of motion for non-conservative systems. This can be done by substituting $-\partial_\sigma V_i$ by an arbitrary force F_i^μ in C_σ yielding:

$$C_\sigma^{i,i-1} = g_{\sigma\mu}^{i-1}\left(x_i^\mu - x_{i-1}^\mu\right) + \tfrac{h^2}{m}\delta_{\sigma\mu}F_i^\mu. \tag{4.30}$$

Using eq. (4.30) instead of eq. (4.22) in the fixed-point iteration scheme, eqs. (4.25) and (4.27) will produce discretized equations of motion in the presence of curvature for non-conservative systems.

4.4 Melting on curved substrates

The nature of two-dimensional crystal melting has been a controversial topic in the last decades [159]. According to Kosterlitz, Thouless, Halperin, Nelson and Young (KTHNY), a melting two-dimensional crystal first loses translational order and then orientational order at distinct temperatures. This occurs due to the emergence of topological defects in the crystal. Alternative scenarios have proposed a discontinuous melting transition mediated by the nucleation of grain boundaries. Although there is no definite consensus on the matter on *all* types of crystals, KTHNY melting transitions have been observed experimentally in colloidal systems [80, 160].

4.4.1 Topological defects in crystals

In a two-dimensional crystal there may be two types of topological defects. First, there are disclinations. Disclinations are crystal sites with an irregular coordination number, the number of bonds. An under- or over-coordinated site is irregular and breaks orientational order. These irregularities are called disclinations. For example, in a triangular lattice the regular coordination number is six — as depicted by the black sites in fig. 4.1. A disclination comes with a topological charge. The topological charge of a disclination is found by winding around it. In the example this reveals that a fivefold (blue) and a sevenfold (red) disclination have a topological charge of $j_5 = -\frac{\pi}{3}$ and $j_7 = \frac{\pi}{3}$, respectively. Secondly, there are dislocations. A dislocation is a dipole of disclinations that breaks translational order. Upon winding around a dislocation we find that it is a defect of vectorial order having both a size — the separation and charge of the dipole pair — and an orientation — the relative orientation of the dipole pair. A vector that describes a dislocation is

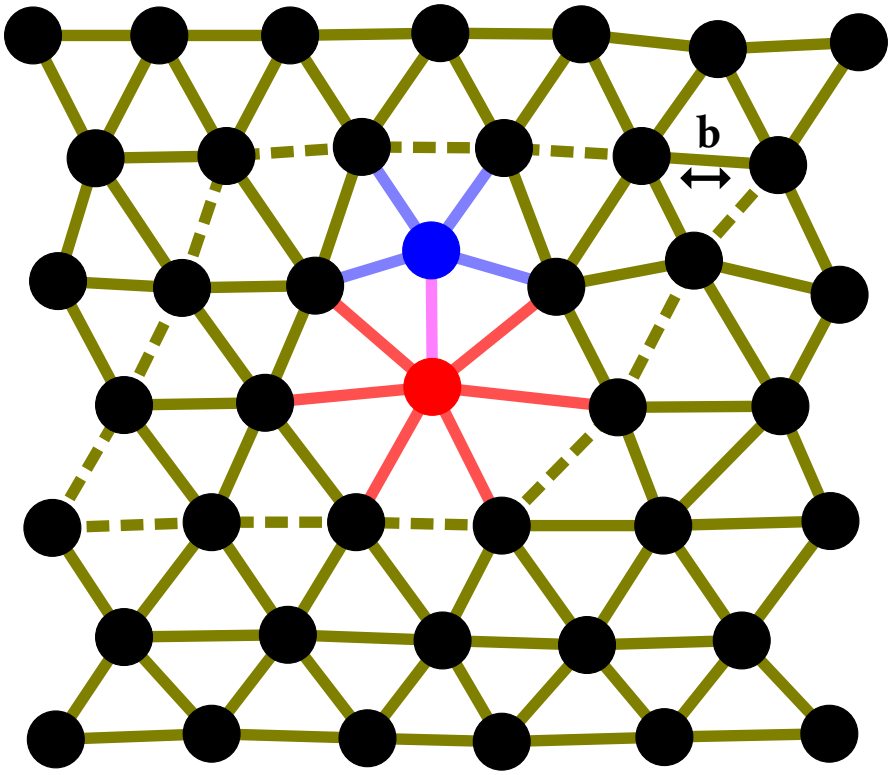

Figure 4.1: A triangular lattice with two disclinations of opposite charge tightly bound to form a dislocation. The blue point is fivefold coordinated forming a negatively charged defect. The red point is sevenfold coordinated forming a positively charge defect. The pink bond binds the two disclinations forming a dislocation. The dashed lines (olive) wind a path of three hops in every direction around the dislocation. As this path cannot close in on itself without taking *one* extra step we conclude that this defect breaks translational order as characterized by the Burgers vector $\boldsymbol{b}$. The sign of the Burgers vector is set by convention.

the Burgers vector $\boldsymbol{b}$, which is found by winding around the dislocation and finding a vector perpendicular to the dipolar separation vector. On a triangular lattice a unit sized Burgers vector $|\boldsymbol{b}| = 1$ can only have six orientations along the principal axes of the crystal. Note how a dipole of dislocations — an irregularity with two dislocations with opposite Burgers vectors right next to each other — is a neutral object as winding around such an irregularity yields no topological charge whatsoever.

4.4.2 KTHNY theory

A perfect triangular lattice at zero temperature has no defects at all. In accordance with KTHNY theory, upon increasing the temperature of such a crystal tight dipoles of dislocations emerge. Increasing the temperature even more, these dipoles of dislocations begin to unbind, breaking translational order. At this stage only translational order is broken. Orientational order, however, remains and the systems resides in the so-called *hexatic* phase. At even higher temperatures, individual dislocations unbind into two disclinations of opposite charge, breaking the residual orientational order and yielding the liquid phase. We see that the entire crystal to liquid melting transition is mediated by the emergence of topological defects.

4.4.3 Defects and curvature

Temperature is not the only reason topological defects may emerge. Stresses and strains in the system may also produce topological defects, in an attempt to screen these strains and stresses with topological charges. Likewise, in the presence of curvature, which invokes stresses and strains, topological charges arise as a screening mechanism. Positively charged disclinations are attracted to regions of positive Gaussian curvature. Similarly negatively charged disclinations are attracted to regions of negative Gaussian curvature. Dislocations reside somewhere in-between the regions of positive and negative Gaussian curvature as they can be viewed as disclination dipoles.

Analytically, the free energy of a crystal with defects in the presence of curvature according to elasticity theory is given by: [104]

$$F = \tfrac{Y}{2} \int \mathrm{d}A \int \mathrm{d}\tilde{A} \left(S(\boldsymbol{x}) - K(\boldsymbol{x})\right) \frac{1}{\Delta^2_{\boldsymbol{x}\tilde{x}}} \left(S(\tilde{\boldsymbol{x}}) - K(\tilde{\boldsymbol{x}})\right), \tag{4.31}$$

where Y is the Young modulus, S is the distribution of unbound topological defects, K is Gaussian curvature and Δ^2 the biharmonic operator. The free energy in terms of the Airy stress function χ is given by:

$$F = \tfrac{1}{2Y} \int \mathrm{d}A (\Delta\chi(\boldsymbol{x}))^2. \tag{4.32}$$

Combining eqs. (4.31) and (4.32) we find the following differential equation:

$$\Delta^2\chi(\boldsymbol{x}) = Y\left(S(\boldsymbol{x}) - K(\boldsymbol{x})\right). \tag{4.33}$$

In the absence of defects the latter becomes

$$\Delta^2\chi(\boldsymbol{x}) = -YK(\boldsymbol{x}), \tag{4.34}$$

yielding an equation that describes the Airy stress function in terms of curvature only. From the Airy stress function we may obtain the geometric potential for dislocations D given by: [104]

$$D(\boldsymbol{x}, \boldsymbol{b}_i) = \boldsymbol{b}_i \epsilon_{ij} \nabla_j \chi(\boldsymbol{x}). \tag{4.35}$$

At zero temperature, dislocations will distribute in regions where they minimize the elastic energy in accordance to the dislocation potential in eq. (4.35).

4.4.4 Dislocation dynamics

As a dislocation terminates a row of sites in a crystal, it is energetically more favorable to nucleate dislocations in tight pairs. Dislocations can easily move around parallel to the Burgers vector orientation. This motion is called *glide*. When a dislocation moves in any other direction that is not parallel to the Burgers vector the motion is called *climb* and generally costs much more energy due to the required diffusive mechanisms. The dislocation pair hence separates by having both of its dislocations glide away from each other. Nucleating a dislocation, and therefore also a dislocation pair, costs energy. The energy per nucleated dislocation is called the core energy E_c.

Dislocations interact with other dislocations. The pairwise dislocation–dislocation potential takes the following form:

$$V_{\mathrm{dd}}(\boldsymbol{b}_i, \boldsymbol{b}_j) = \tfrac{Y}{4\pi} \left(\boldsymbol{b}_i \boldsymbol{b}_j \log\left(\frac{\boldsymbol{r}_{ij}}{a}\right) + \frac{(\boldsymbol{b}_i \boldsymbol{r}_{ij})(\boldsymbol{b}_j \boldsymbol{r}_{ij})}{\boldsymbol{r}_{ij}^2} \right), \tag{4.36}$$

where $\boldsymbol{r}_{ij}$ is the distance between the two dislocations with Burgers vectors $\boldsymbol{b}_i$ and $\boldsymbol{b}_j$ and a is the lattice spacing of the crystal [42]. Additionally, two dislocations of opposite orientation may glide back into each other and annihilate — this is the opposite process of dislocation nucleation. Likewise, two dislocations with different but not equal or opposite orientations may glide into each other and annihilate, resulting in one new dislocation with an intermediate orientation, but equal topological charge. Conversely the reverse process may also occur. For instance on the triangular lattice, the dislocation b_θ and $b_{\theta+\frac{2\pi}{3}}$ may add up to one single dislocation $b_{\theta+\frac{\pi}{3}}$.

In the presence of curvature, dislocation pairs may nucleate in regions where the nucleation energy is sufficiently small. In general, the regions of preferred dislocation pair nucleation are not solely determined by the geometric potential in eq. (4.35). Dynamic constraints play a role as well. The system can only minimize energy through a series of moves consisting of coordinated glide, nucleation and annihilation reactions. As some operations seem entropically hard to reverse, the system may become arrested in some local minimum. In addition, the geometric potential may make dislocation glide energetically costly, as it leaves a local minimum.

4.4.5 Melting on curved substrates

An effective Hamiltonian for dislocations in a curved crystal is:

$$H_{\text{disl}}(\boldsymbol{x}) = NE_c + \sum_i^N D(\boldsymbol{x}, \boldsymbol{b}_i) + \sum_{i>j}^N V_{\text{dd}}(\boldsymbol{b}_i, \boldsymbol{b}_j), \tag{4.37}$$

where N is the number of dislocations in the system. When generating equilibrium states from this Hamiltonian however, one should consider that some states may not be accessed due to dislocation dynamics. For instance, the lowest energy configuration of a curved crystal with one dislocation is found when the dislocation resides in the minimum of the dislocation potential eq. (4.35). This state might never occur, however, if dislocation pairs are nucleated in on the wrong row, as dislocations are only allowed to glide. At this point, it is obvious to expect dislocations and also disclinations to have spatial preferences, depending on the curvature. Therefore, a crystal in the presence of curvature may melt inhomogeneously allowing crystal, hexatic and liquid phases to simultaneously exist at different locations of the sample.

It is, however, hard to establish if the dislocation density $\sigma_{\text{disl}}(\boldsymbol{x})$ is purely dominated by energetics and thus follows from

$$\sigma_{\text{disl}}(\boldsymbol{x}) \propto e^{-\beta H_{\text{disl}}(\boldsymbol{x})}, \tag{4.38}$$

or whether it is determined primarily by dislocation-dynamic effects.

4.4.6 Computational studies of melting and curvature

Monte Carlo simulations have studied the distribution of dislocations in the presence of curvature at zero temperature [99]. Although the Monte Carlo method should also work at finite temperature, curved space melting was never thoroughly investigated because the algorithm gets slower as temperatures increase. An alternative candidate method would be molecular dynamics.♠ Molecular dynamics is a numerical method that solves Newton's equations of motion for many interacting particles — the so-called generalized N-body problem. Here we will solve Newton's equations of motion for many interacting particles in the presence of curvature. The integration scheme to solve Newton's equations in the presence of curvature — which is the main subject of this chapter — is discussed in section 4.3. Apart from the integration method; the choice of curvature, boundary and initial conditions and ensemble preparations are important. We choose the surface to be of a form represented by the two-dimensional Monge patch, see appendix E. A Monge patch, defines a curved surface by introducing a scalar function $f : \mathbb{R}^2 \to \mathbb{R}$ called the Monge function which is embedded in a three-dimensional space $\mathbb{R}^3$. We will simulate for the following Monge functions:

$$f_{\text{bump}}(x, y) = Ae^{-K\left(x^2+y^2\right)}, \tag{4.39}$$

$$f_{\text{egg}}(x, y) = A\cos(K_x x)\cos(K_y y), \tag{4.40}$$

which we will refer to as the Gaussian bump eq. (4.39) and egg carton eq. (4.40), respectively. Here, for both Monge functions, A is the amplitude. K is the width of the Gaussian bump and $\{K_x, K_y\}$ set the periodicities of the egg carton surface. We will choose an $L_x \times L_y$ with $L_x \approx L_y$ nearly square simulation box with the origin in the middle and with periodic boundary conditions. In order to ensure periodicity in the Monge functions, we apply the constraints $K^{-1} \ll L^2$ and $K_x = \frac{2\pi}{L}n$ and $K_y = \frac{2\pi}{L}m$ with $n, m \in \mathbb{N}$. We initialize $N \in \mathbb{N}$ particles in a triangular lattice with lattice spacing a.♡

♠ Molecular dynamics is introduced in appendix O.

♡ For a possible algorithm to generate a triangular lattice see appendix section Q.2.

N	q_x	q_y
780	26	15
5822	71	41
10864	97	56
17466	123	71
32592	168	97
43456	194	112
65964	239	138
81090	265	153
97776	291	168
130368	336	194
151316	362	209
173824	388	224
216500	433	250
243270	459	265
271600	485	280

N	q_x	q_y
293328	504	291
324360	530	306
356952	556	321
417094	601	347
453948	627	362
492362	653	377
562588	698	403
605264	724	418
649500	750	433
729810	795	459
778308	821	474
828366	847	489
866000	866	500
918760	892	515
973080	918	530

Table 4.1: An incomplete list of special numbers up to a million that generate a triangular lattice in an approximate square. N is the number of particles, q_x and q_y are the number of unit cells in the x and y direction respectively. The tolerance on q_x and q_y is at most 0.01.

We are trying to prepare a triangular lattice with N particles inside a square box with periodic boundary conditions. In order to tile the square box with $q_x \times q_y$ tiles we require[♠]

$$N = 2q_x q_y = \frac{2L^2}{\sqrt{3}\,a}. \tag{4.41}$$

As eq. (4.41) has to be satisfied we have to find the special numbers that approximately fit; some of these numbers are listed in table 4.1. The procedure is depicted in fig. 4.2. The velocity of the particles is randomly assigned according to the generalized equipartition theorem, respecting the curvature. This can be done as follows. The equipartition theorem states:

$$\langle x^\mu \partial_\nu H_{\text{kin}} \rangle = \delta^\mu_\nu k_B T. \tag{4.42}$$

[♠] Tiles stack in integer values, hence: $q_x, q_y \in \mathbb{N}$.

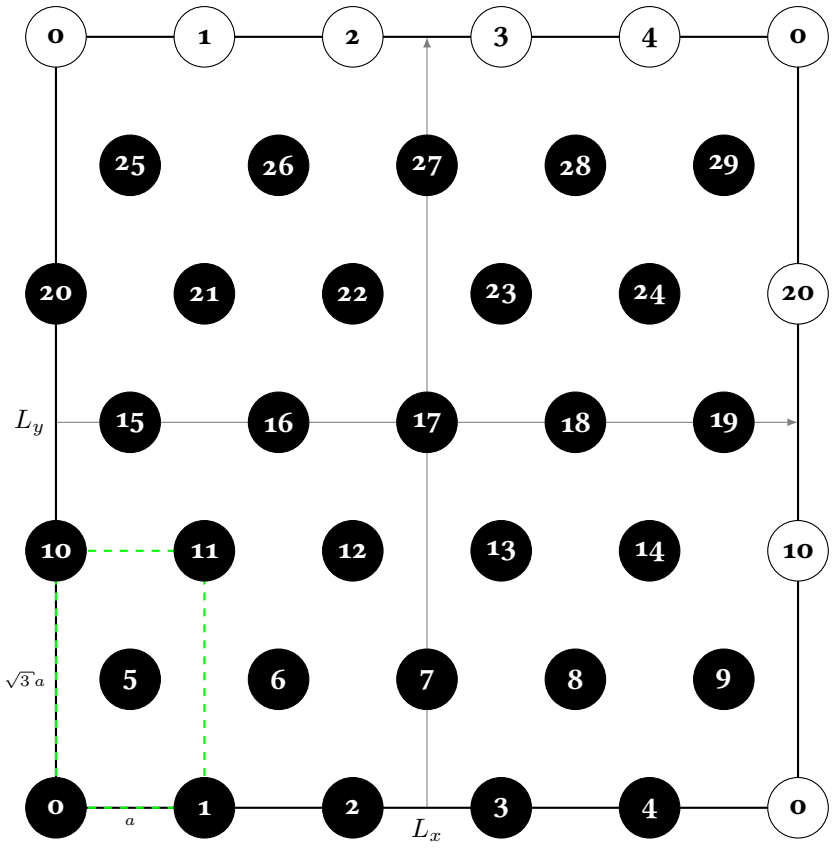

Figure 4.2: Depiction of $N = 30$ black particles in a triangular lattice within the simulation box of $L_x \times L_y$ ($q_x = 5$ and $q_y = 3$). Particle seventeen lies in the origin of the chosen coordinate system. The white particles are image particles present because of periodic boundary conditions. The black lines are the boundaries of the system. The gray lines are the base-axes. The green dashed lines depict the unit cell containing two particles, in this case, once particle five and a quarter times particles zero, two, ten and eleven.

In this case, the kinetic part of the Hamiltonian is given by:

$$H_{\text{kin}} = \tfrac{1}{2} m g_{\mu\nu} \dot{x}^\mu \dot{x}^\nu. \tag{4.43}$$

By using eqs. (4.42) and (4.43) the following equality is found:

$$\langle g_{\mu\nu} \dot{x}^\mu \dot{x}^\nu \rangle = g_{xx} \langle \dot{x}^2 \rangle + g_{yy} \langle \dot{y}^2 \rangle + 2 g_{xy} \langle \dot{x}\dot{y} \rangle = \tfrac{2 k_B T}{m} \tag{4.44}$$

If the problem is diagonalized in the eigenbasis of the metric $g_{\mu\nu}$ this equation simplifies to:

$$\langle \dot{a}^2 \rangle + g \langle \dot{b}^2 \rangle = \tfrac{2 k_B T}{m} \tag{4.45}$$

Where $\dot{a}$ and $\dot{b}$ are eigencoordinates of $g_{\mu\nu}$. Using Maxwell–Boltzmann statistics the variances of the velocity in the $\dot{a}$ and $\dot{b}$ direction are given by:

$$\mathrm{e}^{-\frac{H_{\text{kin}}}{k_B T}} = \mathrm{e}^{-\frac{m(\dot{a}^2 + g\dot{b}^2)}{2 k_B T}} = \mathrm{e}^{-\frac{\dot{a}^2}{2\sigma_{\dot{a}}^2}} \mathrm{e}^{-\frac{\dot{b}^2}{2\sigma_{\dot{b}}^2}}, \tag{4.46}$$

and therefore:

$$\sigma_{\dot{a}}^2 = \tfrac{k_B T}{m}, \qquad \sigma_{\dot{b}}^2 = \tfrac{k_B T}{g m}. \tag{4.47}$$

From the variances and initial particle positions,[♠] random initial velocities corresponding with a certain (fixed) temperature can be found by generating two random numbers from a normal distribution[♡] and multiplying them with their desired variances. The mean of the velocity distribution is zero, since the system is desired to be without flow. Finally, the random numbers need to be transformed back from the eigenbasis of $g_{\mu\nu}$ to the original basis, which is done by a simple base transformation.

Note that the initial conditions chosen for the simulations are not ideal, since the simulation is not started in the ground state of the system, because a flat space triangular lattice is *not* the ground state in curved space. Unfortunately, finding the real curved space ground state is a very hard generalized Thomson-like problem which currently remains unsolved [124, 173]. Therefore the lower limit of the energy in the system is not only controlled by the temperature, but also by the curvature. One way to resolve this issue by minimizing geometric frustration is called quenching: the idea is to run a

[♠] The metric determinant $g = g(x^\rho)$ is position-dependent.

[♡] A uniform random generator can be transformed into a normally distributed random generator by using, for instance, a Box–Muller transformation.

molecular dynamics simulation while occasionally resetting the kinetic energy to zero. The most effective timing to set the kinetic energy to zero is when the kinetic energy is at its maximum and the potential energy is therefore minimal, assuming constant total energy, because the potential energy must be minimized to obtain a local ground state.

The described scheme will simulate particles in the microcanonical ensemble. To obtain a canonical ensemble a linear damping term and a Langevin random force term are introduced — this is the so-called Langevin thermostat.

4.4.7 Preliminary results

Using the procedure as described in section 4.4.6 we prepare our molecular dynamics simulations in the microcanonical ensemble. Let us first analyze the results of such simulations on a Gaussian bump surface, see eq. (4.39). Upon performing one simulation for $N = 17466$ particles in a box with the approximate dimensions $L \times L$ for a small finite temperature — after relaxation[♠] — we typically find a simulation snapshot as depicted fig. 4.3. We observe that the individual dislocations are oriented with their Burgers vectors perpendicular to the radial direction with respect to the top of the bump; fivefold disclinations (blue) facing towards the top and sevenfold disclinations (red) facing away from the bump. The dislocation distribution at low density for a Gaussian bump is found using eq. (4.38) neglecting dislocation–dislocation interactions given by eq. (4.36) in the effective Hamiltonian eq. (4.37). We obtain

$$\sigma_6(x^\rho) \propto \mathrm{e}^{-\beta \min_{\theta\in[0,2\pi]} D(x^\rho, \mathbf{b}(\theta))}, \tag{4.48}$$

where θ is the orientation of the Burgers vector. Hence, we find that $\mathbf{b}(\theta)$ is always perpendicular to the radial direction. The theoretical dislocation density for a Gaussian bump found by using eq. (4.48) is plotted in fig. 4.4.[♡] Upon doing numerous simulations with different random instances of the same initial conditions we can generate a dislocation density profile for the simulations and compare it to this simple estimate. This is done in fig. 4.5,

[♠] Meaning the initial condition is first quenched to zero temperature after which the temperature is reinitialized.

[♡] Henceforth, all the density plots — which we assume for the sake of argument to be normalized — will use the widely known jet color map with zero value as dark blue and unit value as dark red.

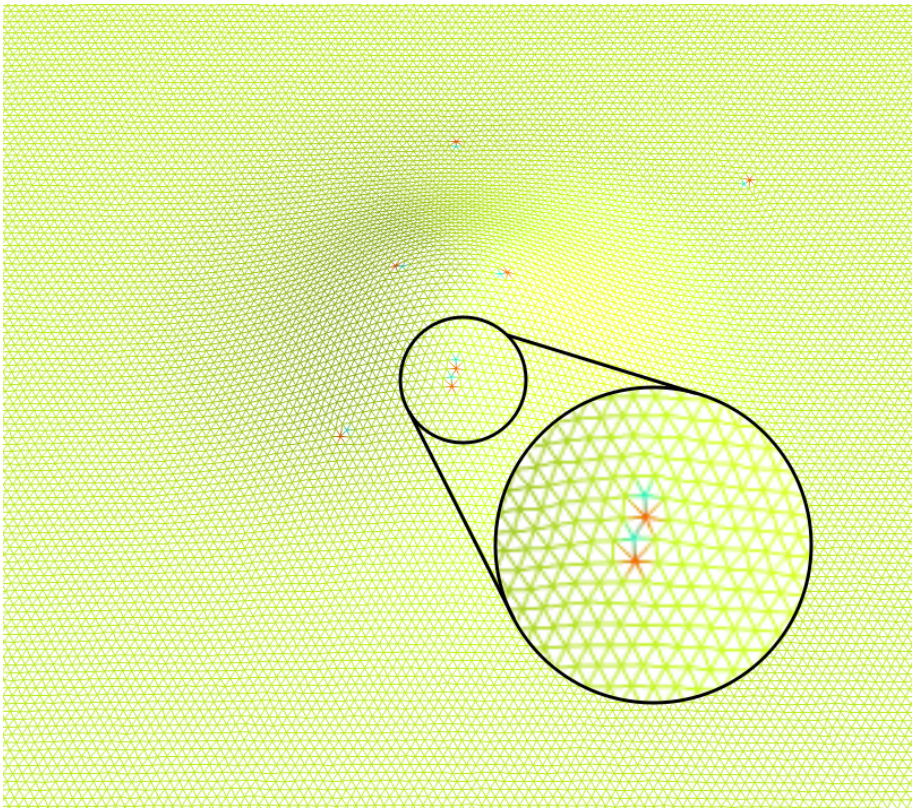

Figure 4.3: A typical end result of a simulation with $N = 17466$ particles. The triangulation is done with Delaunay triangulation. Yellow particles have six neighbors. Red particles have seven neighbors and blue particles have five neighbors. Note how dislocations are oriented with respect to the bump. This simulation is done at $\frac{A}{L} = 0.125$ and $KL = 5\sqrt{5}$, for 10000 time steps. The temperature is initialized at $T = 0.0022$ (a.u.). This image was cropped to fit this thesis.

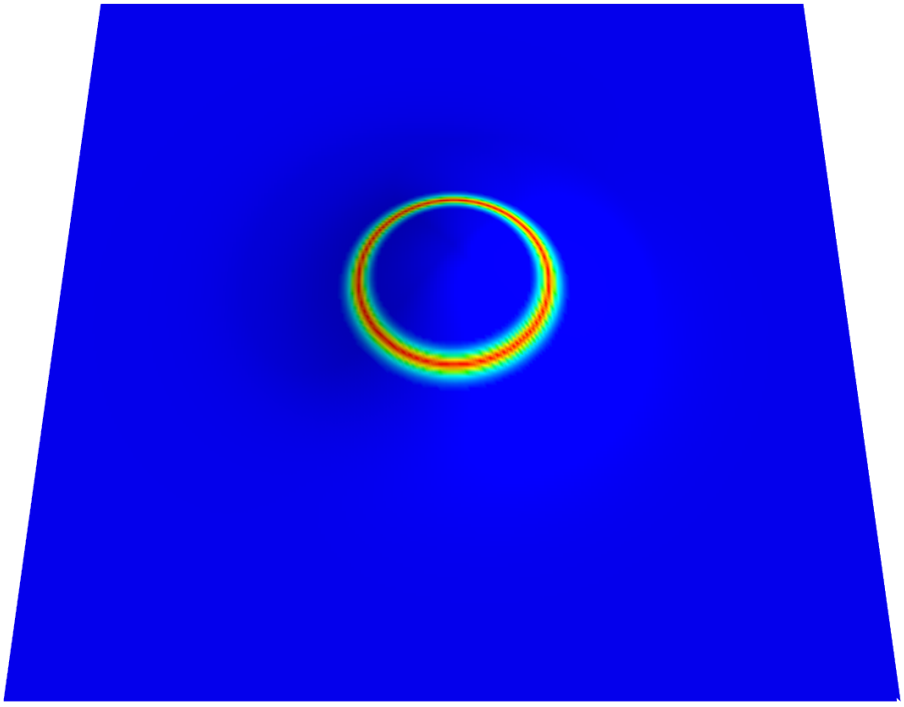

Figure 4.4: The theoretical density of dislocations according to eq. (4.48) for a Gaussian bump with $\frac{A}{L} = 0.125$ and $KL = 5\sqrt{5}$. The color map is given on page 92 footnote ♡.

and we find some discrepancies with the theoretical result plotted in fig. 4.4. Firstly, we observe a sixfold symmetry in fig. 4.5. This sixfold symmetry is due to the discrete nature of the Burgers vector as set by the lattice, which can be highlighted by distinguishing the six distinct dislocations. We color code the dislocations with the key given in fig. 4.6 on page 101 to find fig. 4.7. To account for this effect, we may modify the dislocation density eq. (4.48) to respect the discrete nature of the Burgers vector. This is done by minimizing the dislocation potential $D(x^\rho, \mathbf{b}(\theta))$ where θ is now discrete and set by the principal axes of the crystal. Doing so results in:

$$\sigma_6(x^\rho) \propto \mathrm{e}^{-\beta \min_{\mathbf{b}_n} D(x^\rho, \mathbf{b}_n)}, \tag{4.49}$$

where $\mathbf{b}_n$ are the discrete Burgers vectors. The modified dislocation density eq. (4.49) is plotted in fig. 4.8. Secondly, we observe dislocations far away from the bump which can be explained by realizing that dislocations nucleate in pairs and then glide to their equilibrium position. For one dislocation this means migrating to the point close to the theoretical energetic minimum, for its opposite pair this means migrating away from the bump to infinity. Since periodic boundary conditions are imposed, however, these dislocations have no way of reaching infinity and migrate to a point that minimizes their energy while respecting the constricted one-dimensional glide motion. This effect can be observed when we tile fig. 4.7 resulting in fig. 4.9. Finally, we observe that the peaks at the theoretical minima split. This phenomenon can be explained by dislocation–dislocation interactions and dislocation dynamics, see eq. (4.36) and section 4.4.4 respectively. Two dislocations may glide into each other and change their orientation if compatible; the reverse is also possible. For example two dislocations of opposite orientation can annihilate but can be spontaneously created. Likewise two dislocations with an orientational difference of $\frac{2\pi}{3}$ may form one dislocation with a mean angle. The latter is responsible for the peak splitting. Using the color coding as given in fig. 4.6 we observe that dislocation of e.g. cyan orientation at their equilibrium position occasionally split up in to two dislocations with green and blue orientation. This newly formed dislocation will then glide to to its new respective minimum. Since gliding motion is strictly one-dimensional these new minima are farther radially inward than the energetic minima described by the modified dislocation potential as plotted in fig. 4.8. The described mechanism is depicted in fig. 4.10.

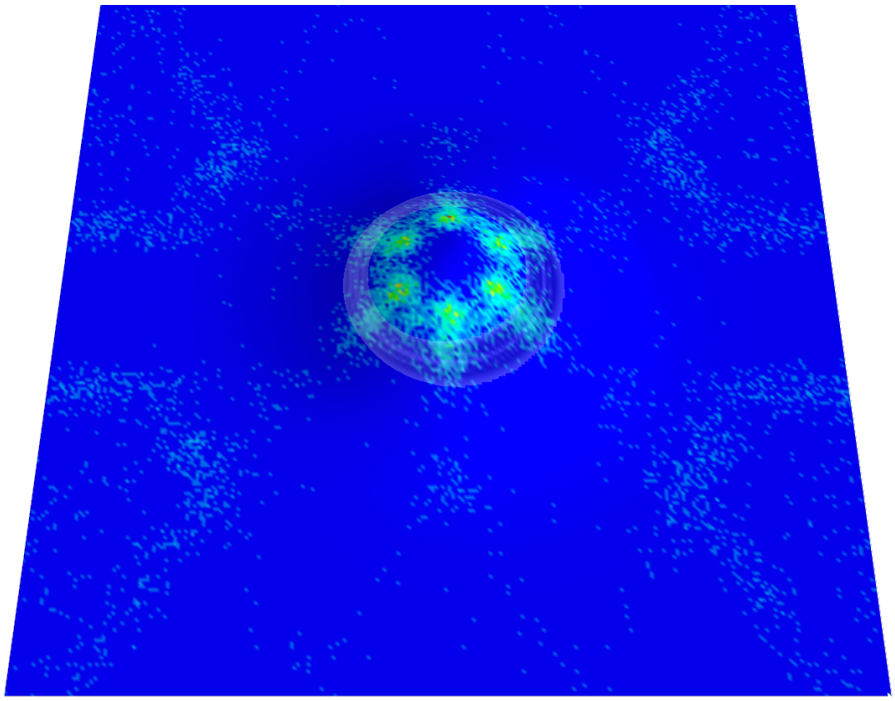

Figure 4.5: The simulated dislocation density on a Gaussian bump. The dark bands indicate the theoretically predicted minima. This plot was compiled from 1200 simulations done at $\frac{A}{L} = 0.125$ and $KL = 5\sqrt{5}$, for 10000 time steps. The temperature is initialized at $T = 0.0022$ (a.u.). The color map is given on page 92 footnote ♡.

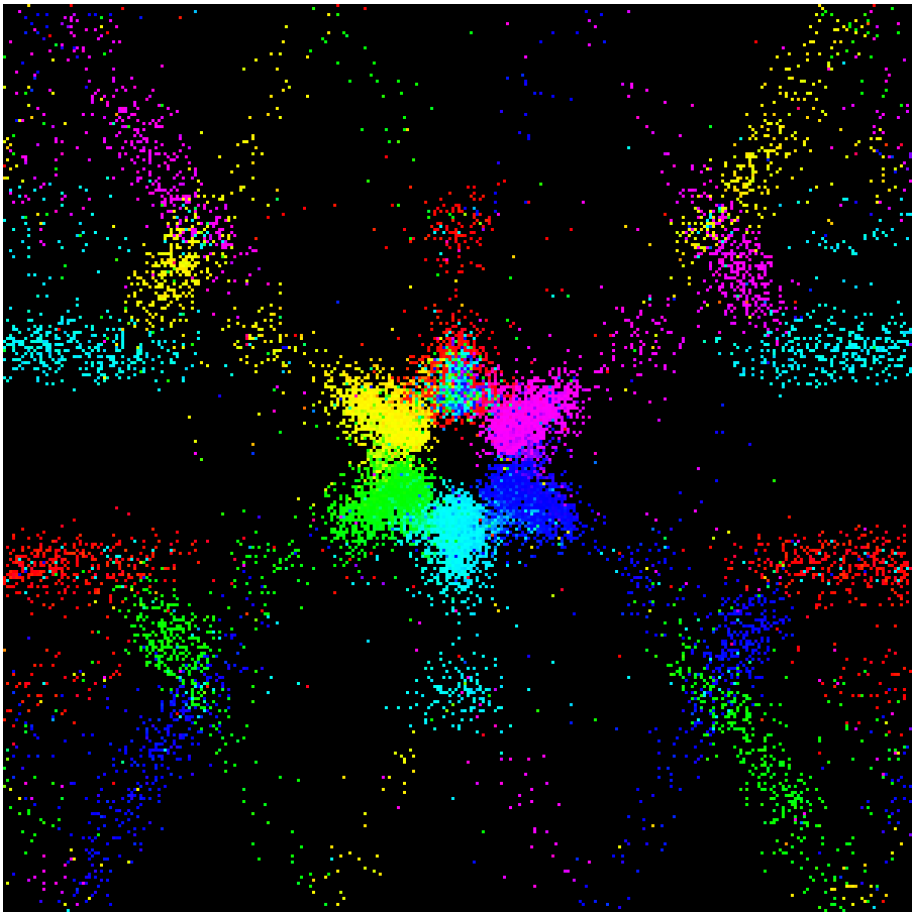

Figure 4.7: The simulated dislocation density as depicted in fig. 4.5 color coded as defined by fig. 4.6 on page 101. We observe that the color coded dislocations align as expected by energy minimization done by eq. (4.49). The occurrence of cyan in the red minimum is due to the branch cut in the $\arctan_2$ function.

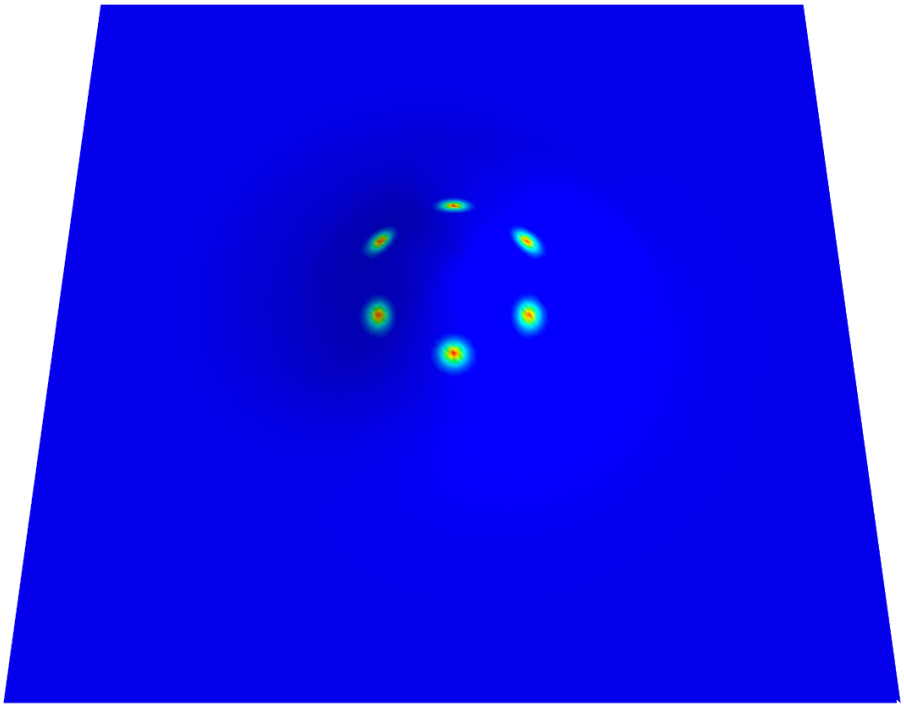

Figure 4.8: The modified theoretical density of dislocations according to eq. (4.49) for a Gaussian bump with $\frac{A}{L} = 0.125$ and $KL = 5\sqrt{5}$. The color map is given on page 92 footnote ♡.

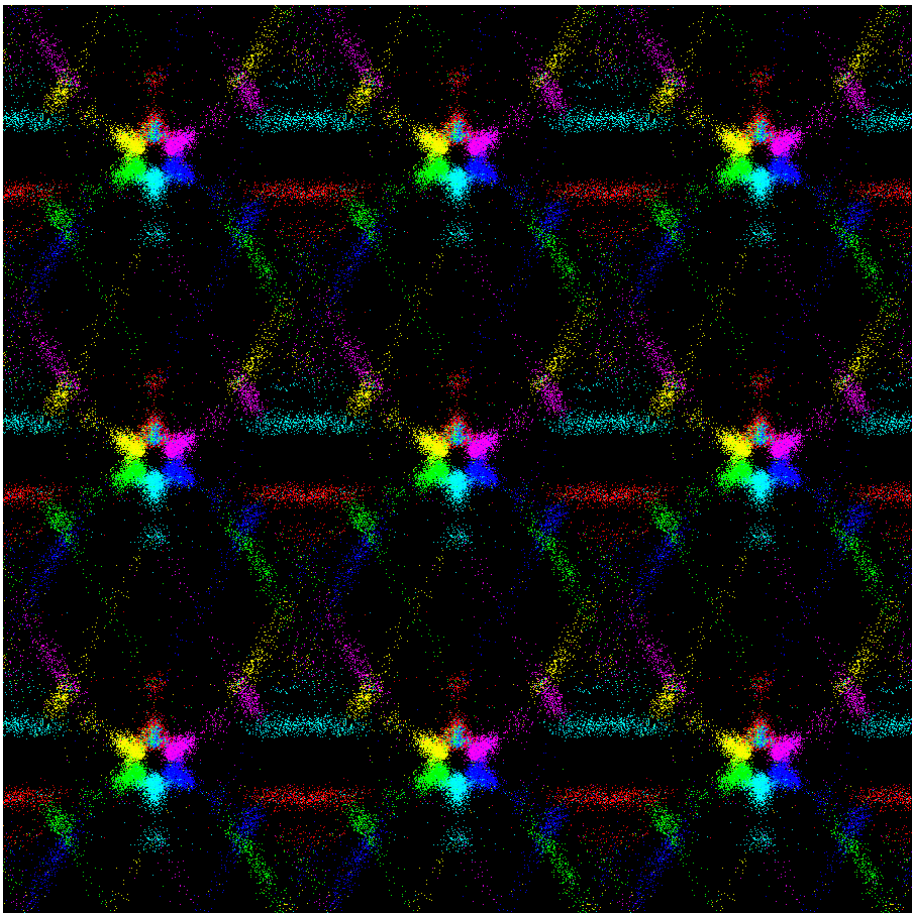

Figure 4.9: A 3×3 tiling of fig. 4.7. We observe that the color coded dislocations align as expected by energy minimization done by eq. (4.49). Additionally, we observe that an important number of dislocations do not fit in this sixfold pattern. They glide away from their nucleation point towards a lower energetic point. The red and cyan dislocation are trapped between the opposite minima, the blue, magenta, yellow and green dislocations are free to roam around (one-dimensionally) forming a long tail.

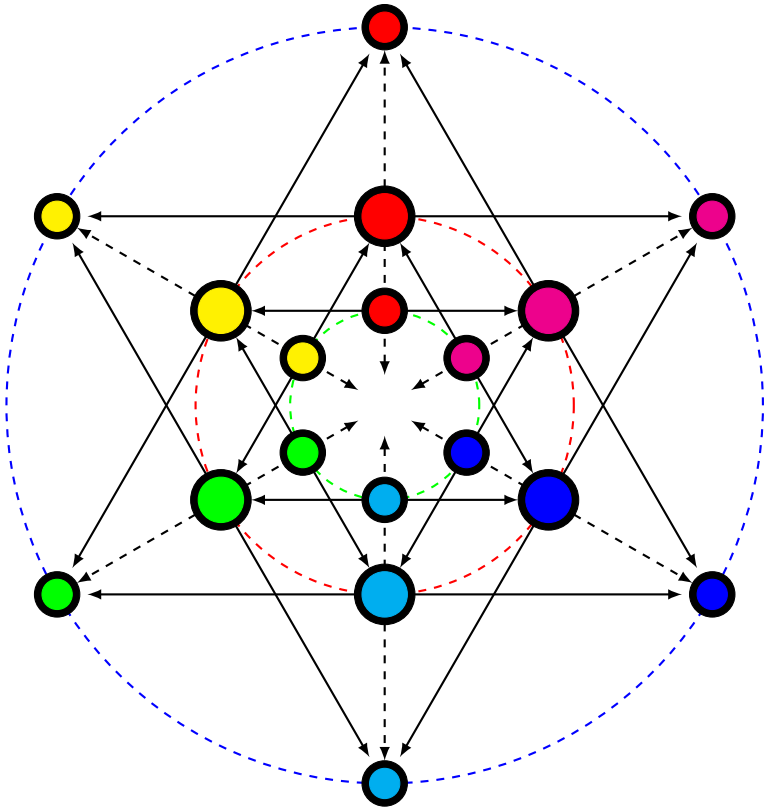

Figure 4.10: The depiction of the mechanism by which the energetic minimum is split. The large colored nodes are the predicted dislocation potential minima. The smaller and inner colored nodes are the minima by the dislocation splitting and gliding. The solid arrows are glide directions for their respective node, the dashed arrows are the climb directions. A dislocation that for instance resides at the red node and then splits into two dislocations with their Burgers vectors rotated by $\frac{\pi}{3}$ compared to the initial dislocation will glide towards their new inner minima. The dislocation cannot climb because this requires diffusive mechanisms, and is therefore stuck in its new minimum.

A similar analysis can be conducted on the egg carton surface, see eq. (4.40). Theoretically, the dislocation density for the egg carton surface is plotted fig. 4.11. The dislocation density of the simulations are found in fig. 4.12. As this structure is periodic, the periodic boundary conditions interfere less with the dislocation distribution. The theoretical dislocation density does not account, however, for dislocation–dislocation interactions, which is likely the reason why the minima in the simulations differ a little from the theoretical estimate.

4.4.8 Conclusions and outlook

It is hard to draw any firm conclusions. It seems, however, that for low temperatures, the simulations theoretical estimates and numerical experiment are in qualitative agreement, although more investigation is required. A thorough test would be to compare the results of the dynamics to a Monte Carlo simulation. Such Monte Carlo simulations would simulate dislocation dynamics in the presence of curvature similar to Pafka et al. [140] and Saito [165] using the Hamiltonian stated in eq. (4.37) — without neglecting the dislocation–dislocation potential eq. (4.36). If the Monte Carlo simulations match the molecular dynamics simulations we will understand the behavior of multiple dislocations in the presence of curvature. The results might differ because curvature influences the dislocation–dislocation interaction. One could measure the dislocation–dislocation interaction from the simulations and plug them back into the Monte Carlo, see also Crocker et al. [150].♠

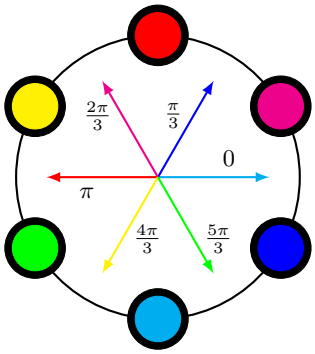

Figure 4.6: The arrows color coding the six distinct orientations of the Burgers vectors as imposed by the six principle lattice directions. The colored circles schematically indicate the spatial positions of distinct minima per orientation of the Burgers as found by eq. (4.49).

♠See the forthcoming doctorate thesis of C. van der Wel (Leiden University) for a generalization of Crocker et al. [150] in the presence of curvature.

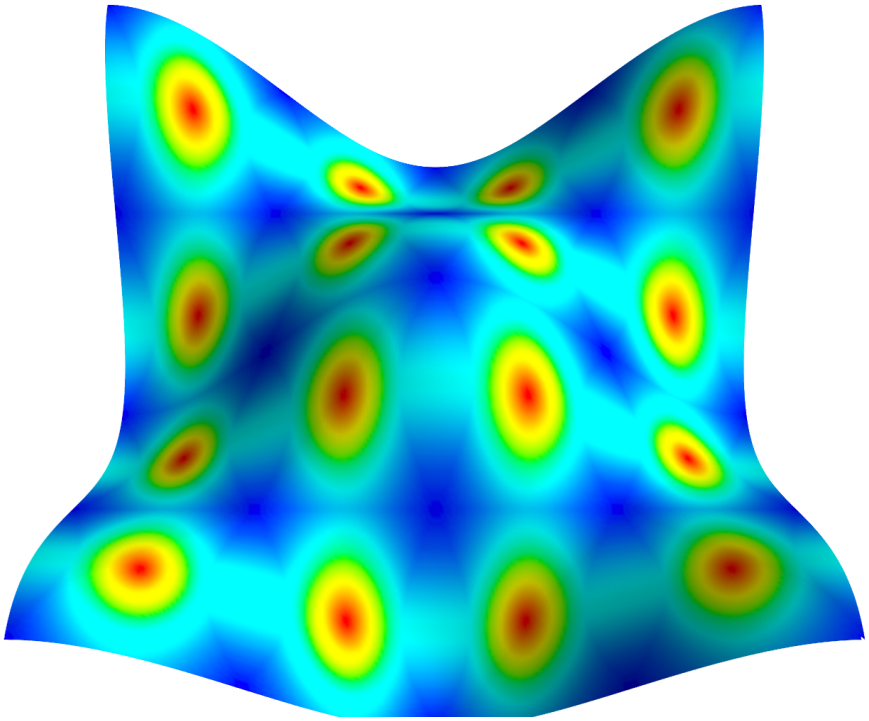

Figure 4.11: The theoretical density of dislocations according to eq. (4.38) for a egg carton surface with $K_x L = K_y L = 2\pi$. The color map is given on page 92 footnote ♡.

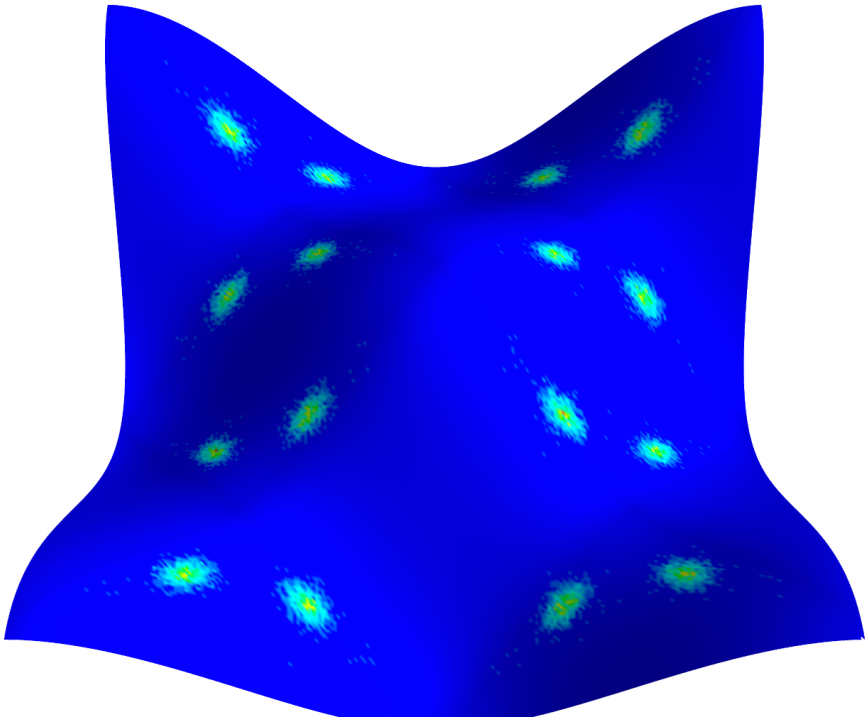

Figure 4.12: The simulated dislocation density on a egg carton surface. This plot was compiled from 1200 simulations done at $\frac{A}{L} = 0.1$ and $K_x L = K_y L = 2\pi$, for 10000 time steps. The temperature is initialized at $T = 0.001$ (a.u.). The color map is given on page 92 footnote ♡.

Appendices

Appendix A Newton's laws of motion

In the seventeenth century Sir Isaac Newton published his famous work the *Philosophiæ Naturalis Principia Mathematica*♠ which laid the foundations of modern-day physics [106]. One of the most notable parts of the good book are the so-called *Newton's laws of motion*. Newton's laws of motion describe *any* classical system. Classical mechanics was born.

Newton's first law of motion is a steady-state condition. It states in layman terms that if a body is moving at a zero or constant velocity there are no net forces acting on that body. To quote:

> "*Every body perseveres in its state of rest, or of uniform motion in a right line, unless it is compelled to change that state by forces impressed thereon.*"

Which can be mathematically stated as:

$$\ddot{x}^{\mu} = 0 \quad \text{if and only if} \quad \sum_{i} F_i^{\mu} = 0. \tag{A.1}$$

Newton's second law of motion is a formulation of a differential equation. In layman terms it states that the acceleration of a body is proportional to the net forces on that body. Quote:

> "*The alteration of motion is ever proportional to the motive force impressed; and is made in the direction of the right line in which that force is impressed.*"

♠The original *Philosophiæ Naturalis Principia Mathematica* is written in Neo-Latin. The English translations cited here are found in Newton [168].

Or mathematically:

$$F^\mu = m\ddot{x}^\mu. \tag{A.2}$$

Equation (A.2) is colloquially called Newton's equations or Newton's equations of motion.

Finally, Newton's third law of motion tells us something about how bodies interact. In layman terms, if one body applies a force to another body, the other body will apply an equal and opposite force on the initial body. More colloquially: "action is reaction". To quote:

> *"To every action there is always opposed an equal reaction: or the mutual actions of two bodies upon each other are always equal, and directed to contrary parts."*

Mathematically stated as:

$$F_1^\mu = -F_2^\mu. \tag{A.3}$$

Appendix B The concept of energy

A useful concept in physics is the concept of energy. Energy is the ability to do work. Work is done when a force applied to a body changes the body's velocity. In classical mechanics there are two forms of energy. Firstly, there is the measure of energy due to velocity, which is called the kinetic energy $T(\dot{x}^\mu)$ and is defined as such:

$$T(\dot{x}^\mu) = \tfrac{1}{2}m\dot{x}^2. \tag{B.1}$$

Kinetic energy is basically the work needed to accelerate a body from zero motion to a given velocity. Secondly, there is a measure of energy due to position, which is called the potential energy[♠] $V(x^\mu)$ and typically depends on the interactions in a system. Colloquially, the potential energy can be described as the work that is needed for a body to obtain a certain position. Whatever the potential may be, the force generated due potential on the body is given by:

$$F^\mu\left(x^\rho\right) = -\delta^{\mu\nu}\partial_\nu V\left(x^\rho\right). \tag{B.2}$$

[♠] Sometimes referred to as just the *potential*.

Note that both kinetic and potential energy are defined per body. A system composed of multiple bodies has a total kinetic and potential energy given respectively by the sum of kinetic and potential energy of its individual bodies.

A useful concept to mention is that the sum of the total kinetic and potential energy of a system — often called the Hamiltonian or total energy and is denoted as $H = T + V$ — is always conserved if the system does not interact with another system. Mathematically, this can be shown by taking the time derivative of the Hamiltonian:

$$\frac{\mathrm{d}H}{\mathrm{d}t} = \frac{\mathrm{d}T}{\mathrm{d}t} + \frac{\mathrm{d}V}{\mathrm{d}t} = \dot{x}\left(m\ddot{x}^{\mu} + \delta^{\mu\nu}\partial_{\nu}V(x^{\rho})\right) = 0, \tag{B.3}$$

because we know from eqs. (B.2) and (A.2) that:

$$m\ddot{x}^{\mu} = -\delta^{\mu\nu}\partial_{\nu}V(x^{\rho}), \tag{B.4}$$

if and only if no non-conservative or external forces are present in the system. This means that the velocities in such a system increase if and only if the potential energy decreases. To change the value of the Hamiltonian for a system — in time — energy needs to be transfered from the system in question to another system.

Appendix C The stationary action principle

A century after Newton postulated his laws of motion, giving birth to classical mechanics, Joseph-Louis Lagrange reformulated classical mechanics for conservative systems. His reformulation is now often refered to *Lagrangian Mechanics*. Lagrange's reformulation is an example of a principle which is now know as the *least action principle* or more correctly *the stationary action principle*. We should stress that the stationary action principle is so powerful that it generates most of the equations in modern day advanced physics.

In order to explain the principle of stationary action we first have to define the action. The action is a functional♠ that takes any path the system can take. We will just impose that for the classical case the action $\mathcal{S}$ is defined by:

$$S(x^{\mu}) = \int_{t_i}^{t_f} L(x^{\mu}, \dot{x}^{\mu}, t)\mathrm{d}t, \tag{C.1}$$

♠Colloquially: a function of functions.

where L is called the *Lagrangian*. The principle of stationary actions then postulates that the equations of motion are found by finding the stationary points of the action. Mathematically, this is done by taking a functional derivative:

$$\delta \mathcal{S} = 0 \tag{C.2}$$

The stationary points of the action are found — or eq. (C.2) is satisfied — by applying the famous Euler–Lagrange equations:

$$\frac{\partial L}{\partial x^\mu} - \frac{\mathrm{d}}{\mathrm{d}t}\frac{\partial L}{\partial \dot{x}^\mu} = 0 \tag{C.3}$$

The Lagrangian L — implicitly defined in eq. (C.1) — depends on the physical problem. For conservative classical systems it turns out that the Lagrangian is always the difference between kinetic and potential energy:

$$L = T - V. \tag{C.4}$$

It is worth stating that the Lagrangian is coordinate-independent — it works in all coordinate systems — as it purely described by energetics which are coordinate-independent.

To summarize, applying the Euler–Lagrange to the classical Lagrangian will yield Newton's equations of motion for the particular problem. In the most general conservative classical case $L = \frac{1}{2}m\dot{x}^2 - V$, the Euler–Lagrange will yield:

$$m\ddot{x}^\mu = -\delta^{\mu\nu}\partial_\nu V. \tag{C.5}$$

Equation (C.5) is Newton's equation eq. (B.2) where all the forces are due to a potential — and thus conservative by definition — which can also be found by combining eqs. (A.2) and (B.2).

Appendix D Geodesic equation

In flat space♠ the *shortest* distance between two points, a^μ and b^μ, is known to be a straight line with a length found using the Pythagorean theorem:

$$s^2 = \delta_{\mu\nu}(b-a)^\mu(b-a)^\nu. \tag{D.1}$$

♠By flat space we mean space without curvature.

Another, more complicated way to find this path is done by integrating infinitesimal parts of it:

$$s^2 = \int_0^1 \delta_{\mu\nu} \dot{x}^\mu \dot{x}^\nu \mathrm{d}t, \tag{D.2}$$

where $x^\mu(t)$ is then given by:

$$x^\mu(t) = a^\mu + (b-a)^\mu t, \tag{D.3}$$

such that $x^\mu(0) = a^\mu$ and $x^\mu(1) = b^\mu$. The a priori unobvious benefit of writing it this way is that even though if we didn't know the path $x^\mu(t)$, it can always be found by minimizing the integral in eq. (D.2). We can minimize by using the Euler–Lagrange equations given in eq. (C.3) as we have previously done to find the stationary action in appendix C. The Euler–Lagrange equations will yield some set of differential equations, which once solved with the correct boundary conditions will yield the path that minimizes[♠] the distance between two points. This whole exercise seems a bit cumbersome, especially since in flat space it will always yield a straight line — the shortest path. Fortunately, it will, however, provide us with almost all the tools we need to start understanding curved space — or Riemannian geometry.

Let us, hence, enable curvature. Imagine you are walking on a flat field and suddenly a heavy earthquake smoothly deforms the surface. That is to say, the stresses produced by the earthquake stretches, compresses and bends the field — without any cuts or sharp creases. Although you will probably remain on the same spot on the field, your elevation might change. This is because the d-dimensional field is *embedded* in to a $(d+1)$-dimensional space.[♡] Suppose, our position on the field is given by x^μ and our position in the embedded space is given by $\vec{X}$. A infinitesimal distance between two points is given by:

$$\mathrm{d}s^2 = \partial_\mu \vec{X} \partial_\nu \vec{X} \mathrm{d}\dot{x}^\mu \mathrm{d}\dot{x}^\nu = g_{\mu\nu} \mathrm{d}\dot{x}^\mu \mathrm{d}\dot{x}^\nu. \tag{D.4}$$

Here, $g_{\mu\nu}$ is called the *metric tensor*. In in flat space it turns out $g_{\mu\nu} = \delta_{\mu\nu}$. In both eqs. (D.1) and (D.2) the $\delta_{\mu\nu}$ is the specific metric tensor in flat space. The metric tensor is a way to measure distances in our curved space but is also used to define the scalar product between two vectors on our curved space:

$$a^\mu b^\mu \equiv g_{\mu\nu} a^\mu b^\nu \tag{D.5}$$

[♠] There is no maximum for this problem, hence we can safely call the solution to Euler–Lagrange a minimum — although possibly degenerate.

[♡] If we want to imagine the earth's surface assume $d = 2$.

The metric tensor has a determinant often denoted as g and an inverse often denoted as $g^{\mu\nu}$. Although we have described what a tensor is for a two-dimensional surface embedded into three-dimensional space, all the equations we have used are valid in arbitrary dimensions.

To find the shortest distance between two points in our curved space we need to apply the Euler–Lagrange equations eq. (C.3) to $\mathrm{d}s^2$ in eq. (D.4). Doing so, results in the famous geodesic equations:

$$\ddot{x}^\mu + \Gamma^\mu_{\sigma\rho}\dot{x}^\sigma\dot{x}^\rho = 0. \tag{D.6}$$

Here $\Gamma^\mu_{\sigma\rho}$ are called the Christoffel symbols of the second kind, defined as such:

$$\Gamma^\mu_{\sigma\rho} = \tfrac{1}{2}g^{\mu\lambda}\left(\partial_\sigma g_{\lambda\rho} + \partial_\rho g_{\sigma\lambda} - \partial_\lambda g^{\sigma\rho}\right), \tag{D.7}$$

Christoffel symbols of the first kind $\Gamma_{\mu\sigma\rho}$ are defined as such:

$$\Gamma_{\mu\sigma\rho} = g_{\mu\lambda}\Gamma^\lambda_{\sigma\rho} = \tfrac{1}{2}\left(\partial_\sigma g_{\mu\rho} + \partial_\rho g_{\sigma\mu} - \partial_\mu g_{\sigma\rho}\right). \tag{D.8}$$

Christoffel symbols are *not* tensors — they change when the coordinate system changes. The geodesic equation generalizes our notion of a straight line on a curved space. In general a straight line is a line that minimizes the distance between two points.

Appendix E Geometry on a Monge patch

Suppose you are going for a stroll in some $(d+1)$-dimensional space confined on some d-dimensional hypersurface given by the at least $\mathcal{C}^2$ function $f : \mathbb{R}^d \to \mathbb{R}$. Your position is then given by $x^\mu \in \mathbb{R}^d$. This construction is called a *Monge patch* or *Monge gauge*, f is called the *Monge function*. The infinitesimal distance between two points is given by the Pythagorean theorem and is given by:

$$\begin{aligned}
\mathrm{d}s^2 &= \mathrm{d}f^2 + \sum_{i=1}^{d}\mathrm{d}x_i^2 \\
&= \left(\sum_{i=1}^{d}\partial_i f\,\mathrm{d}x_i\right)^2 + \sum_{i=1}^{d}\mathrm{d}x_i^2 \\
&= \sum_{i=1}^{d}(1+\partial_i f^2)\mathrm{d}x_i^2 + \sum_{i\neq j}\partial_i f\partial_j f\,\mathrm{d}x_i^2\mathrm{d}x_j^2.
\end{aligned} \tag{E.1}$$

From eq. (E.1) we conclude the metric tensor for such a Monge patch is given by:♠

$$g_{\mu\nu} = \delta_{\mu\nu} + f_\mu f_\nu. \tag{E.2}$$

Hence we can write:

$$\mathrm{d}s^2 = g_{\mu\nu}\mathrm{d}x^\mu \mathrm{d}x^\nu \tag{E.3}$$

Using Sylvester's determinant theorem, the determinant of the Monge metric is found to be:

$$g = 1 + \delta^{\mu\nu} f_\mu f_\nu, \tag{E.4}$$

where the repeating index is explicitly summed over. The metric inverse is found using the Sherman–Morrison formula and is given by:

$$g^{\mu\nu} = \delta^{\mu\nu} - \frac{1}{g}\delta^{\mu\rho} f_\rho \delta^{\nu\sigma} f_\sigma. \tag{E.5}$$

The Christoffel symbols can be found using the metric — and its inverse — using eq. (D.7) for eq. (E.3), or by solving the Euler–Lagrange equations eq. (C.3) with eq. (E.3) as the Lagrangian and then reading them of the geodesic equation given by eq. (D.6). In any case the Christoffel symbols of the first kind for a Monge patch are given by:

$$\Gamma_{\mu\sigma\rho} = f_\mu f_{\sigma\rho}. \tag{E.6}$$

Using Sylvester's determinant theorem again, we can find the eigenvalues of the metric by solving:♡

$$|(1-\lambda)\delta_{\mu\nu} + f_\mu f_\nu| = 0, \tag{E.7}$$

which yields:

$$\lambda_{1\ldots d-1} = 1 \quad \text{or} \quad \lambda_d = g, \tag{E.8}$$

which tells us that space can only be stretched on a Monge patch as compared to flat space, because $g \geq 1$, as one would expect.

♠Here, f_μ is shorthand notation for $f_\mu = \partial_\mu f$.
♡Here $|\ldots| = \det(\ldots)$ is the determinant.

Appendix F Fixed-point iterations

A common problem in mathematics is finding the zero values of some function $f : \mathbb{R} \to \mathbb{R}$, which is at least $\mathcal{C}^0$. More explicitly, for what values of x does $f(x) = 0$ hold? This is typically not a trivial task especially when x has a multiplicity.

A common, analytical, way to tackle the problem is to find or define some inverse function $f^{-1} : \mathbb{R} \to \mathbb{R}$ for which:

$$f^{-1}(f(x)) = x, \tag{F.9}$$

holds. It turns out, however, that f^{-1} does not always exist. Sometimes it is only valid for a subdomain of $\mathbb{R}$, or sometimes it does not exist at all. For instance, the function $f(x) = 0$ has no inverse, as any input value could produce zero. The function $f(x) = x^2$ has two inverse functions and from the answer — $f(x)$ — it is impossible to know which of the two to take:

$$f^{-1}(x) = \pm\sqrt{x}. \tag{F.10}$$

Fortunately, when studying most physics problems we usually know what solutions to expect from an equation. Even though sometimes the analytical ways are hard or impossible, numerical methods are a good alternative to find the answer. There are a multitude of numerical algorithms out there to solve this problem. Here, we will highlight one of these algorithms called the method of fixed-point iterations.

Suppose we have function $F : \mathbb{R} \to \mathbb{R}$ such that the x for which $F(x) = x$ also solves $f(x) = 0$. In that case we can use fixed-point iterations $x_{i+1} = F(x_i)$ to solve the problem given we guess x_0. Algorithmically, fixed-point iterations are implemented in the following way:

1. For $f(x) = 0$ find a corresponding contracting $F(x) = x$.
2. Make an initial guess x_0, close to x for which $f(x) = 0$.
3. Apply $x_{i+1} = F(x_i)$.
4. Repeat starting step 3 until $|x_{i+1} - x_i|$ is sufficiently small.

The fixed-point iteration converges if $F(x)$ is locally a *contraction mapping* in the neighborhood of x for which $F(x) = x$ or $f(x) = 0$, and where x_0 is sufficiently close to — in accordance to Banach's fixed-point theorem. To prove that a general $F(x)$ is a contraction mapping is a hard task. Therefore, fixed-points iterations are not necessarily a reliable way of solving the equation $f(x) = 0$, but when they work, they work very effectively.

As an example, consider the polynomial $f(x) = ax^2 + bx + c$ for which we would like to know the roots — the values of x for which $f(x) = 0$. If we rewrite $f(x) = 0$ as:

$$F(x) = x = -\frac{1}{a}\left(b + \frac{c}{x}\right), \tag{F.11}$$

we may perform fixed-points iterations on $F(x)$. A simple numerical test shows that this scheme converges for various arbitrary values of a, b, and c when $\sqrt{b^2 - 4ac} \in \mathbb{R}$, and when the initial value is chosen sufficiently close to a fixed point. An example program can be found in listing F.1.

It is worth pointing out that if x is multivalued — there are multiple distinct x's for which $f(x) = 0$ both depending on the attractiveness of the fixed point as well as where x_0 is chosen, the algorithm will converge to one of the solutions — provided the algorithm converges at all.

A benefit of fixed-point iterations is that it also work for higher dimensional problems of the form $f : \mathbb{R}^d \to \mathbb{R}^d$ where we have to find a corresponding $F^\mu(x^\mu) = x^\mu$, such that fixed-point iterations can be performed. For instance one could consider the function:

$$f^\mu(x^\mu) = \delta^{\mu\nu}\left(A_{\nu\sigma\rho}x^\sigma x^\rho - B_{\nu\sigma}x^\sigma + C_\nu\right) = 0, \tag{F.12}$$

with the fixed-point equation:

$$F^\mu(x^\mu) = \bar{B}^{\mu\sigma}\left(A_{\mu\sigma\rho}x^\sigma x^\rho + C_\mu\right) = x^\mu, \tag{F.13}$$

where $\bar{B}^{\mu\sigma}$ is the inverse of $B_{\mu\sigma}$.

Appendix G Numerical differentiation

A commonly overlooked tool in computational sciences is the method of *automatic differentiation*. Typically, numerical differentiation is done using the method of *finite differences*. Automatic differentiation, is an *exact* method of computing the derivative of a function for a given value. In order to understand how it works we first do a small recap of some high school math.

```cpp
#include <stdio.h>
#include <stdlib.h>
#include <math.h>
#include <time.h>
#include <limits>

using namespace std;
const double pi=acos(-1.0);
const double scale=5.0;
double a,b,c;

double f(double x)
{
    return a*pow(x,2)+b*x+c;
}

double F(double x)
{
    return -(b+c/x)/a;
}

double fxdpt(double x)
{
    int counter=0;
    double xp;
    do
    {
        x=F(xp=x);
        printf("%d: xp=%.17g, x=%.17g, F(x)=%.17g, f(x)=%.17g\n",counter,xp,x,F(x),f(x));
        counter++;
    }
    while(fabs(f(x))>numeric_limits<double>::epsilon() and counter<=0xFF);
    return x;
}

int main()
{
    srand48(time(NULL));
    double xpp,xmm;
    do
    {
        a=(2.0*drand48()-1.0)*scale;
        b=(2.0*drand48()-1.0)*scale;
        c=(2.0*drand48()-1.0)*scale;
        xpp=(-b+sqrt(pow(b,2)-4.0*a*c))/(2.0*a);
        xmm=(-b-sqrt(pow(b,2)-4.0*a*c))/(2.0*a);
    }
    while(isnan(xpp) or isnan(xmm));
    printf("a = %.17g, b = %.17g, c = %.17g\n",a,b,c);
    printf("x_+ = %.17g, x_- = %.17g\n",xpp,xmm);
    printf("f(x_+) = %.17g, f(x_-) = %.17g\n",f(xpp),f(xmm));
    const double miss=2.0*drand48();
    printf("x_0 = %.17g\n",miss*xpp);
    const double x=fxdpt(miss*xpp);
    printf("x=%.17g, f(x)=%.17g\n",x,f(x));
    if(fabs(x-xpp)<fabs(x-xmm)) printf("|x-x_+|=%.17g\n",fabs(x-xpp));
    else printf("|x-x_-|=%.17g\n",fabs(x-xmm));
    return EXIT_SUCCESS;
}
```

Listing F.1: An implementation for fixed-point iterations algorithm written in C++.

Suppose we have an at least $\mathcal{C}^1$ function $f : \mathbb{R} \to \mathbb{R}$. By definition the derivative $f'(x)$ is given by:

$$f'(x) \equiv \frac{\mathrm{d}f}{\mathrm{d}x} \equiv \lim_{h \to 0} \frac{1}{h} \left(f(x+h) - f(x) \right). \tag{G.1}$$

As an example, we can find the derivative of the function $f(x) = x^2$ by applying the definition in eq. (G.1):

$$\begin{aligned} f'(x) &= \lim_{h \to 0} \frac{1}{h} \left((x+h)^2 - x^2 \right) \\ &= \lim_{h \to 0} \frac{1}{h} \left(x^2 + h^2 + 2hx - x^2 \right) \\ &= \lim_{h \to 0} 2x + h \\ &= 2x. \end{aligned} \tag{G.2}$$

Higher-order derivatives can be found by re-applying eq. (G.1) up to the desired order. Say we are interested in the n^{th} order derivative, denoted by $f^n(x)$ or $\frac{\mathrm{d}^n f}{\mathrm{d}x^n}$, we just find the $(n-1)^{\text{th}}$ derivative, and then take its derivative. Since we know f, f^n can always be induced, if it exists. Hence, in our example we can find $f''(x)$ by taking the derivative of the previously found $f'(x) = 2x$ which yields: $f''(x) = 2$. One of the implications of eq. (G.1) is called Taylor's theorem which states that♠

$$f(x) = \sum_{n=0}^{\infty} \frac{1}{n!} \frac{\mathrm{d}^n f(a)}{dx^n} (x-a)^n, \tag{G.3}$$

where a is some arbitrary value in the domain of f.

It it worth mentioning that differentiation can be extended to work in higher dimensions as well.

G.1 Method of finite differences

Letting a computer find an exact derivative using eq. (G.1) is a very hard task. It is not a priori obvious whether a limit exists and what manipulations ought to be done to find the derivative. A straightforward solution to this problem is an approximate method called *finite difference*. The idea behind finite difference is roughly to omit the limit in eq. (G.1) and rather use an arbitrary small value for h instead. As this method is an approximate method it is always possible

♠As the following equation is purely a reminder, a proof will not be given here.

to improve the accuracy as is extensively done in Fornberg [158]. For brevity's sake we choose the most natural and trivial version of this method here. The simplest way of approximating a derivative numerically is done by:

$$f'(x) = \tfrac{1}{h}\left(f(x+h) - f(x)\right) + \mathcal{O}\left(h^2\right). \tag{G.4}$$

Now, let us take our previous example again. Suppose we want to know the value of the derivative in $x = 3$. We pick a small $h = 10^{-3}$ — for instance — and find:

$$\begin{aligned} f'(3) &\approx \frac{f(3+10^{-3}) - f(3)}{10^{-3}3} \\ &= \frac{9.006001 - 9}{10^{-3}} \\ &= \frac{0.006001}{10^{-3}} \\ &= 6.001. \end{aligned} \tag{G.5}$$

Obviously the value in eq. (G.5) is off by a little: the exact value should be $f'(3) = 6$ as found in eq. (G.2). Unfortunately, the finite difference method — even with higher accuracies — is a source of noise and artifacts in numerical simulations. Therefore an exact method would be very much preferred.

G.2 Symbolic differentiation

One way of achieving exact derivatives computationally is to hard code them into the computer code. This method becomes a somewhat tedious and error prone task when a lot of functions need to be differentiated. Another method would be to let the computer symbolically find all the derivatives of a function, and then generate and evaluate this function. Symbolic differentiation is done by taking standard operations and functions and applying eq. (G.1) to it. Typically for functions $f(x), g(x) : \mathbb{R} \to \mathbb{R}$, a table like table G.1 is found. This method is somewhat slow and hard to implement because a function needs to be parsed, then proper symbolic differentiation rules need to be applied, and then needs to be evaluated, which all end up being a complicated and computationally expensive task. Fortunately, there is yet another method that solves all these problems and this method is called automatic differentiation.

Name	Function	Derivative
Linear rule	af	af'
Sum rule	$f \pm g$	$f' \pm g'$
Product rule	fg	$f'g + fg'$
Quotient rule	$\frac{f}{g}$	$\frac{f'g - fg'}{g^2}$
Chain rule	$f(g)$	$f'(g)g'$
Constant rule	a	0
Power rule	x^n	nx^{n-1}
Exponential rule	a^x	$a^x \log a$
Logarithmic rule	$\log x$	$\frac{1}{x}$

Table G.1: Common rules for symbolic differentiation using the functions $f(x), g(x) : \mathbb{R} \to \mathbb{R}$.

Name	Operation	Result
Linear	$a(x + \varepsilon x')$	$ax + \varepsilon a x'$
Sum	$(x + \varepsilon x') \pm (y + \varepsilon y')$	$x \pm y + \varepsilon(x' \pm y')$
Product	$(x + \varepsilon x')(y + \varepsilon y')$	$xy + \varepsilon(x'y + xy')$
Quotient	$\frac{x+\varepsilon x'}{y+\varepsilon y'}$	$\frac{x}{y} + \varepsilon(\frac{x'y - xy'}{y^2})$

Table G.2: Basic mathematical operations for dual numbers.

G.3 Automatic differentiation

Automatic differentiation can be achieved by using *dual numbers*. We define dual numbers by introducing the following set[♠] $\mathbb{D} = \mathbb{R} \otimes \varepsilon\mathbb{R}$ such that $\varepsilon \neq 0$ and $\varepsilon^2 = 0$. Henceforth, we will write a that a dual number $\chi = x + \varepsilon x'$ where x is called the real part and x' is called the nilpotent part. Basic mathematical operations for dual numbers are listed in table G.2. Table G.2 reminds us somewhat of table G.1 and in fact it turns out that if we use Taylor's theorem,

[♠] This definition is similar to complex numbers where $\mathbb{C} = \mathbb{R} \otimes i\mathbb{R}$ such that $i^2 - 1$.

eq. (G.3), we find:

$$f(x+\varepsilon x') = \sum_{n=0}^{\infty} \frac{1}{n!} \frac{\mathrm{d}^n f(x)}{dx^n} (\varepsilon x')^n = f(x) + \varepsilon f'(x). \tag{G.6}$$

Meaning that whenever we take a function $f(x) : \mathbb{R} \to \mathbb{R}$ and promote it to $\bar{f}(x) : \mathbb{D} \to \mathbb{D}$ and evaluate it, the real part yields the function value, and the nilpotent value yields the function's derivative. We *automatically* obtain the function's derivative, just by evaluating the function for the appropriate dual number.

Computationally, the only thing that needs to be done is to *explain* to the computer how to work with dual numbers; explicitly, to define all the operators and special functions for dual numbers.♠

Automatic differentiation can be generalized to multivariable functions by promoting $f : \mathbb{R}^n \to \mathbb{R}^m$ to $f : \mathbb{D}^n \to \mathbb{D}^m$. Similarly, it can be used to find higher-order derivatives by introducing additional nilpotent variables.

Appendix H Numerical integration

Another commonly used tool of mathematics is *integration*. There are many ways to define integrals; we will use the Riemannian definition here:

$$\int_a^b f(x)\,\mathrm{d}x \equiv \lim_{h\to 0} h \sum_i^N f\left(a + hi\right), \tag{H.1}$$

where N is given by $N = \frac{b-a}{h}$. Informally, the integral is a measure of the sum of the areas between $f(x)$ and the x-axis. An often used concept is the *primitive* function $F(x)$ defined as such:

$$F(x) \equiv \int_0^x f(\xi)\,\mathrm{d}\xi. \tag{H.2}$$

The primitive is sometimes called the *antiderivative* due to the fundamental theorem of calculus which states:

$$f(x) = \int_0^x f'(\xi)\,\mathrm{d}\xi. \tag{H.3}$$

♠ Analogous to the way complex numbers are implemented on a computer.

An integral is linear in the following sense:

$$\int_a^b f(x)\,\mathrm{d}x + \int_b^c f(x)\,\mathrm{d}x + \int_a^c f(x)\,\mathrm{d}x, \tag{H.4}$$

and for a $\alpha \in \mathbb{R}$, constant:

$$\int_a^b \alpha f(x)\,\mathrm{d}x = \alpha \int_a^b f(x)\,\mathrm{d}x. \tag{H.5}$$

Numerically a generic integral can be approximated through various methods. We will highlight a few of these methods. The following methods assume that $t_{n+1} = t_n + h$ for small h. The methods can, however, be composited due to the linearity properties of the integral to integrate over larger intervals. First, the rectangle method, or rectangle rule:

$$\int_{t_n}^{t_{n+1}} f(t)\,\mathrm{d}t \approx h f(t_n), \tag{H.6}$$

which is a simple discretization of the definition of the integral, eq. (H.1). Second, the trapezoid method, or trapezoid rule:

$$\int_{t_n}^{t_{n+1}} f(t)\,\mathrm{d}t \approx \frac{h}{2}\left(f(t_{n+1}) + f(t_n)\right). \tag{H.7}$$

Finally, the Simpson method, or Simpson's rule:

$$\int_{t_n}^{t_{n+1}} f(t)\,\mathrm{d}t \approx \frac{h}{6}\left(f(t_{n+1}) + 4f\left(\tfrac{h}{2}\right) + f(t_n)\right). \tag{H.8}$$

Appendix I Forward Euler

One of the most trivial and common methods to solve differential equations is called *Forward Euler* [170]. Suppose we have the ordinary differential equation given by

$$\dot{x}^\mu(t) = f^\mu(x^\rho, t), \quad x(0) = 0, \tag{I.1}$$

for some arbitrary function $f(x) : \mathbb{R}^{d+1} \to \mathbb{R}^d$, using the definition of derivatives given in eq. (G.1) with a finite h — resembling the finite differences method discussed in appendix section G.1. Here, h is called the *time step* because we define the recurrent equation: $t_{i+1} = t_i + h$, where t_i is the time

series, the discrete variable representing t. Here, all series have an index i representing the number of time steps taken. The initial value of the index is zero, $i = 0$. We can then rewrite eq. (I.1) as such:

$$x^{\mu}_{i+1} = x^{\mu}_{i} + hf^{\mu}(x^{\rho}_{t}, t_i) + \mathcal{O}(h^2), \quad x^{\mu}_{0} = 0, \tag{I.2}$$

yielding a recurrent formula, which can be computed iteratively since we know the initial value x_0. As $h \to 0$ in eq. (I.2) the answer becomes more and more exact, although in principle corrections of order $\mathcal{O}(h^2)$ can always be applied.

When applying Forward Euler to a second order differential equation:

$$\ddot{x}^{\mu}(t) = f^{\mu}(\dot{x}^{\rho}, x^{\sigma}, t), \quad x^{\mu}(0) = 0, \quad \dot{x}^{\mu}(0) = 0 \tag{I.3}$$

for some arbitrary function $f(x) : \mathbb{R}^{2d+1} \to \mathbb{R}^{d}$, we first need to split one second-order differential equation to two first-order differential equations. We do so by introducing a *dummy* variable $y^{\mu} = \dot{x}^{\mu}$, substitution yields:

$$\begin{aligned} \dot{x}^{\mu}(t) &= y^{\mu}, & x^{\mu}(0) &= 0 \\ \dot{y}^{\mu}(t) &= f^{\mu}(y^{\rho}, x^{\sigma}, t), & y^{\mu}(0) &= 0, \end{aligned} \tag{I.4}$$

and we have turned our problem into a system of two first-order differential equations. Now we once again use the method of finite differences to find a recurrent solution — analogous to eq. (I.2) — which is now given by:

$$\begin{aligned} x^{\mu}_{i+1} &= x^{\mu}_{i} + hy^{\mu}_{i} + \mathcal{O}(h^2), & x^{\mu}_{0} &= 0 \\ y^{\mu}_{i+1} &= y^{\mu}_{i} + hf^{\mu}(y^{\rho}_{i}, x^{\sigma}_{i}, t_i), & y^{\mu}_{0} &= 0. \end{aligned} \tag{I.5}$$

Undoing the substation of $y^{\mu} = \dot{x}^{\mu}$ turn eq. (I.5) into:

$$\begin{aligned} x^{\mu}_{i+1} &= x^{\mu}_{i} + h\dot{x}^{\mu}_{i} + \mathcal{O}(h^2), & x^{\mu}_{0} &= 0 \\ \dot{x}^{\mu}_{i+1} &= \dot{x}^{\mu}_{i} + hf^{\mu}(\dot{x}^{\rho}_{i}, x^{\sigma}_{i}, t_i), & \dot{x}^{\mu}_{0} &= 0. \end{aligned} \tag{I.6}$$

As eqs. (I.2) and (I.6) are similarly derived, in both of the cases the answer is approximate up to order $\mathcal{O}(h^2)$. Equation (I.3) and therefore eq. (I.6) are equal to Newton's equations of motion, eq. (A.2), if $f^{\mu}(\dot{x}^{\rho}_{i}, x^{\sigma}_{i}, t_i) = \frac{1}{m}F^{\mu}_{i}$, where F^{μ}_{i} is the total force at timestep i on the body of interest with mass m. For conservative systems, $f^{\mu}(\dot{x}^{\rho}_{i}, x^{\sigma}_{i}, t_i) = -\frac{1}{m}\delta^{\mu\nu}\partial^{i}_{\nu}V(x^{\lambda}_{i})$, as found using eq. (B.4).

This method is called *forward* Euler because we have used forward differences to derive eqs. (I.2) and (I.6). Backward differences can also be used, this would be called *backward* Euler. The downside of backward Euler is that it typically yields an *implicit* algebraic equation that ought to be solved before continuing — often done using an iterative numerical scheme. Hence, backward Euler and forward Euler are respectively called implicit and explicit integrators. The upside of an explicit integrator is that it typically performs faster because no additional iterations are required to solve the implicit algebraic equation. The upside of an implicit integrator is that they are numerically more *stable* compared to explicit integrators. A numerical solution to an equation is unstable when it diverges — rapidly — from the analytic solution.

Appendix J Runge–Kutta's method

In appendix I we discovered how to solve a differential equation numerically, in a iterative fashion. We also discussed that the numerical is approximate up to first order, $\mathcal{O}(h)$. Since we solve the equation iteratively, that is to say for small time steps h, the error in our solution will accumulate over large time intervals. This is a problem both for the relevance and stability of a solution. An obvious solution is to decrease the time step h. The downside to this is, however, that for every decrement in the time step h we have to increase the number of iterations to yield the physical time as $t_{t+1} = t_t + h$. If we decrease h by a factor of 10, the computer has to do a factor of 10 more iterations and is hence a factor 10 slower.

Fortunately, we can do a higher-order approximation to the derivative, using the method of finite differences, and some additional tweaking. One popular way of doing that is called the Runge–Kutta method. For the equation:

$$\ddot{x}^\mu(t) = f^\mu(x^\mu, t), \quad x^\mu(0) = 0, \quad \dot{x}^\mu(0) = 0 \tag{J.1}$$

The Runge–Kutta method gives the solution:

$$\begin{aligned} x^\mu_{i+1} &= x^\mu_i + h\left(\dot{x}^\mu_i + \tfrac{1}{6}(k^\mu_1 + 2k^\mu_2)\right) + \mathcal{O}(h^4), & x^\mu_0 &= 0 \\ \dot{x}^\mu_{i+1} &= \dot{x}^\mu_i + \tfrac{1}{6}k^\mu_1 + \tfrac{1}{6}k^\mu_2 + \tfrac{1}{6}k^\mu_3, & \dot{x}^\mu_0 &= 0, \end{aligned} \tag{J.2}$$

with:

$$\begin{aligned} k^\mu_1 &= hf^\mu(x^\mu_i, t_i) \\ k^\mu_2 &= hf^\mu(x^\mu_i + \tfrac{h}{2}\dot{x}^\mu_i + \tfrac{h}{8}k^\mu_1, t_i + \tfrac{h}{2}) \\ k^\mu_3 &= hf^\mu(x^\mu_i + h\dot{x}^\mu_i + \tfrac{h}{2}k^\mu_2, t_i + h). \end{aligned} \tag{J.3}$$

The Runge–Kutta method solves Newton's equation for conservative forces eq. (B.2) up to third order accuracy $\mathcal{O}(h^3)$. Therefore this version of Runge–Kutta is also refered to as the Runge–Kutta 3 method.

Appendix K Symplectic Euler

Symplectic Euler is one of the simplest symplectic integrators that can be derived with the method of variational integration — as described in section 4.2. As discussed in appendix C, the Lagrangian for classical systems is given by $L = \frac{1}{2}m\dot{x}^2 - V$, see eq. (C.4). In order to discretize the Lagrangian we need to perform the integral in eq. (4.7). For the symplectic Euler method we will use the rectangle method for approximating integrals as discussed in appendix H, eq. (H.6). We will, additionally, discretize the velocity by approximating the numerical derivative as discussed in appendix section G.1, eq. (G.4), which yields:

$$\dot{x}^\mu = \tfrac{1}{h}\left(x^\mu_{i+1} - x^\mu_i\right). \tag{K.1}$$

Hence, we find the discrete Lagrangian for symplectic Euler to be given:

$$L_D^{\text{rect}}(x^\mu_i, x^\mu_{i+1}) = \tfrac{m}{2h}\left(\delta_{\mu\nu}x^\mu_{i+1}x^\nu_{i+1} - 2\delta_{\mu\nu}x^\mu_i x^\nu_{i+1} + \delta_{\mu\nu}x^\mu_i x^\nu_i\right) - hV_i. \tag{K.2}$$

Before we continue to apply the discrete Euler–Lagrange, we first establish the following identities:

$$\partial^i_\sigma \delta_{\mu\nu}x^\mu_j x^\nu_k = \delta_{\mu\nu}\left(\delta_{ji}\delta^\mu_\sigma x^\nu_k + \delta_{ki}x^\mu_j\delta^\nu_\sigma\right). \tag{K.3}$$

Applying the discrete Euler–Lagrange equations, eq. (4.11), to our discrete Lagrangian eq. (K.2) then yields:

$$\tfrac{m}{h}\left(2x^\mu_i - x^\mu_{i+1} - x^\mu_{i-1}\right) - h\delta^{\mu\sigma}\partial^i_\sigma V_i = 0. \tag{K.4}$$

When further simplyfing eq. (K.4), we find:

$$x^\mu_{i+1} = x^\mu_i + h\dot{x}^\mu_i - \tfrac{h^2}{m}\delta^{\sigma\mu}\partial^i_\sigma V_i. \tag{K.5}$$

Upon computing eq. (4.12), for this discrete Lagrangian, eq. (K.2) we obtain the following result:

$$\dot{x}^\mu_{i+1} = \tfrac{1}{h}\left(x^\mu_{i+1} - x^\mu_i\right), \tag{K.6}$$

which is somewhat remarkable as one might have expected it to be $\dot{x}_i^\mu$ instead. Upon substitution we find the following discrete equations of motion:

$$\dot{x}_{i+1}^\mu = \dot{x}_i^\mu - \tfrac{h}{m}\delta^{\sigma\mu}\partial_\sigma^i V_i, \tag{K.7}$$
$$x_{i+1}^\mu = x_i^\mu + h\dot{x}_{i+1}^\mu. \tag{K.8}$$

When invoking eq. (B.2), eq. (K.7) becomes:

$$\dot{x}_{i+1}^\mu = \dot{x}_i^\mu + \tfrac{h}{m}F_i^\mu, \tag{K.9}$$
$$x_{i+1}^\mu = x_i^\mu + h\dot{x}_{i+1}^\mu. \tag{K.10}$$

for non-conservative systems.

Appendix L Velocity Verlet

The velocity Verlet method is a symplectic method with higher order accuracy than Symplectic Euler. It can be found using the trapezoidal method eq. (H.7) when discretizing the Lagrangian — as we saw, when the rectangle method is invoked, we obtain symplectic Euler (see appendix K). For brevity we will impose the well known velocity Verlet equation here:

$$x_{i+1}^\mu = x_i^\mu + h\dot{x}_i^\mu + \tfrac{h^2}{2m}F^\mu(x_i^\mu), \tag{L.1}$$
$$\dot{x}_{i+1}^\mu = \dot{x}_i^\mu + \tfrac{h}{2m}\left(F^\mu(x_i^\mu) + F^\mu(x_{i+1}^\mu)\right), \tag{L.2}$$

For the velocity in eq. (L.2) the forces F_{i+1}^μ for the new positions have to be recomputed — this has a bad computational performance impact. In addition, note how the force $F^\mu(x_{i+1}^\mu)$ is solely a function of position x_{i+1}^μ, as we are calculating the new velocity $\dot{x}_{i+1}^\mu$. If the force would be dependent on the velocity $\dot{x}^\mu$ — which is the case for active or damped systems — eq. (L.2) would become implicit, which is yet another computational performance impact.

Appendix M The discrete conservation of energy

In this appendix we compare the energy increment per time step of forward Euler and symplectic Euler. The discrete Hamiltonian at timestep i, H_i, is given by:

$$H_i = \tfrac{1}{2}m\dot{x}_i^2 + V\left(x_i^\mu\right). \tag{M.1}$$

Therefore, H_{i+1} is given by:

$$H_{i+1} = \tfrac{1}{2} m \dot{x}_{i+1}^2 + V\left(x_{i+1}^\mu\right). \tag{M.2}$$

Upon computing the Hamiltonian difference $\Delta H = H_{i+1} - H_i$, we find the energy increment per timestep

$$\Delta H = \tfrac{1}{2} m \left(\dot{x}_{i+1}^2 - \dot{x}_i^2\right) + V\left(x_{i+1}^\mu\right) - V\left(x_i^\mu\right). \tag{M.3}$$

We do so for both forward Euler and symplectic Euler.

M.1 Forward Euler

The forward Euler equations for conservative systems are found in appendix I and are given by:

$$\dot{x}_{i+1}^\mu = \dot{x}_i^\mu - \tfrac{h}{m} \delta^{\mu\nu} \partial_\nu^i V\left(x_i^\lambda\right), \tag{M.4}$$

$$x_{i+1}^\mu = x_i^\mu + h \dot{x}_i^\mu. \tag{M.5}$$

We, hence, compute the Hamiltonian difference for forward Euler ΔH^f and initially find:

$$\begin{aligned} \Delta H^f = &- h \dot{x}_i^\lambda \delta_{\lambda\mu} \delta^{\mu\nu} \partial_\nu^i V\left(x_i^\lambda\right) + \tfrac{h^2}{2m} \left(\delta^{\mu\nu} \partial_\nu^i V\left(x_i^\lambda\right)\right)^2 \\ &+ V\left(x_i^\lambda + h \dot{x}_i^\lambda\right) - V\left(x_i^\lambda\right), \end{aligned} \tag{M.6}$$

since:

$$\tfrac{1}{2} m \left(\dot{x}_{i+1}^2 - x_i^2\right) = -h \dot{x}_i^\lambda \delta_{\lambda\mu} \delta^{\mu\nu} \partial_i^\mu V\left(x_i^\lambda\right) + \tfrac{h^2}{2m} \left(\delta^{\mu\nu} \partial_\nu V\left(x_i^\lambda\right)\right)^2. \tag{M.7}$$

Upon Taylor expanding the potential term up to second order in h, we find:

$$\Delta H^f = \tfrac{h^2}{2m} \left(\delta^{\mu\nu} \partial_\nu^i V\left(x_i^\lambda\right)\right)^2 + \tfrac{h^2}{2} \dot{x}_i^\mu \dot{x}_i^\nu \partial_\mu^i \partial_\nu^i V\left(x_i^\lambda\right) + \mathcal{O}\left(h^3\right), \tag{M.8}$$

$$= \tfrac{1}{2} m \left(\dot{x}_{i+1}^\mu - \dot{x}_i^\mu\right)^2 + \tfrac{h^2}{2} \dot{x}_i^\mu \dot{x}_i^\nu \partial_\mu^i \partial_\nu^i V\left(x_i^\lambda\right) + \mathcal{O}\left(h^3\right), \tag{M.9}$$

as the Taylor expansion yields:

$$\begin{aligned} V\left(x_i^\lambda + h \dot{x}_j^\lambda\right) = &V\left(x_i^\lambda\right) + h \dot{x}_j^\lambda \delta_{\lambda\mu} \delta^{\mu\nu} \partial_\nu V\left(x_i^\lambda\right) \\ &+ \tfrac{h^2}{2} \dot{x}_j^\mu \dot{x}_j^\nu \partial_\mu^i \partial_\nu^i V\left(x_i^\lambda\right) + \mathcal{O}\left(h^3\right). \end{aligned} \tag{M.10}$$

M.2 Symplectic Euler

The symplectic Euler equations for conservative systems are found in appendix K and are given by:

$$\dot{x}^{\mu}_{i+1} = \dot{x}^{\mu}_{i} - \tfrac{h}{m}\delta^{\mu\nu}\partial^{i}_{\nu}V\left(x^{\lambda}_{i}\right), \tag{M.11}$$

$$x^{\mu}_{i+1} = x^{\mu}_{i} + h\dot{x}^{\mu}_{i+1}. \tag{M.12}$$

We, hence, also compute the Hamiltonian difference for symplectic Euler ΔH^{s} and similarly eq. (M.6) initially find:

$$\begin{aligned}\Delta H^{s} = &- h\dot{x}^{\lambda}_{i}\delta_{\lambda\mu}\delta^{\mu\nu}\partial^{i}_{\nu}V\left(x^{\lambda}_{i}\right) + \tfrac{h^{2}}{2m}\left(\delta^{\mu\nu}\partial^{i}_{\nu}V\left(x^{\lambda}_{i}\right)\right)^{2} \\ &+ V\left(x^{\lambda}_{i} + h\dot{x}^{\lambda}_{i+1}\right) - V\left(x^{\lambda}_{i}\right).\end{aligned} \tag{M.13}$$

Upon Taylor expanding the potential term up to second order in h, eq. (M.10) and substituting $\dot{x}^{\mu}_{i+1}$ given by eq. (M.12), we find:

$$\Delta H^{s} = -\tfrac{h^{2}}{2m}\left(\delta^{\mu\nu}\partial^{i}_{\nu}V\left(x^{\lambda}_{i}\right)\right)^{2} + \tfrac{h^{2}}{2}\dot{x}^{\mu}_{i}\dot{x}^{\nu}_{i}\partial^{i}_{\mu}\partial^{i}_{\nu}V\left(x^{\lambda}_{i}\right) + \mathcal{O}\left(h^{3}\right), \tag{M.14}$$

$$= -\tfrac{1}{2}m\left(\dot{x}^{\mu}_{i+1} - \dot{x}^{\mu}_{i}\right)^{2} + \tfrac{h^{2}}{2}\dot{x}^{\mu}_{i}\dot{x}^{\nu}_{i}\partial^{i}_{\mu}\partial^{i}_{\nu}V\left(x^{\lambda}_{i}\right) + \mathcal{O}\left(h^{3}\right). \tag{M.15}$$

At this point we observe that the kinetic part of the equation vanishes when mechanical equilibrium is assumed and we indeed find energetic conservation [103, 129, 136].

Appendix N Conjugate Gradient

A widely used way to minimize a scalar function $f(x^{\mu}) : \mathbb{R}^{d} \to \mathbb{R}$ is by the so called conjugate gradient method. The conjugate gradient method relies on fact that

$$-\delta^{\mu\sigma}\partial_{\sigma}f(x^{\mu})$$

is the direction of steepest descent, hence, $f(x^{\mu})$ ought to be at least $\mathcal{C}^{1}$ now. Essentially, we could always walk in the direction of steepest descent until we reach the nearest valley in that direction and repeat until we are stuck at a point where the gradient is zero valued — the minimum.[♠] This is roughly

[♠] We are descending, we should not get stuck at any other stationary point.

how the conjugate method works. It improves, however, on the number of iterations we have to do before reaching the minimum. It does so by predicting the direction of the valley's descent instead of crisscrossing through it. This is achieved as follows:

1. Calculate the steepest descent vector $d_i^\mu = -\delta^{\mu\sigma}\partial_\sigma f(x_i^\mu)$.
2. Find the conjugate direction vector $\Delta_i^\mu = d_i^\mu + C_i\Delta_{i-1}^\mu$.
3. Perform a line minimization in the direction of Δ_i^μ and find the optimal λ in:

$$\lambda = \arg\min_\lambda f(x_i^\mu + \lambda\Delta_i^\mu), \tag{N.1}$$

   and $x^{i+1} = x_i^\mu + \lambda\Delta_i^\mu$ accordingly.
4. If $|\delta^{\mu\sigma}\partial_\sigma f(x_i^\mu)|$ is not sufficiently small go to step 1.

To kickstart the algorithm we assume $\Delta_0^\mu = d_0^\mu$. The C_i in step 2 is found by one of the following definitions:

- Fletcher–Reeves:

$$C_i^{\text{FR}} = \frac{\delta_{\mu\nu}x_i^\mu x_i^\nu}{\delta_{\mu\nu}x_{i-1}^\mu x_{i-1}^\nu}. \tag{N.2}$$

- Polak–Ribiére:

$$C_i^{\text{PR}} = \frac{\delta_{\mu\nu}x_i^\mu\left(x_i^\nu - x_{i-1}^\nu\right)}{\delta_{\mu\nu}x_{i-1}^\mu x_{i-1}^\nu}. \tag{N.3}$$

- Hestenes–Stiefel:

$$C_i^{\text{HS}} = \frac{\delta_{\mu\nu}x_i^\mu\left(x_i^\nu - x_{i-1}^\nu\right)}{\delta_{\mu\nu}\Delta_{i-1}^\mu\left(x_i^\nu - x_{i-1}^\nu\right)}. \tag{N.4}$$

- Dai–Yuan:

$$C_i^{\text{DY}} = \frac{\delta_{\mu\nu}x_i^\mu x_i^\nu}{\delta_{\mu\nu}\Delta_{i-1}^\mu\left(x_i^\nu - x_{i-1}^\nu\right)}. \tag{N.5}$$

For the first iteration we may use $C_0 = 1$. Each of these definitions has its own benefits; typically it is easy to implement a few and see which one performs better for your problem although in most cases the choice should not matter too much.

Appendix O Molecular dynamics

In the eyes of a physicist — possibly a theoretical soft matter physicist — the method of molecular dynamics [117, 144] is nothing but the generalized classical N-body problem solved computationally. The generalized classical N-body problem is basically N bodies interacting in some way. In the most general case we end up with a dynamical system of coupled equations:

$$m_n \ddot{x}_n^\mu = F_n^\mu \left(x_0^\mu, \dots, x_{N-1}^\mu \right), \tag{O.1}$$

where n denotes the n^{th} particle in the system and is the total force acting on the n^{th} particle is given by $F_n^\mu \left(x_0^\mu, \dots, x_{N-1}^\mu \right)$. In the presence of curvature, the equations of motion for the dynamical system are given by:

$$m_n \left(\ddot{x}_n^\mu + \Gamma_{\sigma\rho}^{\mu\, n} \dot{x}_n^\sigma \dot{x}_n^\rho \right) = F_n^\mu \left(x_0^\mu, \dots, x_{N-1}^\mu \right). \tag{O.2}$$

We have discussed symplectic methods for solving eq. (O.1) in chapter 4, particularly section 4.2 provided we discretize time. Depending on the type of system, we may choose Velocity Verlet as described in appendix L for conservative systems. For non-conservative we choose symplectic Euler appendix K, and in the presence of curvature we may use a modified variant of symplectic Euler as described in section 4.3. Obviously, in order to perform these methods initial conditions per particle are a necessity.

Although we are solving Newton's equations for every individual particle, we are usually not necessarily interested in the individual trajectories of these particles. Usually, we are interested in the statistical behavior of the system as a whole. Hence, molecular dynamics should be seen a method for solving statistical physics-type questions. As we are interested in statistical effects we choose N, the number, of particles to be large — canonically of the order one hundred to one hundred thousand.

Typically, interactions between particles are assumed to be pairwise, meaning a particle i interacts with a particle j yielding a force on particle i in the most general form given by:

$$\begin{aligned} F_{ij}^\mu \left(x_i^\mu, x_j^\mu \right) &= -g_i^{\mu\nu} \partial_\nu^i V_{ij} \left(\mathrm{d} \left(x_j^\mu, x_i^\mu \right) \right) \\ &= -g_i^{\mu\nu} \frac{V_{ij} \left(\mathrm{d} \left(x_j^\mu, x_i^\mu \right) \right)}{\mathrm{d} \left(x_j^\mu, x_i^\mu \right)} \frac{\mathrm{d}^\nu \left(x_j^\mu, x_i^\mu \right)}{\mathrm{d} \left(x_j^\mu, x_i^\mu \right)}, \end{aligned} \tag{O.3}$$

where $\mathrm{d}\left(x_j^\mu, x_i^\mu\right)$ is the distance between particle i and j and $\mathrm{d}^\mu\left(x_j^\mu, x_i^\mu\right)$ is the distance vector pointing from particle i towards particle j. Obviously, by Newton's third law, eq. (A.3) — which is only valid if $g_i^{\mu\nu} = g_j^{\mu\nu}$; which is the case in flat space — the force on particle j is given by:

$$F_{ji}^\mu\left(x_j^\mu, x_i^\mu\right) = -F_{ij}^\mu\left(x_i^\mu, x_j^\mu\right). \tag{O.4}$$

Finally, to find the total resulting forces on particle i we take the sum:

$$F_i^\mu = F_{\text{add}}^\mu - g_i^{\mu\nu}\partial_\nu^i \sum_{j\neq i}^{N} V_{ij}\left(\mathrm{d}\left(x_j^\mu, x_i^\mu\right)\right), \tag{O.5}$$

where F_{add}^μ are additional non-conservative forces.

As N increases we observe an computational performance problem. In order to find the resultant forces on particle i — given that there are interactions — we need to perform N^2 calculations. Hence, the complexity of solving Newton's equations of motion for N interaction particles scales as $\mathcal{O}\left(N^2\right)$. Fortunately, however, in many physical systems it turns out that the pairwise interaction potential $V_{ij}(r)$ is small as r increases. Such potentials are called short range. For short range potentials the sum in eq. (O.5) can be truncated to be only a sum over its neighbors:

$$\begin{aligned} F_i^\mu &= F_{\text{add}}^\mu - g_i^{\mu\nu}\partial_\nu^i \sum_{\langle ij\rangle}^{N} V_{ij}\left(\mathrm{d}\left(x_j^\mu, x_i^\mu\right)\right) \\ &= F_{\text{add}}^\mu - g_i^{\mu\nu}\partial_\nu^i \sum_{i\neq j}^{N} V_{ij}^{\text{tr}}\left(\mathrm{d}\left(x_j^\mu, x_i^\mu\right)\right), \end{aligned} \tag{O.6}$$

such that the truncated interaction potential $V_{ij}^{\text{tr}}(r_{ij})$ is given:

$$V_{ij}^{\text{tr}}(r_{ij}) = \begin{cases} V_{ij}(r_{ij}) - V_{ij}(r_c) & r_{ij} < r_c \\ 0 & r_{ij} \geq r_c \end{cases}, \tag{O.7}$$

for some cutoff radius r_c. Defining the truncated potential as is done in eq. (O.7) ensures continuity of the potential energy function. Note how adding a constant $V_{ij}(r_c)$ to the potential does not affect force as we are taking the derivative. If r_c is chosen appropriately for the short range potential, the speed

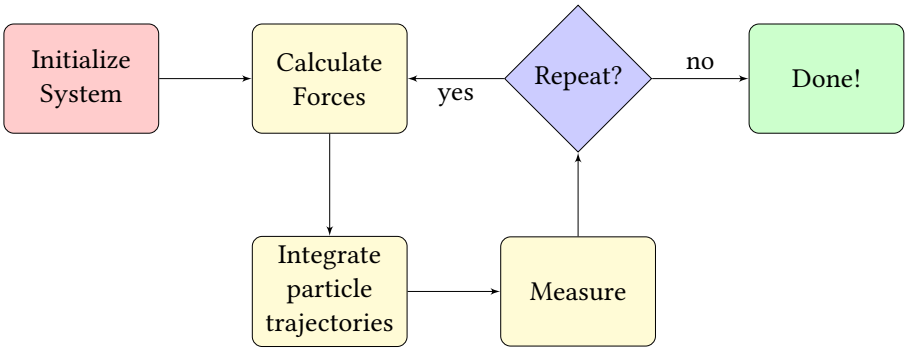

Figure O.1: A simple flowchart depicting how molecular dynamics is roughly done.

up could be significant, whereas the physical error is near insignificant — as interactions at large distances would have less influence than the numerical noise. For more about how to implement this efficiently, see appendix section O.2. For long range interactions with periodic boundaries Ewald summations are required.

Given the trajectory integration method with initial conditions, and the force calculation method, we can start implementing the Molecular dynamics algorithm as depicted in fig. O.1. The Molecular dynamics algorithm evaluates our system from $t_i \to t_{i+1} = t_i + h$ as an approximation to the real Newtonian dynamics. We can repeat this for as long as necessary, taking how many time steps as we want. As we are doing physics, we can measure certain — statistical — properties of interest in-between time steps — or possible more efficiently, just collect all the particles' positions and velocities for post-processing of the data later.

O.1 Boundary conditions

Another important ingredient of molecular dynamics is the boundary conditions. In order to perform the algorithm we have to define a coordinate system in d dimensions. To prevent values from overflowing — and particles from drifting off — boundary conditions are often required. There are occasions where boundary conditions do not matter. For instance, when the particles are attractive at longer ranges and there is no drift in the system, there is no reason to impose a boundary. When the particles are repulsive at longer ranges,

however, imposing a boundary is unavoidable. If no boundary is imposed the particles will scatter and possibly shoot off until a numerical overflow is encountered. Hence it is convenient to impose a simulation box in which the particles can be confined.

We may start by building the box in which the particles reside. The simulation box has a hypervolume:

$$V = \prod_{\delta}^{d} L_\delta \tag{O.8}$$

where d is the dimension of the system and L_δ is the size of the box in each component. The origin is placed right in the middle of the box such that the boundaries of the box are present at every $\pm\frac{1}{2}L_\delta$. A two-dimensional box is depicted in fig. O.2. The boundaries can have boundary conditions per dimension. Canonical boundary conditions are either periodic, where the box is tiled and wrapped, or hard, where the particles perfectly bounce off the boundary. Additionally, we may change the shape of the simulation box itself by applying linear transformations, making it shrink, rotate, expand and shear. Should we, however, want hard boundaries of an arbitrary shape, there is yet another way of imposing them. Consider a particle confined inside the hatched blob in fig. O.2. We may approximately compose such a shape from straight lines and circles; circles and straight lines have very well-defined regular tangents. Once we know the lines and circles — with their tangents — we can apply a spring-like force to a particle in case it tries to transcend the boundary. Choosing a sufficiently stiff spring constant will mimic a perfect hard boundary quite well.

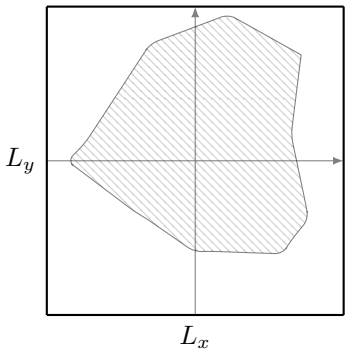

Figure O.2: A two-dimensional box with dimensions $L_x \times L_y$. The origin of the box is where the grey axes cross. The hatched blob represents an arbitrary boundary imposed on the particles within the box.

It is worth mentioning that if periodic boundary conditions are applied, distances ought to be measured through the boundary wrapping to the other side. This will ensure that particles will interact with other particles through the boundary if sufficiently close.

O.2 Neighbor search algorithms

In order to truly speed up the molecular dynamics algorithm we truncated our potential in eq. (O.6). For the implementation of the molecular dynamics algorithm this means we have to find all the neighbors of particle i within a distance r_c.

In order to do so, let us introduce $r_s > r_c$, which is called the skin radius. In order then to generate a list of all particles within a distance r_c of particle i, all we have to do is consider the list of particles within the skin list — particles within a distance r_s of particle i. We may wonder why this is useful at all; we simply translated the problem of generating the neighbor list to generating the skin list. Why is this an improvement? The answer lies in the dynamics of the problem. Generating the neighbor list from the skin list is of order $\mathcal{O}(NK)$, where $K \leq N$ is the average number of particles in a skin list. Naively, however, generating the skin list of order $\mathcal{O}\left(N^2\right)$ — we will improve on this shortly. Of course we have to generate the skin list, but only if a particle has traveled a distance larger than $r_s - r_c$, which is typically much less frequent than every time step, provided r_s is chosen sufficiently large.

The naive way of finding the nearest neighbors of particle i is to test whether all other particles are within a radius r_s. If positive the particles are added to the skin list. This method is sometimes called a brute force neighbor search.

A more sophisticated method is the *cell algorithm*. As the name suggests, the cell algorithm subdivides space into square, cubic or hypercubic cells — depending on the dimensionality — much like a d-dimensional histogram. Once done, the skin list of particle i is generated by considering particles in the same and nearest neighboring cells. In the case of periodic boundary conditions, the cells will wrap around.

Yet another method of generating the skin list is the *k-d tree*. A k-d tree is a binary tree that stores the particles' positions in a ordered fashion. The ordering is done in such a way that every node is a k-dimensional point where one of the dimensions of space is split in half, generating two subtrees. This way, particles close to each other remain in the same subtree whereas particles far away from each other are in the other subtree. On every level of the tree this process is repeated for a different dimension of the k-dimensional space. Due to the computational time complexity properties of a tree, locating, updating, adding and removing particles from the tree can be at most logarithmic order depending on implementation — for N particles time complexity is of order $\mathcal{O}(\log N)$. The initial build of the tree is of order $\mathcal{O}(N \log N)$.

Appendix P `libmd`

In order to perform molecular dynamics simulations optimized for soft matter physics, we have created a computer library called `libmd`. `libmd` is an in-house molecular dynamics computer library written in `C++11`. The library was initially written in 2013 by dr. J. Paulose, (now dr.) T. H. Beuman, MSc and B. C. van Zuiden, MSc (maintainer) under the supervision of (now prof.) dr. Vincenzo Vitelli.

`libmd` implements molecular dynamics as described in appendix O for arbitrary dimensions. It combines the computational techniques like automatic differentiation (appendix section G.3), state of the art neighbor search algorithms (appendix section O.2) and symplectic integration using the described integrators (appendices K and L and section 4.3) to solve for scenarios with and without curvature. The curvature part of the code assumes a Monge patch (appendix E), where the user only has to provide the Monge function. In addition the library can cope with arbitrary potentials or force terms. It is designed to be extremely flexible and hackable, it supports hooks and is fairly well documented.

Appendix Q Finite discrete lattices

In this appendix we describe some finite discrete two-dimensional lattices, for fun and for profit. These discrete lattices have been used in computational implementations of this thesis. Throughout this appendix we will use the modulus operator denoted $\%$ and defined as $a\%b \equiv a - b\left\lfloor \frac{a}{b} \right\rfloor$ where $\lfloor \ldots \rfloor$ is the floor function[♠] and $a, b \in \mathbb{Z}$. The modulus operator is assumed to have the same precedence as multiplication and devision.

Q.1 Square lattice

The square lattice is a somewhat trivial lattice. Its $N \in \mathbb{N}$ sites are composed of $q_x \in \mathbb{N}$ rows and $q_y \in \mathbb{N}$ columns such that $N = q_x q_y$. Given a lattice spacing a, site $i \in \{0, \ldots, N-1\}$ is positioned at:

$$x_i = a\left(i\%q_x\right), \tag{Q.1}$$

$$y_i = a\left\lfloor \frac{i}{q_x} \right\rfloor. \tag{Q.2}$$

[♠] One can define the floor function as $\lfloor x \rfloor = \max_{z \in \mathbb{Z}} (z \leq x)$.

The four neighbors j_n^i of site i are found using the following formulas:

$$j_0^i = (i+1)\,\%q_x + q_x\left\lfloor \tfrac{i}{q_x} \right\rfloor, \tag{Q.3}$$

$$j_1^i = \left(i + q_x\left(\left\lfloor \tfrac{i}{q_x} \right\rfloor + 1\right)\right)\%N, \tag{Q.4}$$

$$j_2^i = (i-1+q_x)\,\%q_x + q_x\left\lfloor \tfrac{i}{q_x} \right\rfloor, \tag{Q.5}$$

$$j_3^i = \left(i + q_x\left(\left\lfloor \tfrac{i}{q_x} \right\rfloor - 1\right) + N\right)\%N. \tag{Q.6}$$

Q.2 Triangular lattice

A somewhat more complicated lattice is the triangular lattice. Its $N \in \mathbb{N}$ sites are composed of $q_x \in \mathbb{N}$ rows and $q_y \in 2\mathbb{N}$ columns such that $N = q_x q_y$. Given a lattice spacing a, site $i \in \{0, \ldots, N-1\}$ is positioned at:

$$x_i = a\,(i\%q_x) + \tfrac{a}{2}\left(\left\lfloor \tfrac{i}{q_x} \right\rfloor \%2\right), \tag{Q.7}$$

$$y_i = \tfrac{\sqrt{3}a}{2}\left\lfloor \tfrac{i}{q_x} \right\rfloor. \tag{Q.8}$$

The six neighbors j_n^i of site i are found using the following formulas:

$$j_0^i = (i+1)\,\%q_x + q_x\left\lfloor \tfrac{i}{q_x} \right\rfloor, \tag{Q.9}$$

$$j_1^i = \left(\left(i + \left\lfloor \tfrac{i}{q_x} \right\rfloor \%2\right)\%q_x + q_x\left(\left\lfloor \frac{i}{q_x} \right\rfloor + 1\right)\right)\%N, \tag{Q.10}$$

$$j_2^i = \left(\left(i - 1 + q_x + \left\lfloor \tfrac{i}{q_x} \right\rfloor \%2\right)\%q_x + q_x\left(\left\lfloor \frac{i}{q_x} \right\rfloor + 1\right)\right)\%N, \tag{Q.11}$$

$$j_3^i = (i-1+q_x)\,\%q_x + q_x\left\lfloor \tfrac{i}{q_x} \right\rfloor, \tag{Q.12}$$

$$j_4^i = \left(\left(i - 1 + q_x + \left\lfloor \tfrac{i}{q_x} \right\rfloor \%2\right)\%q_x + q_x\left(\left\lfloor \tfrac{i}{q_x} \right\rfloor - 1\right) + N\right)\%N, \tag{Q.13}$$

$$j_5^i = \left(\left(i + \left\lfloor \tfrac{i}{q_x} \right\rfloor \%2\right)\%q_x + q_x\left(\left\lfloor \tfrac{i}{q_x} \right\rfloor - 1\right) + N\right)\%N. \tag{Q.14}$$

Q.3 Honeycomb lattice

An even more complicated lattice is the honeycomb lattice. Its $N \in \mathbb{N}$ sites are composed of $q_x \in 2\mathbb{N}$ rows and $q_y \in 2\mathbb{N}+1$ columns such that $N = q_x q_y$. Given a lattice spacing a, site $i \in \{0, \dots, N-1\}$ is positioned at:

$$x_i = \tfrac{\sqrt{3}a}{2} i \% q_x, \tag{Q.15}$$

$$y_i = \tfrac{3a}{2} \left\lfloor \tfrac{i}{q_x} \right\rfloor \% q_y + \tfrac{a}{2} \left| (i \% q_x) \,\%2 - \left(\left\lfloor \tfrac{i}{q_x} \right\rfloor \% q_y \right) \%2 \right| \tag{Q.16}$$

The three neighbors j_n^i of site i are found using the following formulas:

$$j_0^i = (i \% q_x + 1) + q_x \left\lfloor \tfrac{i}{q_x} \right\rfloor, \tag{Q.17}$$

$$j_1^i = (i \% q_x - 1 + qx) + q_x \left\lfloor \tfrac{i}{q_x} \right\rfloor, \tag{Q.18}$$

$$j_2^i = \left(i + q_x \left(2 \left| (i \% q_x) \,\%2 - \left(\left\lfloor \tfrac{i}{q_x} \right\rfloor \% q_y \right) \%2 \right| - 1 \right) + N \right) \% N. \tag{Q.19}$$

Q.4 Lieb lattice

A possibly more complicated lattice is the Lieb lattice. Its $N \in \mathbb{N}$ sites are composed of $q_x \in \mathbb{N}$ rows and $q_y \in 2\mathbb{N}$ columns such that $N = q_x q_y$. Given a lattice spacing a, site $i \in \{0, \dots, N-1\}$ let us first define:

$$n = \tfrac{3q_x}{2} + q_x \%2, \tag{Q.20}$$

$$f_i = i \% n, \tag{Q.21}$$

site i is then positioned at:

$$x_i = \begin{cases} a f_i & f_i < q_x \\ 2a \left(f_i - q_x \right) & f_i \geq q_x \end{cases}, \tag{Q.22}$$

$$y_i = \begin{cases} 2a \left(\left\lfloor \tfrac{i}{n} \right\rfloor \% q_x \right) & f < q_x \\ 2a \left(\left\lfloor \tfrac{i}{n} \right\rfloor \% q_x + \tfrac{1}{2} \right) & f \geq q_x \end{cases}. \tag{Q.23}$$

Sites with three types of sites. First there is $f_i < q_x$ and $f_i \% 2 = 0$ with four neighbors:

$$j_0^i = \left(f_i + 1 \right) \% q_x + n \left\lfloor \tfrac{i}{n} \right\rfloor, \tag{Q.24}$$

$$j_1^i = \left(\left\lfloor \tfrac{f_i}{2} \right\rfloor + q_x + n \left\lfloor \tfrac{i}{n} \right\rfloor \right) \% N, \tag{Q.25}$$

$$j_2^i = \left(f_i - 1 + q_x \right) \% q_x + n \left\lfloor \tfrac{i}{n} \right\rfloor, \tag{Q.26}$$

$$j_3^i = \left(\left\lfloor \tfrac{f_i}{2} \right\rfloor + q_x + n \left(\left\lfloor \tfrac{i}{n} \right\rfloor + 1 \right) + N \right) \% N. \tag{Q.27}$$

Second, there is $f_i < q_x$ and $f_i \% 2 = 1$ with two neighbors:

$$j_0^i = (f_i + 1) \,\%q_x + n\left\lfloor \tfrac{i}{n} \right\rfloor, \tag{Q.28}$$

$$j_1^i = (f_i - 1 + q_x) \,\%q_x + n\left\lfloor \tfrac{i}{n} \right\rfloor. \tag{Q.29}$$

Finally, there is $f_i \geq q_x$ also with two neighbors:

$$j_0^i = \left(2\,(f - q_x) + n\left(\left\lfloor \tfrac{i}{n} \right\rfloor + 1\right)\right) \%N, \tag{Q.30}$$

$$j_1^i = \left(2\,(f - q_x) + n\left(\left\lfloor \tfrac{i}{n} \right\rfloor\right)\right) \%N. \tag{Q.31}$$

References

[1] J. L. Aragones, J. P. Steimel, and A. Alexander-Katz. *Elasticity-induced force reversal between active spinning particles in dense passive media.* **Nat. Comm.** *7.* ***2016*** (*54*).

[2] J. Denk, L. Huber, E. Reithmann, and E. Frey. *Active Curved Polymers Form Vortex Patterns on Membranes.* **Phys. Rev. L** *116* 17. ***2016*** (*53*).

[3] S. J. Ebbens. *Active colloids: Progress and challenges towards realising autonomous applications.* **Curr. Opin. Coll. I. Sci** *21.* ***2016*** (*75*).

[4] C. He, X. Ni, H. Ge, Y.-B. Sun X.-C. Chen, M.-H. Lu, X.-P. Liu, and Y.-F. Chen. *Acoustic topological insulator and robust one-way sound transport.* **Nat. Phys.** ***2016*** (*34*).

[5] V. Koning and V. Vitelli. *Crystals and liquid crystals confined to curved geometries.* Fluids, Colloids, and Soft Materials: An Introduction to Soft Matter Physics *7.* ***2016*** (*5, 77*).

[6] A. Snezhko. *Complex collective dynamics of active torque-driven colloids at interfaces.* **Curr. Opin. Coll. I. Sci** *21.* ***2016*** (*53*).

[7] H. Wioland, F. G. Woodhouse, J. Dunkel, and R. E. Goldstein. *Ferromagnetic and antiferromagnetic order in bacterial vortex lattices.* **Nat. Phys.** ***2016*** (*34, 35*).

[8] J. Yan, M. Han, J. Zhang, C. Xu, E. Luijten, and S. Granick. *Reconfiguring active particles by electrostatic imbalance.* **Nat. Mater.** ***2016*** (*34*).

[9] A. Bricard, J.-B. Caussin, D. Das, C. Savoie, V. Chikkadi, K. Shitara, O. Chepizhko, F. Peruani, D. Saintillan, and D. Bartolo. *Emergent vortices in populations of colloidal rollers.* **Nat. Comm.** *6.* ***2015*** (*34*).

[10] D. R. Brumley, M. Polin, T. J. Pedley, and R. E. Goldstein. *Metachronal waves in the flagellar beating of Volvox and their hydrodynamic origin.* **Jour. of The Roy. Soc. I** *12* 108. ***2015*** (*54*).

[11] F. Ginot, I. Theurkauff, D. Levis, C. Ybert, L. Bocquet, L. Berthier, and C. Cottin-Bizonne. *Nonequilibrium Equation of State in Suspensions of Active Colloids.* **Phys. Rev. X** *5.* ***2015*** (*33, 53*).

[12] Y. Goto and H. Tanaka. *Purely hydrodynamic ordering of rotating disks at a finite Reynolds number.* **Nat. Comm.** *6.* ***2015*** (*54*).

[13] T. Kariyado and Y. Hatsugai. *Manipulation of Dirac Cones in Mechanical Graphene.* **Sci. Rep.** *5.* ***2015*** (*34*).

[14] A. B. Khanikaev, R. Fleury, S. H. Mousavi, and A. Alu. *Topologically robust sound propagation in an angular-momentum-biased graphene-like resonator lattice.* **Nat. Comm.** *6.* ***2015*** (*34, 36, 40*).

[15] C. Maggi, F. Saglimbeni, M. Dipalo, F. De Angelis, and R. D. Leonardo. *Micromotors With Asymmetric Shape That Efficiently Convert Light Into Work By Thermocapillary Effect.* **Nat. Comm.** *6.* ***2015*** (*75*).

[16] L. M. Nash, D. Kleckner, A. Read, V. Vitelli, A. M. Turner, and W. T. M. Irvine. *Topological mechanics of gyroscopic metamaterials.* **Proc. Nat. Acad. Sci.** *112* 47. ***2015*** (*5, 34*).

[17] P. Oswald and G. Poy. *Lehmann rotation of cholesteric droplets: Role of the sample thickness and of the concentration of chiral molecules.* **Phys. Rev. E** *91* 3. ***2015*** (*53*).

[18] J. Paulose, B. G. Chen, and V. Vitelli. *Topological modes bound to dislocations in mechanical metamaterials.* **Nat. Phys.** ***2015*** (*1, 34*).

[19] J. Paulose, A. S. Meeussen, and V. Vitelli. *Selective buckling via states of self-stress in topological metamaterials.* **Proc. Nat. Acad. Sci.** *112* 25. ***2015*** (*1, 34*).

[20] D. J. G. Pearce and M. S. Turner. *Emergent behavioural phenotypes of swarming models revealed by mimicking a frustrated anti-ferromagnet.* **Roy. Soc. I** *12* 111. ***2015*** (*35*).

[21] A. P. Petroff, X.-L. Wu, and A. Libchaber. *Fast-Moving Bacteria Self-Organize into Active Two-Dimensional Crystals of Rotating Cells.* **Phys. Rev. L** *114.* ***2015*** (*53*).

[22] S. Sabrina, M. Spellings, S. C. Glotzer, and K. J. M. Bishop. *Coarsening dynamics of binary liquids with active rotation.* ***2015*** (*54*).

[23] F. Saglimbeni, M. Dipalo, F. De Angelis, R. Di Leonardo, and C. Maggi. *Micromotors with asymmetric shape that efficiently convert light into work by thermocapillary effects.* **Nat. Comm.** *6.* ***2015*** (*53*).

[24] M. Spellings, M. Engel, D. Klotsa, S. Sabrina, A. M. Drews, N. H. P. Nguyen, K. J. M. Bishop, and S. C. Glotzer. *Shape control and compartmentalization in active colloidal cells.* **Proc. Natl. Acad. Sci. USA** *112* 34. ***2015*** (*54*).

[25] R. Susstrunk and S. D. Huber. *Observation of phononic helical edge states in a mechanical topological insulator.* **Sci.** *349* 6243. ***2015*** (*34*).

[26] R. Suzuki, C. A. Weber, E. Frey, and A. R. Bausch. *Polar pattern formation in driven filament systems requires non-binary particle collisions.* **Nat. Phys.** ***2015*** (*35*).

[27] J. Tailleur and M. E. Cates. *Motility-Induced Phase Separation.* **Ann. Rev. Cond. Matt. Phys.** *6.* ***2015*** (*33, 53*).

[28] P. Wang, L. Lu, and K. Bertoldi. *Topological Phononic Crystals with One-Way Elastic Edge Waves.* **Phys. Rev. L** *115* 10. ***2015*** (*34*).

[29] I. Williams, E. C. Oğuz, T. Speck, P. Bartlett, H. Löwen, and C. P. Royall. *Transmission of torque at the nanoscale.* **Nat. Phys.** *12* 1. ***2015*** (*75*).

[30] J. Yan, S. C. Bae, and S. Granick. *Rotating crystals of magnetic Janus colloids.* **Soft Matt.** *11* 1. ***2015*** (*55*).

[31] Z. Yang, F. Gao, X. Shi, X. Lin, Z. Gao, Y. Chong, and B. Zhang. *Topological Acoustics.* **Phys. Rev. L** *114* 11. ***2015*** (*5, 34, 36, 39, 40, 51*).

[32] K. Yeo, E. Lushi, and P. M. Vlahovska. *Collective Dynamics in a Binary Mixture of Hydrodynamically Coupled Microrotors.* **Phys. Rev. L** *114*. ***2015*** (*54*).

[33] A. Cavagna and I. Giardina. *Bird Flocks as Condensed Matter.* **Ann. Rev. Cond. Matt. Phys.** *5* 1. ***2014*** (*33, 53*).

[34] B. G. Chen, N. Upadhyaya, and V. Vitelli. *Nonlinear conduction via solitons in a topological mechanical insulator.* **Proc. Nat. Acad. Sci.** *111* 36. ***2014*** (*1, 34*).

[35] E. Efrati and W. T. M. Irvine. *Orientation-dependent handedness and chiral design.* **Phys. Rev. X** *4* 1. ***2014*** (*75*).

[36] Y. Fily, S. Henkes, and M. C. Marchetti. *Freezing and phase separation of self-propelled disks.* **Soft Matt.** *10* 13. ***2014*** (*66*).

[37] B. Florijn, C. Coulais, and M. van Hecke. *Programmable mechanical metamaterials.* **Phys. Rev. L** *113* 17. ***2014*** (*1*).

[38] V. Koning. *On the geometry of fracture and frustration.* Casimir PhD Series, Delft-Leiden; 2014-25. ***2014*** (*5*).

[39] N. Kumar, H. Soni, S. Ramaswamy, and A. K. Sood. *Flocking at a distance in active granular matter. 5 SP -.* ***2014*** (*34, 48*).

[40] E. Lushi, H. Wioland, and R. E. Goldstein. *Fluid flows created by swimming bacteria drive self-organization in confined suspensions.* **Proc. Nat. Acad. Sci.** *111* 27. ***2014*** (*67*).

[41] N. H. P. Nguyen, D. Klotsa, M. Engel, and S. C. Glotzer. *Emergent Collective Phenomena in a Mixture of Hard Shapes through Active Rotation.* **Phys. Rev. L** *112* 7. ***2014*** (*54*).

[42] Ariel Amir, Jayson Paulose, and David R. Nelson. *Theory of interacting dislocations on cylinders.* **Phys. Rev. E** *87.* ***2013*** (*87*).

[43] A. Bricard, J.-B. Caussin, N. Desreumaux, O. Dauchot, and D. Bartolo. *Emergence of macroscopic directed motion in populations of motile colloids.* **Nat.** *503* 7474. ***2013*** (*33–35, 44, 48, 53, 75*).

[44] T. Brotto, J.-B. Caussin, E. Lauga, and D. Bartolo. *Hydrodynamics of confined active fluids.* **Phys. Rev. L** *110* 3. ***2013*** (*48*).

[45] M. Cavallaro Jr, M. A. Gharbi, D. A. Beller, S. Copar, Z. Shi, R. D. Kamien, S. Yang, T. Baumgart, and K. J. Stebe. *Ring around the colloid.* **Soft Matter** *9*. ***2013*** (*13*).

[46] T. Fukui, Y. Hatsugai, and H. Suzuki. *Chern Numbers in Discretized Brillouin Zone: Efficient Method of Computing (Spin) Hall Conductances.* **Phys. Soc. of Japan**. ***2013*** (*41*).

[47] S. Fürthauer, M. Strempel, S. W. Grill, and F. Jülicher. *Active Chiral Processes in Thin Films.* **Phys. Rev. L** *110* 4. ***2013*** (*53*).

[48] A. Kaiser and Löwen, H. *Vortex arrays as emergent collective phenomena for circle swimmers.* **Phys. Rev. E** *87* 3. ***2013*** (*54*).

[49] C. L. Kane and T. C. Lubensky. *Topological boundary modes in isostatic lattices.* **Nat. Phys.** *10* 1. ***2013*** (*34*).

[50] V. Koning, T. Lopez-Leon, A. Fernandez-Nieves, and V. Vitelli. *Bivalent defect configurations in inhomogeneous nematic shells.* **Soft Matter** *9*. ***2013*** (*13*).

[51] Q. Liu, B. Senyuk, M. Tasinkevych, and I. I. Smalyukh. *Nematic liquid crystal boojums with handles on colloidal handlebodies.* **Proc. Nat. Acad. Sci.** *110* 23. ***2013*** (*13*).

[52] M. C. Marchetti, J. F. Joanny, S. Ramaswamy, T. B. Liverpool, J. Prost, M. Rao, and R. A. Simha. *Hydrodynamics of soft active matter.* **Rev. Mod. Phys.** *85* 3. ***2013*** (*4, 33–36, 48, 53*).

[53] D. Marenduzzo, C. Micheletti, E. Orlandini, and D. Sumners. *Topological friction strongly affects viral DNA ejection.* **Proc. Nat. Acad. Sci.** *110* 50. ***2013*** (*14*).

[54] P. Nitoń, A. Żywociński, M. Fiałkowski, and R. Hołyst. *A "nano-windmill" driven by a flux of water vapour: a comparison to the rotating ATPase.* **Nanoscale** *5* 20. ***2013*** (*75*).

[55] E. Pairam, J. Vallamkondu, V. Koning, B. C. van Zuiden, P. W. Ellis, M. A. Bates, V. Vitelli, and A. Fernandez-Nieves. *Stable nematic droplets with handles.* **Proc. Nat. Acad. Sci.** *110* 23. ***2013*** (*13, 24, 25, 27, 28, 31*).

[56] J. Palacci, S. Sacanna, A. P. Steinberg, D. J. Pine, and P. M. Chaikin. *Living crystals of light-activated colloidal surfers.* **Sci.** *339* 6122. ***2013*** (*33, 53*).

[57] M. C. Rechtsman, J. M. Zeuner, Y. Plotnik, Y. Lumer, D. Podolsky, F. Dreisow, S. Nolte, M. Segev, and A. Szameit. *Photonic Floquet topological insulators.* **Nat.** *496* 7444. ***2013*** (*34*).

[58] S. Sacanna, D. J. Pine, and G.-R. Yi. *Engineering shape: the novel geometries of colloidal self-assembly.* **Soft Matt.** *9.* ***2013*** (*75*).

[59] T. Sanchez, D. T. N. Chen, S. J. DeCamp, M. Heymann, and Z. Dogic. *Spontaneous motion in hierarchically assembled active matter.* **Nat.** *491* 7424. ***2013*** (*33, 53*).

[60] B. Senyuk, Q. Liu, S. He, R. D. Kamien, R. B. Kusner, T. C. Lubensky, and I. I. Smalyukh. *Topological colloids.* **Nat.** *493* 7431. ***2013*** (*13*).

[61] A. P. Solon and J. Tailleur. *Revisiting the Flocking Transition Using Active Spins.* **Phys. Rev. L** *111* 7. ***2013*** (*35*).

[62] H. Wioland, F. G. Woodhouse, J. Dunkel, J. O. Kessler, and R. E. Goldstein. *Confinement Stabilizes a Bacterial Suspension into a Spiral Vortex.* **Phys. Rev. L** *110* 26. ***2013*** (*67*).

[63] Z. Yao and M. O. de la Cruz. *Packing of charged chains on toroidal geometries.* **Phys. Rev. E** *87.* ***2013*** (*13*).

[64] B. Button, L.-H. Cai, C. Ehre, M. Kesimer, D. B. Hill, J. K. Sheehan, R. C. Boucher, and M. Rubinstein. *A periciliary brush promotes the lung health by separating the mucus layer from airway epithelia.* **Sci.** *337* 6097. ***2012*** (*54*).

[65] F. Farrell, M. Marchetti, D. Marenduzzo, and J. Tailleur. *Pattern Formation in Self-Propelled Particles with Density-Dependent Motility.* **Phys. Rev. L** *108* 24. ***2012*** (*35, 48*).

[66] S. Fürthauer, M. Strempel, S. W. Grill, and F. Jülicher. *Active chiral fluids.* **Eur. Phys. JE** *35* 9. ***2012*** (*68*).

[67] Y. Sumino, K. H. Nagai, Y. Shitaka, D. Tanaka, K. Yoshikawa, H. Chaté, and K. Oiwa. *Large-scale vortex lattice emerging from collectively moving microtubules.* **Nat.** *483* 7390. ***2012*** (*53*).

[68] D. Svenšek and R. Podgornik. *Confined chiral polymer nematics: Ordering and spontaneous condensation.* **Europhys. Lett.** *100.* ***2012*** (*14*).

[69] T. Vicsek and A. Zafeiris. *Collective motion.* **Phys. Rep.** *517* 3-4. ***2012*** (*33, 34, 53*).

[70] N. Coq, A. Bricard, F.-D. Delapierre, L. Malaquin, O. du Roure, M. Fermigier, and D. Bartolo. *Collective Beating of Artificial Microcilia.* **Phys. Rev. L** *107.* ***2011*** (*55*).

[71] V. S. R. Jampani, M. Škarabot, M. Ravnik, S. Čopar, S. Žumer, and I. Mu ševi č. *Colloidal entanglement in highly twisted chiral nematic colloids: Twisted loops, Hopf links, and trefoil knots.* **Phys. Rev. E** *84.* ***2011*** (*13*).

[72] T. Lopez-Leon and A. Fernandez-Nieves. *Drops and shells of liquid crystal.* **Coll. and Poly. Sci.** *289.* ***2011*** (*13*).

[73] T. Lopez-Leon, V. Koning, K. B. S. Devaiah, V. Vitelli, and A. Fernandez-Nieves. *Frustrated nematic order in spherical geometries.* **Nat. Phys.** *7.* ***2011*** (*13*).

[74] R. L. Blumberg Selinger, A. Konya, A. Travesset, and J. V. Selinger. *Monte Carlo Studies of the XY Model on Two-Dimensional Curved Surfaces.* **Phys. Chem. B** *115* 48. ***2011*** (*13*).

[75] H. Shin and G. M. Grason. *Filling the void in confined polymer nematics: Phase transitions in a minimal model of dsDNA packing.* **Europhy. Lett.** *96* 3. ***2011*** (*14*).

[76] S. Thutupalli, R. Seemann, and S. Herminghaus. *Swarming behavior of simple model squirmers.* **New J. Phys.** *13.* ***2011*** (*33, 53*).

[77] U. Tkalec, M. Ravnik, S. Čopar, S. Žumer, and I. Muševič. *Reconfigurable Knots and Links in Chiral Nematic Colloids.* **Sci.** *333* 6038. ***2011*** (*13*).

[78] L. Tortora and O. D. Lavrentovich. *Chiral symmetry breaking by spatial confinement in tactoidal droplets of lyotropic chromonic liquid crystals.* **Proc. Nat. Acad. Sci.** *108* 13. ***2011*** (*30*).

[79] J. Deseigne, O. Dauchot, and H. Chaté. *Collective Motion of Vibrated Polar Disks.* **Phys. Rev. L** *105.* ***2010*** (*33, 34, 53*).

[80] U. Gasser, C. Eisenmann, G. Maret, and P. Keim. *Melting of crystals in two dimensions.* **Chem. Phys. Chem.** *11* 5. ***2010*** (*83*).

[81] B. Guirao, A. Meunier, S. Mortaud, A. Aguilar, J.-M. Corsi, L. Strehl, Y. Hirota, A. Desoeuvre, C. Boutin, Y.-G. Han, Z. Mirzadeh, H. Cremer, M. Montcouquiol, K. Sawamoto, and N. Spassky. *Coupling between hydrodynamic forces and planar cell polarity orients mammalian motile cilia.* **Nat. Cell Bio.** *12* 4. ***2010*** (*54*).

[82] M. Z. Hasan and C. L. Kane. *Colloquium: Topological insulators.* **Rev. Mod. Phys.** *82* 4. ***2010*** (*5, 33, 34, 39, 41*).

[83] Y. Hatwalne and M. Muthukumar. *Chiral Symmetry Breaking in Crystals of Achiral Polymers.* **Phys. Rev. L** *105.* ***2010*** (*14*).

[84] A. Kudrolli. *Concentration Dependent Diffusion of Self-Propelled Rods.* **Phys. Rev. L** *104.* ***2010*** (*33, 53*).

[85] V. Schaller, C. Weber, C. Semmrich, E. Frey, and A. R. Bausch. *Polar patterns of driven filaments.* **Nat.** *467* 7311. ***2010*** (*33, 34, 44, 53*).

[86] I. I. Smalyukh, Y. Lansac, N. A. Clark, and R. P. Trivedi. *Three-dimensional structure and multistable optical switching of triple-twisted particle-like excitations in anisotropic fluids.* **Nat. Mater.** *9* 2. ***2010*** (*13*).

[87] N. Uchida and R. Golestanian. *Synchronization and Collective Dynamics in a Carpet of Microfluidic Rotors.* **Phys. Rev. L** *104.* ***2010*** (*53*).

[88] N. Uchida and R. Golestanian. *Synchronization in a carpet of hydrodynamically coupled rotors with random intrinsic frequency.* **Europhys. Lett.** *89* 5. ***2010*** (*53*).

[89] P. Yeh and C. Gu. *Optics of Liquid Crystal Displays.* Wiley Series in Pure and Applied Optics. ***2010*** (*29, 31*).

[90] M. Bowick and L. Giomi. *Two-dimensional matter: order, curvature and defects.* **Adv. in Phys.** *58.* ***2009*** (*13, 77*).

[91] K. Drescher, K. C. Leptos, I. Tuval, T. Ishikawa, T. J. Pedley, and R. E. Goldstein. *Dancing Volvox : Hydrodynamic Bound States of Swimming Algae.* **Phys. Rev. L** *102* 16. ***2009*** (*53*).

[92] A. Leforestier and F. Livolant. *Structure of toroidal DNA collapsed inside the phage capsid.* **Proc. Nat. Acad. Sci.** *106* 23. ***2009*** (*14*).

[93] D. Marenduzzo, E. Orlandini, A. Stasiak, D. W. Sumners, L. Tubiana, and C. Micheletti. *DNA–DNA interactions in bacteriophage capsids are responsible for the observed DNA knotting.* **Proc. Nat. Acad. Sci.** *106* 52. ***2009*** (*14*).

[94] E. Pairam and A. Fernández-Nieves. *Generation and stability of toroidal droplets in a viscous liquid.* **Phys. Rev. L** *102* 23. ***2009*** (*27*).

[95] E. Prodan and C. Prodan. *Topological Phonon Modes and Their Role in Dynamic Instability of Microtubules.* **Phys. Rev. L** *103.* ***2009*** (*34*).

[96] L. Giomi and M. J. Bowick. *Defective ground states of toroidal crystals.* **Phys. Rev. E** *78.* ***2008*** (*13*).

[97] L. Giomi and M. J. Bowick. *Elastic Theory of Defects in Toroidal Crystals.* **Europhys. J. E** *27.* ***2008*** (*13*).

[98] E. Lemaire, L. Lobry, N. Pannacci, and F. Peters. *Viscosity of an electro-rheological suspension with internal rotations.* **Jour. of Rheo.** ***2008*** (*53*).

[99] A. Hexemer, V. Vitelli, E. J. Kramer, and G. H. Fredrickson. *Monte Carlo study of crystalline order and defects on weakly curved surfaces.* **Phys. Rev. E** *76* 5. ***2007*** (*88*).

[100] M. Ravnik, M. Škarabot, S. Žumer, U. Tkalec, I. Poberaj, D. Babi č, N. Osterman, and I. Mu ševi č. *Entangled Nematic Colloidal Dimers and Wires.* **Phys. Rev. L** *99.* ***2007*** (*13*).

[101] T. Araki and H. Tanaka. *Colloidal Aggregation in a Nematic Liquid Crystal: Topological Arrest of Particles by a Single-Stroke Disclination Line.* **Phys. Rev. L** *97.* ***2006*** (*13*).

[102] E. Bertin, M. Droz, and G. Gregoire. *Boltzmann and hydrodynamic description for self-propelled particles.* **Phys. Rev. E** *74* 2. ***2006*** (*35, 48*).

[103] A. Stern and M. Desbrun. *Discrete geometric mechanics for variational time integrators.* ***2006*** (*77, 79, 125*).

[104] V. Vitelli, J. B. Lucks, and D. R. Nelson. *Crystallography on curved surfaces.* **Proc. Nat. Acad. Sci.** *103* 33. ***2006*** (*77, 85, 86*).

[105] J. A. Acebrón, L. L. Bonilla, C. J. Pérez Vicente, F. Ritort, and R. Spigler. *The Kuramoto model: A simple paradigm for synchronization phenomena.* **Rev. Mod. Phys.** *77*. ***2005*** (*53*).

[106] G. R. Fowles and G. L. Cassiday. *Analytical Mechanics.* International student edition. ***2005*** (*105*).

[107] R. Kirchhoff and Löwen, H. *T-structured fluid and jamming in driven Brownian rotators.* **Europhys. Lett.** *69* 2. ***2005*** (*54*).

[108] I. H. Riedel, K. Kruse, and J. Howard. *A self-organized vortex array of hydrodynamically entrained sperm cells.* **Sci.** *309* 5732. ***2005*** (*53*).

[109] H. Stark and T. C. Lubensky. *Poisson bracket approach to the dynamics of nematic liquid crystals: The role of spin angular momentum.* **Phys. Rev. E** *72* 5. ***2005*** (*68*).

[110] J. Toner, Y. Tu, and S. Ramaswamy. *Hydrodynamics and phases of flocks.* **Ann. of Phys.** *318* 1. ***2005*** (*4, 33–36, 48, 53*).

[111] J.-C. Tsai, F. Ye, J. Rodriguez, J. P. Gollub, and T. C. Lubensky. *A Chiral Granular Gas.* **Phys. Rev. L** *94* 21. ***2005*** (*53, 68, 69, 75*).

[112] M. Bowick, D. R. Nelson, and A. Travesset. *Curvature-induced defect unbinding in toroidal geometries.* **Phys. Rev. E** *69*. ***2004*** (*13*).

[113] S. M. Carroll. *Spacetime and Geometry: An Introduction to General Relativity.* ***2004*** (*77*).

[114] I. M. Kulić, D. Andrienko, and M. Deserno. *Twist-bend instability for toroidal DNA condensates.* **Europhys. Lett.** *67* 3. ***2004*** (*13, 14, 17*).

[115] D. R. Nelson, T. Piran, and S. Weinberg. *Statistical Mechanics of Membranes and Surfaces.* ***2004*** (*5, 77*).

[116] P. Prinsen and P. van der Schoot. *Parity breaking in nematic tactoids.* **Jour. of Phys. Cond. Matt.** *16* 49. ***2004*** (*30*).

[117] D. C. Rapaport. *The Art of Molecular Dynamics Simulation.* ***2004*** (*127*).

[118] C. C. Conwell, I. D. Vilfan, and N. V. Hud. *Controlling the size of nanoscale toroidal DNA condensates with static curvature and ionic strength.* **Proc. Nat. Acad. Sci.** *100*. ***2003*** (*14*).

[119] M. Kleman and O. D. Lavrentovich. *Soft Matter Physics: An Introduction.* ***2003*** (*11, 12, 14, 18, 25, 31*).

[120] P. Lenz, J.-F. Joanny, F. Jülicher, and J. Prost. *Membranes with Rotating Motors.* **Phys. Rev. L** *91.* ***2003*** (*54*).

[121] V. N. Manoharan, M. T. Elsesser, and D. J. Pine. *Dense packing and symmetry in small clusters of microspheres.* **Sci.** *301* 5632. ***2003*** (*75*).

[122] M. R. Stukan, V. A. Ivanov, A. Y. Grosberg, W. Paul, and K. Binder. *Chain length dependence of the state diagram of a single stiff-chain macromolecule: Theory and Monte Carlo simulation.* **Journ. Chem. Phys.** *118.* ***2003*** (*14*).

[123] Y. Tabe and H. Yokoyama. *Coherent collective precession of molecular rotors with chiral propellers.* **Nat. Mater.** *2* 12. ***2003*** (*53*).

[124] A. Travesset. *Universality in the screening cloud of dislocations surrounding a disclination.* **Phys. Rev. B** *68* 11. ***2003*** (*77, 91*).

[125] M. D. Contreras and R. Sanchez. *Application of a factorial design to the study of the flow behavior, spreadability and transparency of a Carbopol ETD 2020 gel. Part II.* **Int. Jour. Pharma.** *234* 1. ***2002*** (*27*).

[126] R. D. Kamien. *The geometry of soft materials: a primer.* **Rev. Mod. Phys.** *74.* ***2002*** (*15*).

[127] S. Nonaka, H. Shiratori, Y. Saijoh, and H. Hamada. *Determination of left-right patterning of the mouse embryo by artificial nodal flow.* **Nat.** *418* 6893. ***2002*** (*54*).

[128] H. Levine, W. J. Rappel, and I. Cohen. *Self-organization in systems of self-propelled particles.* **Phys. Rev. E** *63* 1 Pt 2. ***2001*** (*42*).

[129] J. E. Marsden and M. West. *Discrete mechanics and variational integrators.* **Acta Num. 2001** *10.* ***2001*** (*77, 79, 125*).

[130] H. Stark. *Physics of colloidal dispersions in nematic liquid crystals.* **Phys. Rep.** *351* 6. ***2001*** (*13*).

[131] M. Stevens. *Simple Simulations of DNA Condensation.* **Biophys. Journ.** *80.* ***2001*** (*14*).

[132] P. M. Chaikin and T. C. Lubensky. *Principles of Condensed Matter Physics.* ***2000*** (*5, 11*).

[133] H. Levine, W.-J. Rappel, and I. Cohen. *Self-organization in systems of self-propelled particles.* **Phys. Rev. E** *63* 1. ***2000*** (*4*).

[134] R. K. Soong, G. D. Bachand, H. P. Neves, A. G. Olkhovets, H. G. Craighead, and C. D. Montemagno. *Powering an inorganic nanodevice with a biomolecular motor.* **Sci.** *290* 5496. ***2000*** (*75*).

[135] J. Stelzer and R. Bernhard. *Director configurations of a nematic liquid crystal confined in a toroidal geometry. A finite element study.* **arXiv**. ***2000*** (*13*).

[136] C. Kane, J. E. Marsden, and M. Ortiz. *Symplectic-energy-momentum preserving variational integrators.* **Jour. Math. Phys.** *40* 7. ***1999*** (*77, 79, 125*).

[137] Philippe P. *Novel phases and colloidal assemblies in liquid crystals.* **Cur. Opin. Coll. IS** *4* 1. ***1999*** (*13*).

[138] O. D. Lavrentovich. *Topological defects in dispersed words and worlds around liquid crystals, or liquid crystal drops.* **Liquid Crystals** *24* 1. ***1998*** (*13*).

[139] T. C. Lubensky, D. Pettey, N. Currier, and H. Stark. *Topological defects and interactions in nematic emulsions.* **Phys. Rev. E** *57*. ***1998*** (*13*).

[140] S. Pafka, J. Cserti, and G. Tichy. *Monte Carlo studies of two-dimensional dislocation systems in applied external stress.* **Mod. and Sim. in Mat. Sci. and Eng.** *6* 5. ***1998*** (*101*).

[141] P. Poulin and D. A. Weitz. *Inverted and multiple nematic emulsions.* **Phys. Rev. E** *57*. ***1998*** (*13*).

[142] J. Toner and Y. Tu. *Flocks, herds, and schools: A quantitative theory of flocking.* **Phys. Rev. E** *58* 4. ***1998*** (*4*).

[143] V. A. Bloomfield. *DNA condensation by multivalent cations.* **Biopol.** *44* 3. ***1997*** (*14*).

[144] F. Ercolessi. *A molecular dynamics primer.* **Spring college in computational physics, ICTP, Trieste** *19*. ***1997*** (*127*).

[145] P. Poulin, H. Stark, T. C. Lubensky, and D. A. Weitz. *Novel Colloidal Interactions in Anisotropic Fluids.* **Sci.** *275* 5307. ***1997*** (*13*).

[146] P. S. Drzaic. *Liquid Crystal Dispersions.* Liquid Crystals Series,VoL 1. ***1995*** (*13, 27*).

[147] O. D. Lavrentovich and V. M. Pergamenshchik. *Patterns in thin liquid crystal films and the divergence ("surface like") elasticity.* **Jour. Mod. Phys. B** *09* 18n19. ***1995*** (*25*).

[148] J. Toner and Y. Tu. *Long-Range Order in a Two-Dimensional Dynamical XY-Model: How Birds Fly Together.* **Phys. Rev. L** *75* 23. ***1995*** (*4, 33, 35, 48, 53*).

[149] T. Vicsek, A. Czirók, E. Ben-Jacob, I. Cohen, and O. Shochet. *Novel Type of Phase Transition in a System of Self-Driven Particles.* **Phys. Rev. L** *75* 6. ***1995*** (*4, 42*).

[150] J. C. Crocker and D. G. Grier. *Microscopic measurement of the pair interaction potential of charge-stabilized colloid.* **Phys. Rev. L** *73*. ***1994*** (*101*).

[151] O. D. Lavrentovich and V. M. Pergamenshchik. *Stripe Domain Phase of a Thin Nematic Film and the K_{13} Divergence Term.* **Phys. Rev. L** *73.* ***1994*** (*25*).

[152] R. D. Polak, G. P. Crawford, B. C. Kostival, J. W. Doane, and S. Žumer. *Optical determination of the saddle-splay elastic constant K_{24} in nematic liquid crystals.* **Phys. Rev. E** *49.* ***1994*** (*25*).

[153] A. Sparavigna, O. D. Lavrentovich, and A. Strigazzi. *Periodic stripe domains and hybrid-alignment regime in nematic liquid crystals: Threshold analysis.* **Phys. Rev. E** *49.* ***1994*** (*25*).

[154] P. G. de Gennes and J. Prost. *The Physics of Liquid Crystals.* ***1993*** (*11, 14, 18, 23*).

[155] D. W. Allender, G. P. Crawford, and J. W. Doane. *Determination of the liquid-crystal surface elastic constant K_{24}.* **Phys. Rev. L** *67.* ***1991*** (*25*).

[156] K. W. Wojciechowski, D. Frenkel, and A. C. Bra ńka. *Nonperiodic solid phase in a two-dimensional hard-dimer system.* **Phys. Rev. L** *66.* ***1991*** (*66*).

[157] O. D. Lavrentovich and V. V. Sergan. *Parity-breaking phase transition in tangentially anchored nematic drops.* **Il Nuovo Cimento D** *12* 9. ***1990*** (*27, 32*).

[158] B. Fornberg. *Generation of finite difference formulas on arbitrarily spaced grids.* **Math. of Comput.** *51* 184. ***1988*** (*25, 116*).

[159] K. J. Strandburg. *Two-dimensional melting.* **Rev. Mod. Phys.** *60.* ***1988*** (*83*).

[160] C. A. Murray and D. H. Van Winkle. *Experimental observation of two-stage melting in a classical two-dimensional screened Coulomb system.* **Phys. Rev. L** *58.* ***1987*** (*83*).

[161] R. D. Williams. *Two transitions in tangentially anchored nematic droplets.* **Journal of Physics A** *19* 16. ***1986*** (*27, 30*).

[162] D. H. Lee, J. D. Joannopoulos, J. W. Negele, and D. P. Landau. *Discrete-Symmetry Breaking and Novel Critical Phenomena in an Antiferromagnetic Planar XY Model in Two Dimensions.* **Phys. Rev. L** *52* 6. ***1984*** (*61*).

[163] G. E. Volovik and O. D. Lavrentovich. *Topological dynamics of defects: boojums in nematic drops.* **Sov. Phys. JETP** *58* 6. ***1983*** (*27, 30*).

[164] O. G. Mouritsen and A. J. Berlinsky. *Fluctuation-Induced First-Order Phase Transition in an Anisotropic Planar Model of N2 on Graphite.* **Phys. Rev. L** *48* 3. ***1982*** (*60*).

[165] Y. Saito. *Monte Carlo studies of two-dimensional melting: Dislocation vector systems.* **Phys. Rev. B** *26.* ***1982*** (*101*).

[166] I. M. Lifshitz, A. Yu. Grosberg, and A. R. Khokhlov. *Some problems of the statistical physics of polymer chains with volume interaction.* **Rev. Mod. Phys.** *50.* ***1978*** (*14*).

[167] M. Schick and R. B. Griffiths. *Antiferromagnetic ordering in the three-state Potts model.* **J. Phys. A: Math Gen** *10* 12. ***1977*** (*60*).

[168] I. Newton. *Principia mathematica.* **Harvard University Press**. ***1972*** (*105*).

[169] Robert B. Meyer. *Piezoelectric Effects in Liquid Crystals.* **Phys. Rev. L** *22.* ***1969*** (*23*).

[170] M. Abramowitz and I. A. Stegun. *Handbook of mathematical functions: with formulas, graphs, and mathematical tables. 55.* ***1964*** (*119*).

[171] L. E. Dahler and J. S. Scriven. *Angular momentum of continua.* **Nat.** *192* 4797. ***1961*** (*68*).

[172] L. D. Landau, E. M. Lifshitz, J. B. Sykes, J. S. Bell, and M. E. Rose. *Quantum Mechanics, Non-Relativistic Theory. 11* 12. ***1958*** (*52*).

[173] J. J. Thomson. *On the structure of the atom: an investigation of the stability and periods of oscillation of a number of corpuscles arranged at equal intervals around the circumference of a circle; with application of the results to the theory of atomic structure.* **Lond. Edinb. Dubl. Phil. Mag.** *7* 39. ***1904*** (*91*).

Samenvatting

Chiraliteit is een wiskundige eigenschap die objecten classificeert op hun handigheid. Onze handen, bijvoorbeeld, lijken identiek, maar zijn elkaars spiegelbeeld: we kunnen onze handen niet op elkaar plaatsen zolang de handpalmen in dezelfde richting wijzen. Deze eigenschap maakt onze handen chiraal. Chiraliteit kan makkelijk getest worden: als we het object in zijn volledigheid kunnen transleren en/of roteren naar zijn spiegelbeeld is het object *niet* chiraal. Onze handen zijn ruimtelijk chiraal, maar er bestaan ook systemen die chiraal zijn in de tijd. Neem bijvoorbeeld een analoge klok die niet ruimtelijk chiraal is. De secondewijzer op een canonieke klok draait linkshandig.♠ Veel natuurkundige modellen zijn onveranderlijk onder chiraliteit. Dat wil zeggen dat deze modellen niet discrimineren tussen links- en rechtshandige toestanden. Wanneer dit het geval is, kunnen systemen die niet chiraal zijn in een chirale toestand vervallen omdat dit energetisch gunstiger is.

Materie bestaat uit deeltjes. Veel natuurkunde beschrijft materie bestaande uit *passieve* deeltjes met positieafhankelijke interacties. Dit soort passieve materie convergeert naar een thermische *evenwichtstoestand*. Levende biologische systemen of zelfs robotische systemen zijn niet in evenwicht, ze gebruiken energie om tegen de evenwichtstoestand in te werken. Deze systemen bestaan uit *actieve* deeltjes en convergeren naar een *stabiele* toestand. De twee kenmerken van actieve deeltjes zijn dat ze energie consumeren om zichzelf te kunnen voortbewegen en om complexere interacties te hebben met andere deeltjes. Voorbeelden van simpele actieve systemen zijn stammen *E. coli*-bacteriën, een brij van spermacellen, een mierenkolonie of een zwerm vogels. Al deze systemen hebben één ding gemeen: de individuele deeltjes bewegen zich zelf voort in dezelfde richting als hun buren.

♠Hierbij nemen we aan dat de z-as uit de klok wijst.

De topologie en geometrie van de ruimte heeft grote invloed op hoe de materie die in die ruimte leeft zich gedraagt. Een kristal bijvoorbeeld heeft een periodieke structuur. Deze kristalstructuur kan niet voortbestaan als de ruimte zich kromt; net zoals bijvoorbeeld een legpuzzel, waarvan de stukjes niet goed in elkaar passen als de tafel gekromd is. Ook bij actieve materie heeft de topologie en geometrie van de ruimte invloed. Neem bijvoorbeeld lineair gepolariseerde deeltjes — zoals *E. coli*-bacteriën. Als deze deeltjes gevangen worden in een lange buis zal het collectief zich voortbewegen in de axiale richting. Net zo zal het collectief zich azimuthaal voortbewegen als de deeltjes gevangen zitten in een schijf of annulus.

Stel dat we actieve deeltjes gevangen zetten in een schijf. Het collectief zal zich dan azimuthaal voortbewegen, links- of rechtsom. We plaatsen nu een stroomgenerator in het middelpunt van de schijf. Door de stroming van de deeltjes zal de stroomgenerator gaan draaien en kunnen we gratis stroom opwekken. Het lijkt alsof we de tweede wet van de thermodynamica overtreden. Dit is echter niet het geval. De actieve deeltjes consumeren energie en deze energie kan gebruikt worden om de generator aan te drijven. Velen zullen zeggen, op het eerste gezicht is dit niets nieuws: het is al jaren bekend dat biologische materie op deze manier lokaal de tweede wet overtreedt. Het is op dit punt interessant om te noemen dat ook een — strikt levenloos — systeem van colloïden die aan één zijde gecoat zijn met platina in een oplossing van waterstofperoxide in water onder bestraling van ultraviolet licht de tweede wet kan overtreden.

Het begrip topologie heeft de hedendaagse wiskunde en natuurkunde veranderd. Topologie is een manier om een wiskundige ruimte zo te karakteriseren dat deze karakterisatie invariant is onder continue transformaties. Neem bijvoorbeeld een opgeblazen fietsband. Het aantal grepen of gaten in zo een object is behouden ongeacht de lineaire transformaties, geometrische oneffenheden en verschillende inbeddingen. Sterker nog, het aantal grepen fungeert als een canoniek topologisch getal, een geheel getal dat een ruimtelijk object topologisch karakteriseert. Aangezien onze fietsband maar één greep of gat heeft is dit topologische getal één. Als we dit vergelijken met een bal waar precies nul gaten in zitten, concluderen we dat er geen mogelijke manier is om een fietsband te kneden tot een bal — of vice versa. Het is echter wel mogelijk om een fietsband tot koffiekop te kneden — of andersom — omdat het aantal grepen in beide objecten gelijk is. Het aantal grepen is een van de vele mogelijke topologische getallen. Een iets ingewikkelder topologisch

getal voor ruimtelijke objecten is de zogenaamde Euler karakteristiek. In de impulsruimte kan het zogeheten Chern-getal gebruikt worden om te zien of bandkloven topologisch beschermd zijn; zulke bandkloven kunnen dan niet gesloten worden door het systeem continu te veranderen.

Analytische berekeningen voor passieve systemen in thermisch evenwicht zijn vaak al ingewikkeld. Door activiteit en complexe interacties aan het systeem toe te voegen worden deze berekeningen nog ingewikkelder. In beide gevallen kunnen computationele methoden helpen. Numerieke methoden blijken een zeer geschikte manier om analytische theorieën te bevestigen en nieuwe natuurkunde te voorspellen aan de hand van die theorieën. De computer, in combinatie met analytische methoden en mogelijk ook experimenten, maakt grote stappen mogelijk in de huidige wetenschap.

Dit proefschrift bediscussieert de topologische en geometrische eigenschappen van chirale vloeistoffen. In hoofdstuk 1 laten we zien hoe een toroïdaal systeem van vloeibare kristallen in draadgeordende toestand een spontane chirale transitie ondergaat. Dit is opmerkelijk omdat de vloeibarekristaldeeltjes zelf niet chiraal zijn. De transitie blijkt van dezelfde klasse als die van het beroemde Isingmodel, een model voor ferromagnetisme. In hoofdstuk 2 introduceren we een systeem van lineair gepolariseerde zwemmers. Deze lineair gepolariseerde zwemmers zitten gevangen in een rooster van overlappende annuli in de zogenoemde Liebformatie. Dit systeem brengt zichzelf in een stabiele toestand die topologisch insuleert: een klassieke analogie van het befaamde kwantum-Hall-effect. In hoofdstuk 3 beschrijven we een systeem van actief chiraal roterende geladen staafvormige deeltjes. Afhankelijk van de dichtheid van deze deeltjes vormt dit collectief een driehoekig rooster waar de deeltjes zich tijdruimtelijk ordenen (de kristalfase), een vloeistof vormen, of een glas vormen. In de kristalfase vinden we stabiele toestanden in de zogeheten drie-Potts-antiferromagnetische toestand of de haringbottoestand. In de vloeibare fase observeren we stromingen langs de rand van het systeem. De chiraliteit van de deeltjes bepaalt de richting van de stroom in deze fase. In hoofdstuk 4 leiden we een nieuw computeralgoritme af dat Newtons vergelijkingen kan oplossen op een Riemannse variëteit met behoud van energie. Hoewel dit algoritme vele toepassingen heeft, beperken wij ons hier tot het smelten van kristallen op tweedimensionale oppervlakken.

List of publications

- Anton Souslov, Benjamin C. van Zuiden, Denis Bartolo, and Vincenzo Vitelli. *Topological sound in active-liquid metamaterials.* Nature Publishing Group: **Nature Physics**, ***2017***. DOI: 10.1038/nphys4193. arXiv: 1610.06873. URL: https://www.nature.com/nphys/journal/vaop/ncurrent/full/nphys4193.html (visited on 07/17/2017).
  Highlighted in Metamaterials: Topological order gets active, by A. Alù, Nature Physics, 2017.

- Benjamin C. van Zuiden, Jayson Paulose, William T. M. Irvine, Denis Bartolo, and Vincenzo Vitelli. *Spatiotemporal order and emergent edge currents in active spinner materials.* PNAS: **Proceedings of the National Academy of Sciences** *113* (46), 12919–12924, ***2016***. DOI: 10.1073/pnas.1609572113. arXiv: 1606.03934. URL: http://www.pnas.org/content/113/46/12919.abstract (visited on 11/15/2016).
  Highlighted in Spin City, by A. Klopper, Nature Physics 12, 1090, 2016.

- Vinzenz Koning, Benjamin C. van Zuiden, Randall D. Kamien, and Vincenzo Vitelli. *Saddle-splay screening and chiral symmetry breaking in toroidal nematics.* The Royal Society of Chemistry: **Soft Matter**, ***2014***. DOI: 10.1039/C4SM00076E. arXiv: 1312.5092. URL: http://pubs.rsc.org/en/Content/ArticleLanding/2014/SM/c4sm00076e (visited on 08/17/2016).

- Ekapop Pairam, Jayalakshmi Vallamkondu, Vinzenz Koning, Benjamin C. van Zuiden, Perry W. Ellis, Martin A. Bates, Vincenzo Vitelli, and Alberto Fernandez-Nieves. *Stable nematic droplets with handles.* PNAS: **Proceedings of the National Academy of Sciences** *110* (23), 9295–9300, ***2013***. DOI: 10.1073/pnas.1221380110. arXiv: 1212.1771. URL: http://www.pnas.org/content/110/23/9295 (visited on 08/17/2016).

Curriculum vitæ

I WAS BORN in Jerusalem, Israel in November 1987. I attended high school at J. S. G. Maimonides, Amsterdam, The Netherlands, where I graduated in 2007 with a VWO (nt+ng) degree. September 2008 I received my *propedeuse* degree in physics and astronomy at Leiden University. April 2011 I completed my bachelor studies in physics and astronomy at Leiden University. August 2013 I obtained my master's degree in theoretical physics at Leiden University. September 2013 I continued working with (now prof.) dr. Vincenzo Vitelli as a Doctor of Philosophy (Ph. D.) student at Leiden University.